POLITECNICO DI MILANO
DEPARTMENT OF AEROSPACE SCIENCE AND TECHNOLOGY
DOCTORAL PROGRAMME IN AEROSPACE ENGINEERING

TOWARDS SAFE AND RELIABLE ON-ORBIT AUTONOMOUS OPERATIONS WITH MANIPULATORS

Doctoral Dissertation of:
Francesco Cavenago

Supervisor:
Prof. Mauro Massari

Tutor:
Prof. Marco Lovera

The Chair of the Doctoral Program:
Prof. Pierangelo Masarati

2019/2020 – XXXII

You can't connect the dots looking forward; you can only connect them looking backwards. So you have to trust that the dots will somehow connect in your future.

Steve Jobs

Abstract

Even if space robotics is considered one of the most promising technologies for on-orbit servicing missions, the use of spacecraft equipped with manipulators is still very limited. The reason lies in the complexity involved in this kind of missions, which require advanced algorithms to go through very different and demanding phases. First, the space robot has to rendezvous with a target object, which could be uncooperative and thus require the acquisition of information about the motion and physical properties. Then, an effective coordinated control of the spacecraft-manipulator ensemble is necessary, including trajectory generation and robust control schemes for both systems. A stable interaction between the robot and the target must be guaranteed during physical contact due to grasping and manipulation tasks. Moreover, unexpected collisions may occur since the robot is required to operate very close to other objects, and thus a reaction strategy should be implemented to avoid severe damages and the failure of the mission. These are only some of the challenges involved in an on-orbit autonomous robotic missions with manipulators. In this thesis, the attention is focused on the relative pose estimation problem and the physical contact handling. In particular, an high-order numerical extended Kalman filter and an unscented Kalman filter are developed in the differential algebra framework to address the relative state estimation. The improvement in the robustness provided by including nonlinear terms in the estimation process and the reduction of the computational burden thanks to the differential algebra are demonstrated through a comparison among differential-algebra-based filters and the standard counterparts. As regards the physical contact handling, an

observer initially developed for humanoids is first reviewed and analyzed considering space-related issues. Then, a new observer is proposed based on a centroid-joints formulation of the space robot's dynamics. In both schemes, three momentum-based residuals are defined which can be used to reconstruct the external contact wrench. The angular and joint momentum residuals of the new observer show an interesting decoupling from the linear velocity of the spacecraft, which results in improved performance when realistic measurements are considered. Indeed, the linear velocity is not easy to acquire accurately and at high frequency in orbit. The validation of both observers have been carried out on real hardware, that is an important step towards their use in a real space scenario. Along with the contact detection and force estimation, the residuals are used to identify the location of the collision, namely to isolate the collision. Afterwards, another technique for the detection and isolation is also presented, which is based on monitoring the components of the robot's total momentum. The performance is evaluated numerically and a discussion of the pros and cons is reported. Finally, a reaction control strategy to unexpected collisions is proposed which exploits the information from the observer. Thanks to the controller, the robot, after recognizing the impact, moves away from the obstacle reaching a safe position and configuration. It is demonstrated that the controlled system is input-to-state stable, i.e. the error on the states is bounded even during the contact. The performance is assessed through a simulation example, considering a 7 degrees-of-freedom robotic arm on a 6 degrees-of-freedom moving spacecraft, equipped with thrusters and variable speed control moment gyros.

Sommario

L'utilizzo in orbita di manipolatori robotici è ancora molto limitato, nonostante siano considerati una delle tecnologie più promettenti per numerose operazioni, quali l'ispezione di satelliti, l'assemblaggio di grandi strutture, il rifornimento, la manutenzione, etc. Questo è dovuto alla complessità di questo genere di missioni, che richiedono lo sviluppo di algoritmi avanzati per fronteggiare numerose fasi. Un robot spaziale può essere chiamato ad eseguire un rendezvous con un oggetto target, che potrebbe essere non cooperativo e quindi richiedere la stima del moto e delle proprietà fisiche. Inoltre, un adeguato controllo del sistema accoppiato satellite-manipolatore deve essere sviluppato, insieme ad un efficace algoritmo di generazione di traiettorie per entrambi i sistemi. È necessario garantire una stabile interazione fisica tra il robot e il target nel caso si debba svolgere manipolazione o afferrare il target. Inoltre, data la vicinanza tra i due oggetti in orbita, situazioni di collisioni inaspettate potrebbero insorgere, mettendo a rischio l'intera missione se non trattate in maniera opportuna. Queste sono solo alcune delle sfide tecnologiche che bisogna affrontare nella progettazione di una missione di servicing con robots autonomi. In questa tesi, vengono proposti alcuni algoritmi e strategie per affrontare il problema della stima della posizione ed assetto relativi e la gestione di contatti inaspettati. Un filtro di Kalman esteso di alto ordine e un filtro di Kalman uscented sono stati sviluppati utilizzando l'algebra differenziale per eseguire la stima degli stati relativi. Attraverso un confronto tra i filtri proposti e le rispettive versioni standard, viene mostrato come l'introduzione di termini non lineari nel processo di stima migliori la robustezza e come l'algebra differenzia-

le aiuti a ridurre il peso computazionale. Per quanto riguarda la gestione di contatti inaspettati, un'osservatore sviluppato inizialmente per umanoidi è stato applicato al sistema satellite-manipolatore, considerando le problematiche relative ad uno scenario in orbita. In seguito, si è sviluppata una nuova formulazione dell'osservatore, che si basa su una dinamica centroidale del robot spaziale. In entrambi gli osservatori, il momento totale del sistema viene utilizzato per definire tre residui che possono essere sfruttati per ricostruire forza e coppia agenti sul robot a causa del contatto. Nello schema proposto, i residui calcolati a partire dai momenti angolari e dei giunti risultano essere disaccoppiati dalla misura della velocità del satellite, garantendo delle prestazioni migliori quando misure realistiche vengono considerate. Infatti, la velocità del satellite è una grandezza difficilmente misurabile accuratamente ed ad alta frequenza durante operazioni in orbita. Questi residui possono essere inoltre utilizzati per identificare il punto dove è avvenuto il contatto. Entrambi gli osservatori sono stati validati utilizzando la On-Orbit Servicing Simulator facility del DLR. I tests sperimentali rappresentano un passo importante verso l'utilizzo di queste tecniche in uno scenario spaziale reale. In seguito, un'altra tecnica viene proposta per riconoscere ed isolare il contatto, che si basa sul monitoraggio diretto delle componenti del momento totale del sistema. Le prestazioni vengono valutate attraverso simulazioni numeriche e viene fatto un confronto con gli osservatori analizzando i pro e i contro di ciascuna tecnica. Infine, è presentata una strategia di controllo per reagire al contatto indesiderato. Grazie alle informazioni derivanti dall'osservatore, il controllore comanda al robot il movimento da seguire per allontanarsi dall'ostacolo, raggiungendo una posizione e una configurazione sicure ed evitando possibili situazioni di instabilità. Viene dimostrato analiticamente che il sistema così controllato risulta essere stabile anche durante l'azione del disturbo esterno dovuto al contatto. Le prestazioni del controllore sono valutate attraverso un esempio in simulazione in cui viene modellato un sistema composto da un manipolatore a sette gradi di libertà montato su un satellite. Per controllare il moto di quest'ultimo vengono utilizzati propulsori e giroscopi a velocità variabile per il controllo della coppia.

Contents

List of Figures

List of Tables

CHAPTER 1

Introduction

Space robotics is considered one of the most promising technologies for future successful missions [1]. In particular, satellites equipped with manipulators can be used for on-orbit servicing (OOS) operations, like active debris removal, maintenance of space systems, repair, assembly, inspection, refueling, etc [2]. A number of studies [3] [4] [5] have demonstrated that these robotic operations would result in savings in term of cost effectiveness and in a higher safety. Consequently, on-orbit servicing missions have been a long-term goal since their first conceptual designs in the early 1980s, with the ARAMIS project [6]. However, after almost 40 years, the use of orbital robots is still very limited. The major experiences are the ones related to the space shuttle and the International Space Station (ISS), i.e., the Shuttle Remote Manipulator System (SRMS) [7], the Space Station Remote Manipulator System (SSRMS) [8], the Japanese Experiment Module Remote Manipulator System (JEMRMS) [9] and the European Robotic Arm (ERA) [10]. In addition to these, some test missions have been carried out to develop robotic technologies, such as the Robot Technology Experiment (ROTEX) [11] and the Robotics Component Verification on the ISS (ROKVISS) [12] by the German Aerospace Center (DLR). In the former one, robotic technologies were experimen-

tally demonstrated aboard the Space Shuttle, verifying a variety of teleoperation modes characterized by several seconds of delay. In the latter test mission, some robotic components were tested in orbit. The first OOS demonstration mission can be dated 1997: the Experimental Test Satellite VII (ETS-VII) [13] of the JAXA. A 6-degrees-of-freedom (DoF) manipulator was mounted on an unmanned vehicle and autonomous rendezvous and docking, teleoperation and servicing tasks were verified. Another demonstration mission was the Orbital Express [14] in 2007 by the Defense Advanced Research Project Agency (DARPA), in which different technologies for autonomous servicing, such as docking, refueling, ORU replacement, were tested. Along with this mission, DARPA started a number of other OOS programs, like the Spacecraft for Universal Modification of Orbits (SUMO) [15], later renamed Front-end Robotics Enabling Near-term Demonstration (FREND) [16], and PHOENIX [17]. In these programs, the developed technologies were tested only in laboratory. The Canadian Space Agency (CSA), the Russian Space Agency (RSA) and the DLR worked on an OOS mission called Technology Satellites for Demonstration and Verification of Space Systems (TECSAS) [18], which consisted in a spacecraft equipped with a manipulator and a target satellite to be captured and serviced in orbit. This project was then stopped and only the DLR has continued in the same direction with the subsequent project DEOS (Deutsche Orbitale Servicing Mission) [19].
Despite of the potential of robotic technologies for OOS missions, from the Orbital Express experience, no other space robotic arms for servicing have been launched. The reason lies in the high complexity involved in this kind of missions, especially if the system is wanted to be autonomous. In order to carry out successful and reliable robotic operations in orbit, many challenges have to be faced and a further development of the robotic technologies must be pursued. Indeed, an OOS mission is made up of several interconnected building blocks, which should work efficiently and guarantee safety and robustness. The principal ones are listed below.

- **Relative pose estimation**: the final approaching phase includes to acquire the 6DoF motion of a target satellite, that means to estimate the position, attitude, linear and angular velocity.
- **Target's parameters estimation and structural integrity assessment**: the acquisition of the physical properties, such as the inertia parameters, is essential to stabilize the composite servicer-target system after the capture, in case of a noncooperative, unknown target satellite, and to assess the structural integrity, which is a serious issue

in a real servicing scenario.

- **Proximity rendezvous**: the motion trajectory and the strategy for the final approaching are determined in this phase.
- **End-effector's path planning**: once the target's information are acquired, the end-effector motion is planned to reach the grasp point, in case of a capture task, or a point of interest, if an inspection task is considered, for instance.
- **Space robot control**: the manipulator is deployed and the whole ensemble spacecraft-manipulator has to be controlled to perform the desired tasks, either manipulation or contact-free motion.
- **Physical contact handling**: this is considered one of the main challenges to be solved for a safe and reliable OOS mission. A safe physical interaction between the space robot and the target must be guaranteed if capture is requested. In addition to that, since the robot operates in the proximity of another object or even other objects, erroneous movements or unforeseen situations may lead to unexpected collisions that must be dealt with by the space robot properly, avoiding critical consequences.
- **Stabilization in the post-capture phase**: the composite servicer-target system must be stabilized, considering the new inertia properties and flexible elements.

In this thesis, only some of the listed issues are addressed. Especially, some algorithms and strategies are proposed for the relative pose estimation problem and the physical contact handling during unexpected collisions, which must be properly addressed for the development of an effective autonomous system.

1.1 Relative pose estimation

As previously explained, in the context of an OOS mission, the space robot, called also chaser or servicer, may demand the proximity or rendezvous with a target satellite. The target may be either cooperative, with some type of beacon or target and a docking fixture, if that is required, or uncooperative, i.e., a spacecraft that has no active or passive equipment, targets, or procedures to help in the process. As regards the relative pose estimation, this latter scenario is the most demanding one, since there are no available sensors on the target. A typical example is the case of a chaser

approaching the target during an active debris removal mission [20]. Even before attempting the capture, one of the main challenges of these missions is approaching the target, estimating the relative position with respect to the chaser, and studying and predicting the attitude of the target, which, in the general case, tends to show a tumbling motion. This is crucial for safe proximity operations and demands accurate, real-time measurements and estimations of relative range and attitude [21] [22]. Generally, attitude and range estimation in rendezvous problems with cooperative and uncooperative targets can be classified into model-based and non-model-based techniques. Non-model-based techniques match corresponding features in the two views of a stereo camera for pose estimation, not depending on prior knowledge of the object. Many such algorithms may have difficulty in image-to-model feature correlation and foreground-background segmentation. On the contrary, model-based techniques take advantage of prior knowledge of the object whose pose and motion are to be estimated. In both cases, due to the presence of noise and errors, the estimation method shall include filtering. Thus, the problem of relative position estimation and attitude prediction shall go through the following steps:

1. time update of state and covariance of 6 degrees-of-freedom motion;
2. measurement update and state vector estimation.

In all of the above steps, the state vector must include the translational and rotational motion. More specifically, in the time update of the state and covariance, it is important to consider the nonlinear 6DoF dynamics, including possible couplings between the translational and rotational motion. Therefore, this can be classified as a problem of nonlinear filtering.
At present time, one of the most exploited estimation algorithm is the extended Kalman filter (EKF) [23]. The EKF is based on the main idea of linearizing the equations of motion and the measurement equations via first-order Taylor expansions around the current mean and covariance (the uncertainties are assumed to be Gaussian distributed). In some cases, however, the linear assumption may fail due to the nature of the dynamics or the number of available measurements, leading to inaccurate realization of the local motion. Therefore, alternative methods capable of accounting for system nonlinearity must be used. A different approach is the Unscented Kalman Filter (UKF) [24] [25]. This technique is based on the unscented transformation, which does not contain any linearization. Carefully-chosen sample points are propagated through the true nonlinear system in order to propagate the expected value and covariance. Thanks to its nonlinear nature,

UKF provides superior performance with respect to the EKF in highly nonlinear situations. In 2007, Park and Scheeres [26] [27] developed the high order numerical Kalman filter (HNEKF) by implementing a semi-analytic orbit uncertainty propagation technique, that is by solving for the higher-order Taylor series terms describing the localized nonlinear motion, and by analytically mapping the initial uncertainties. These higher-order filters are more accurate than the EKF, as the prediction step relies on a fully nonlinear mapping of the means and covariances. However, the HNEKF needs to derive the so-called higher-order tensors, which makes it in many cases difficult to use due to computational complexity.
The complexity of integrating multiple points, for UKF, and of deriving the high-order tensor, for the HNEKF, to map the mean and covariance can be easily solved using Differential Algebra (DA) techniques. By substituting the classical implementation of real algebra with the implementation of a new algebra of Taylor polynomials, any function f of n variables can be easily expanded into its Taylor polynomial up to an arbitrarily order m in the DA framework [28] [29]. This has a strong impact when the numerical integration of an ordinary differential equation (ODE) is performed by means of an arbitrary integration scheme. Any integration scheme is based on algebraic operations, involving the evaluation of the ODE right hand side at several integration points. Therefore, starting from the DA representation of the initial conditions and carrying out all the evaluations in the DA framework, the flow of an ODE is obtained at each step as its Taylor expansion in the initial conditions. Consequently, by propagating the mean trajectory and evaluating the measurement function in the DA framework, not only their pointwise values are obtained, but also the higher-order partials. This eliminates the need to calculate the higher-order tensors at each time step by solving a complex system of augmented ODE, for the HNEKF [30] [31] [32]. Moreover, it reduces the multiple integration of the UKF to an easier evaluation of the Taylor expansion of the flow in different sample points.
In this thesis, the HNEKF and UKF are implemented in the DA framework and applied to the problem of the relative pose estimation of a target. Especially, the European Space Agency (ESA) e.Deorbit mission, involving the Envisat satellite, is taken as reference scenario. The performance of the two nonlinear filters is assessed and compared not only in terms of accuracy, but also in terms of computational weight. Indeed, current space processors have limited computational power which restricts the implementable estimation processes. Therefore, a key point for the success of these missions is the development of efficient algorithms capable of limiting the compu-

tational burden without losing out the necessary performance. To this aim, the DA-based HNEKF, which was developed inside the Ariadna study "Assessment of Onboad DA State Estimation for Spacecraft Relative Navigation" [33] in collaboration with ESA, has been also implemented on a BeagleBone Black[1] platform, which is deemed to be representative of the low computational capability in orbit.

1.2 Physical contact handling

On-orbit servicing will require the robot to operate in close proximity to a target object, or another robot, or an astronaut, potentially [1]. In these conditions, contact situations could arise and they may be intentional, e.g. a grasping operation, or accidental, e.g. an unforeseen collision. The space robot should be endowed with algorithms to master all these circumstances properly.
Since the pioneering works, the dynamics of the contact phase has been extensively studied, considering in particular free-floating robots [34] [35] [36] [37]. Moreover, many authors have addressed the problem of guaranteeing a safe interaction when the robot's end-effector comes into contact with the target to perform grasping tasks [38] [39] [40] [41] [42]. Some methods [41] explicitly require an external force feedback to tackle the problem, while others [38] [43] might benefit from its knowledge. For this reason, the space robot can be equipped with a force-torque sensor duly placed at the wrist. However, this sensor can not be redundant, and thus a failure could prevent the achievement of the planned task. Furthermore, there may be situations in which the contact does not occur exactly at the foreseen location, and the sensor may provide inaccurate measurements [44].
These motivations have pushed some researchers to propose a different approach, in which the contact force is estimated without using a dedicated sensor. In [44] the use of the disturbance observer is proposed, while in [38] the force is reconstructed through the target's equations of motion. These methods require quantities that are not measured directly, as the joint accelerations and the linear velocity of robot base for the former, and the target accelerations for the latter. These quantities could be obtained through numerical differentiation, but they would introduce nonnegligible noise in the estimation process. Moreover, in these works the contact is assumed to be at the end-effector, and thus the location is known.
In this thesis, the more general situation of an unexpected collision in an

[1] https://elinux.org/Beagleboard:BeagleBoneBlack.

unknown point along the space robot is considered. Note that the contact at the end-effector is just a subcase in which the location is known. The generic collision handling problem has been already studied for fixed-base manipulators [45] [46], humanoids [47] [48] and flying robots [49] [50], while it is still to be analyzed for orbital robots. The capability of identifying a collision is deemed to be of paramount importance for an autonomous robotic system. For instance, imagine a space robot moving nearby an unknown target to inspect it and perform some tasks. If some appendages are not reconstructed or recognized properly, they can be impacted by the manipulator during the operations. Alternatively, a situation of unplanned contacts may be caused by a wrong identification of the grasping point or an incorrect estimation of position and velocity. Indeed, this could lead to a wrong end-effector path planning and thus to collide with another part of the target. Algorithms to master these situations would increase the level of autonomy and safety since the robot would be able to realize that a dangerous occurrence is happening and react accordingly, preventing a complete failure of the mission.
Along the same line of [45], contact handling can be divided into different phases:

- **Contact detection**: the goal of this phase is to detect whether a contact occurred or not. A signal, whose modulus is expected to lie below a certain threshold, is monitored and, whenever an unexpected change happens, an alarm is risen. In this phase, it is important to reduce false positive and, at the same time, achieve high sensitivity in order to have a fast detection. Therefore, it is essential to understand the influence of noise and uncertainties on the selected monitoring signal. Indeed, the lower the level of noise and uncertainties, the higher the sensitivity.

- **Contact isolation**: this phase aims at locating the exact point of the contact along the robot, or at least the part involved. In case of planned contact, this information can be used to check that the contact occurred at the end-effector. On the other hand, in case of an unexpected collision, the knowledge of the contact position can be exploited either to implement effective reaction strategy or for health monitoring purposes.

- **Contact identification**: the knowledge of the contact force is a valuable information that may be exploited to implement control strategies to guarantee safe physical interaction, in both intentional or unintentional case. In the latter situation, this information can also be used to

quantify the seriousness of the collision. Therefore, in this phase the external disturbance, in terms of force, moment and joint torques, is estimated.

- **Contact reaction**: in this last phase the robot is controlled to react properly to the external disturbance caused by the contact. Depending on the situation, whether the contact is desired or not, different control strategies can be implemented. In the former case, the robot should keep the contact with target, while, in the latter one, it should move away. In both situations, a certain compliant behavior should be ensured by the controller. It is important to stress that in the latter situation the lack of a proper reaction would cause multiple impacts and possible instabilities. Indeed, the robot would try to pursue the original goal pushing against the obstacle.

To address the first three phases jointly, the residual-based observer, proposed in [47] for humanoids, is first reviewed and analyzed considering the features of a space robot, such as the base actuation system and the impossibility to measure some states accurately. This observer computes the linear, angular and joint momentum residuals which turn out to be the estimates of the external generalized forces acting on the floating base and the disturbance joint torques due to the contact. Then, the residuals can be used to estimate the external wrench acting on the robot. The main drawback of the method is the need of a fast and accurate reconstruction of the base linear velocity, which is difficult to obtain in real space applications. Afterwards, a new observer is derived, which is based on a centroid-joints dynamics. The most important feature of this observer is the complete decoupling of the angular and joint momentum residuals from the base linear velocity. These residuals can be used to reconstruct the external wrench leading to a more practical and better-performing solution. Indeed, the proposed method requires only the knowledge of the base angular velocity and control moments, and the joint positions, velocities and torques, which can be acquired at high frequency and feature relatively low noise. Moreover, the angular and joint momentum residuals can be used to isolate the contact rapidly and accurately. Both observers have been validated on the On-Orbit Servicing Simulator (OOS-Sim) hardware-in-the-loop facility [51] at the DLR. The performed tests represent an important step towards the demonstration of the observers' applicability in a real space scenario. Note that the observer in [47] has never been tested on real hardware before.
Also another method is developed for the detection and isolation phases, which is based on monitoring the components of the total momentum of

the space robot. This strategy is very straightforward in case of free-floating robots, since the total momentum is expected to be constant until a collision occurs. In addition, knowing the momentum variations, the second cardinal equation of dynamics can be used to determine the contact point along the manipulator. Then, the method can be extended to actuated-base robots too, as it is shown in Chapter 5.
As regards the reaction phase, a compliant controller is proposed to face unexpected collisions. The controller uses the information from the developed observer to move away from the obstacle reaching a safe position and configuration, while keeping a desired attitude. Thanks to this strategy, multiple impacts and the increase of the force, which can lead to damages and instability, are avoided. The controller is proven to be input-to-state stable, namely the error on the states is bounded during the contact and goes to zero when the contact ends. The performance is assessed through numerical simulations considering thrusters and momentum exchange devices as actuators for the spacecraft.

1.3 Thesis structure

The thesis is structured as follows.

- **Chapter 2**: this chapter contains the background knowledge and concepts used in the development of the proposed techniques and, along with that, the main notations used.
- **Chapter 3**: this chapter and the following one are dedicated to the relative pose estimation problem. Especially, the high order numerical Kalman filter is introduced and the DA-based version is developed and the performance assessed.
- **Chapter 4**: the unscented Kalman filter is explained and derived in the DA framework. The perfomance are analyzed through simulations and a comparison with the DA-based HNEKF is reported.
- **Chapter 5**: contact detection, isolation and identification problems are addressed introducing two contact wrench observers and the momentum monitoring technique. A discussion of the pros and cons of the different strategies is reported.
- **Chapter 6**: the compliant controller proposed to face the reaction phase is presented and the input-to-state stability is demonstrated. Moreover, a modification of the observer based on a centroid-joints

dynamics is introduced to include the contribution of momentum exchange devices.

- **Chapter 7**: the main conclusions of the work are drawn and future developments are discussed. In particular, how to integrate all the techniques developed with the other building blocks necessary for an OOS mission is analyzed.

CHAPTER 2

Background

This chapter is inteded to provide the background knowledge necessary for an easier comprehension of the techniques presented in the thesis.

2.1 Differential algebra

Differential Algebra techniques allow solving analytical problems through an algebraic approach [29]. Similar to the computer representation of real numbers as Floating Point (FP) numbers, DA allows the representation and manipulation of functions on a computer. Each sufficiently often differentiable function f is represented by its Taylor expansion around an expansion point truncated at an arbitrary finite order. Without loss of generality, 0 is

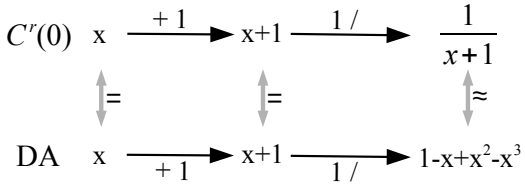

Figure 2.1: *Evaluation of the expression* $1/(1+x)$ *in* $C^r(0)$ *and DA arithmetic.*

chosen as the expansion point. Algebraic operations on the space of truncated Taylor polynomials are defined such that they approximate the operations on the function space $C^r(0)$ of r times differentiable functions at 0. More specifically, each operation is defined to result in the truncated Taylor expansion of the correct result computed on the function space $C^r(0)$. This yields the so-called Truncated Power Series Algebra (TPSA) [28].
To illustrate the process, consider Fig. 2.1. The expression $1/(x+1)$ is evaluated once in $C^r(0)$ and then in the DA framework with truncation order 3. Starting with the identity function x, one is summed to arrive at the function $x + 1$, the representation of which is fully accurate in DA as it is a polynomial of order 1. Continuing the evaluation the multiplicative inversion is performed, resulting in the function $1/(1 + x)$ in $C^r(0)$. As this function is not a polynomial any more, it is automatically approximated in DA arithmetic by its truncated Taylor expansion around 0, given by $1 - x + x^2 - x^3$. Note that, by definition of the DA operations, the diagram for each single operation commutes. That is to say the same result is reached by first Taylor expanding a $C^r(0)$ function (moving from the top to the bottom of the diagram) and then performing the DA operation (moving from left to right), or by first performing the $C^r(0)$ operation and then Taylor expanding the result.
In addition to algebraic operations, the DA framework can be endowed with natural differentiation and integration operators, completing the structure of a differential algebra. Intrinsic functions, such as trigonometric and exponential functions, are built from elementary algebraic operations [29]. This way, Taylor expansions of arbitrary sufficiently smooth functions given by some closed-form expression can be computed fully algebraically in a computer environment. An implementation of such DA computer routines is available in the software DACE 2.0 [52], which is used to implement some of the algorithms presented in this thesis.
An important application of DA in engineering applications is the expansion of the flow $\varphi(t; x_0)$ of an Ordinary Differential Equation (ODE) to arbitrary order with respect to initial conditions, integration times and system parameters. The following is a short summary of the underlying concept. For a more complete introduction to DA, as well as a fully worked out illustrative example of a DA based ODE integrator using a simple Euler step, see [30].
Consider the initial value problem

$$\begin{cases} \dot{x} = f(x, t) \\ x(t_0) = x_0, \end{cases} \tag{2.1}$$

and its associated flow $\varphi(t; x_0)$. By means of classical numerical integration schemes, such as Runge-Kutta or multi-step methods, it is possible to compute the trajectory of a single initial condition x_0 using floating point arithmetic on a computer.
Starting instead from the DA representation of an initial condition x_0, and performing all operations in the numerical integration scheme in DA arithmetic, DA allows propagating the Taylor expansion of the flow around x_0 forward in time, up to the desired final time t_f, yielding a polynomial expansion of $\varphi(t_f; x_0 + \delta x_0)$ up to arbitrary order.
The conversion of standard explicit integration schemes to their DA counterparts is rather straightforward. One simply replaces all operations performed during the execution of the scheme by the corresponding DA operations. Step size control and error estimates are performed only on the constant part of the polynomial, i.e. the reference trajectory of the expansion point. The result is an automatic Taylor expansion of the result of the numerical method (i.e. the numerical approximation to the flow) with respect to any quantity that was initially set to a DA value.
The main advantage of the DA-based approach is that there is no need to derive, implement and integrate variational equations in order to obtain high-order expansions of the flow. As this is achieved by merely replacing algebraic operations on floating-point numbers by DA operations, the method is inherently ODE independent. Furthermore, an efficient implementation of DA such as the DACE 2.0 package, allows to obtain high-order expansions with limited computational time.

2.2 Relative dynamics

The goal of the filters presented in Chapters 3-4 is to estimate the spacecraft relative state for proximity operations of a target. In particular, the ESA e.Deorbit mission [53] is considered as reference and Envisat is selected as uncooperative target satellite.
In the following, the relative translational and rotational dynamics implemented in the filters are reported.

2.2.1 Relative translational dynamics

The relative translational dynamic equations are developed in the local vertical local horizontal (LVLH) frame fixed on the chaser (see Fig. 2.2). In this frame the target relative position $\boldsymbol{r}_r \in \mathbb{R}^3$ and velocity $\boldsymbol{v}_r \in \mathbb{R}^3$ can be defined as:

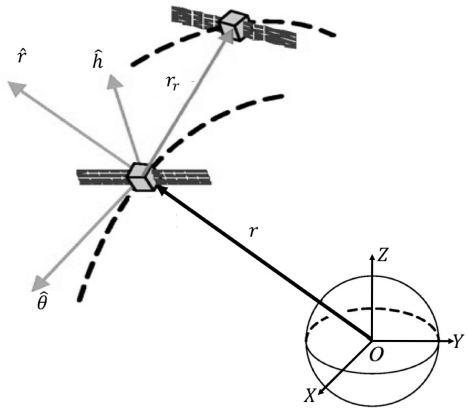

Figure 2.2: *Chaser local vertical local horizontal frame.*

$$\boldsymbol{r}_r = x\hat{\boldsymbol{r}} + y\hat{\boldsymbol{\theta}} + z\hat{\boldsymbol{h}}, \tag{2.2}$$

$$\boldsymbol{v}_r = \dot{x}\hat{\boldsymbol{r}} + \dot{y}\hat{\boldsymbol{\theta}} + \dot{z}\hat{\boldsymbol{h}}, \tag{2.3}$$

where x, y, $z \in \mathbb{R}$ are the three components of $\boldsymbol{r}_r$ in the chaser LVLH frame and $\hat{\boldsymbol{r}}$, $\hat{\boldsymbol{\theta}}$, $\hat{\boldsymbol{h}} \in \mathbb{R}^3$ are the versors of the considered triad. The relative translational dynamics are governed by the following equations [54]:

$$\ddot{x} - 2\dot{\nu}\dot{y} - \ddot{\nu}y - \dot{\nu}^2 x = -\mu(\bar{r} + x)/[(\bar{r} + x)^2 + y^2 + z^2]^{3/2} + \mu/\bar{r}^2, \tag{2.4}$$

$$\ddot{y} + 2\dot{\nu}\dot{x} + \ddot{\nu}x - \dot{\nu}^2 y = -\mu y/[(\bar{r} + x)^2 + y^2 + z^2]^{3/2}, \tag{2.5}$$

$$\ddot{z} = -\mu z/[(\bar{r} + x)^2 + y^2 + z^2]^{3/2}, \tag{2.6}$$

where $\mu \in \mathbb{R}$ is the gravitational parameter, $\bar{r} \in \mathbb{R}$ is the distance from the Earth center to the chaser and $\nu \in \mathbb{R}$ is the true anomaly. Finally, the motion of the chaser is described by the following equations:

$$\ddot{\bar{r}} = \bar{r}\dot{\nu}^2 - \mu/\bar{r}^2, \tag{2.7}$$

$$\ddot{\nu} = -2\dot{\bar{r}}\dot{\nu}/\bar{r}. \tag{2.8}$$

2.2.2 Relative rotational dynamics

As for the rotational dynamics, the relative orientation of the body-fixed reference frame on the target with respect to the body-fixed reference frame on the chaser can be described through a rotation matrix $\boldsymbol{\Gamma} \in \mathbb{R}^{3\times3}$. Consequently, the relative angular velocity and acceleration of the target can be expressed as follows [55]:

$$\boldsymbol{\omega}_r = \boldsymbol{\omega}_t - \boldsymbol{\Gamma}\boldsymbol{\omega}_c, \tag{2.9}$$

$$\dot{\boldsymbol{\omega}}_r = \dot{\boldsymbol{\omega}}_t - \boldsymbol{\Gamma}\dot{\boldsymbol{\omega}}_c + \dot{\boldsymbol{\omega}}_{app}, \tag{2.10}$$

$$\dot{\boldsymbol{\omega}}_{app} = \boldsymbol{\omega}_r \times \boldsymbol{\Gamma}\boldsymbol{\omega}_c, \tag{2.11}$$

where $\boldsymbol{\omega}_c$, $\boldsymbol{\omega}_t \in \mathbb{R}^3$ are the angular velocity of the chaser and the target expressed in their body-fixed reference frame, respectively, $\boldsymbol{\omega}_r \in \mathbb{R}^3$ is the relative angular velocity expressed in the target body-fixed reference frame, and $\dot{\boldsymbol{\omega}}_{app}$ is an apparent angular acceleration.
The relative attitude of the target can be described parameterizing the rotation matrix $\boldsymbol{\Gamma}$. To this aim, the Modified Rodrigues Parameters (MRP) are adopted in this study [56]. The MRP are related to quaternions and to the rotation matrix by the following relations:

$$\boldsymbol{\zeta} = \frac{\boldsymbol{\epsilon}_t}{1+\eta_t}, \tag{2.12}$$

$$\boldsymbol{\Gamma}(\boldsymbol{\zeta}) = \boldsymbol{E} - \alpha_1^A[\boldsymbol{\zeta}]^\times + \alpha_2^A[\boldsymbol{\zeta}]^{\times 2}, \tag{2.13}$$

$$\begin{cases} \alpha_1^A = 4\frac{1-\boldsymbol{\zeta}^T\boldsymbol{\zeta}}{(1+\boldsymbol{\zeta}^T\boldsymbol{\zeta})^2} \\ \alpha_2^A = 8\frac{1}{(1+\boldsymbol{\zeta}^T\boldsymbol{\zeta})^2}, \end{cases} \tag{2.14}$$

where $\boldsymbol{\zeta} \in \mathbb{R}^3$ are the MRP, $\boldsymbol{\epsilon}_t \in \mathbb{R}^3$ and $\eta_t \in \mathbb{R}$ are the vector and scalar part of the quaternions, respectively, and $\boldsymbol{E}$ is the identity matrix. The operator $[\cdot]^\times$ stands for the skew-symmetric matrix of the argument.
The time evolution of the MRP is governed by

$$\dot{\boldsymbol{\zeta}} = \frac{1}{4}\boldsymbol{\Sigma}(\boldsymbol{\zeta})\boldsymbol{\omega}_r, \tag{2.15}$$

$$\boldsymbol{\Sigma}(\boldsymbol{\zeta}) = (1-\boldsymbol{\zeta}^T\boldsymbol{\zeta})\boldsymbol{E} + 2\boldsymbol{\zeta}\boldsymbol{\zeta}^T + 2[\boldsymbol{\zeta}]^\times. \tag{2.16}$$

As for the dynamics, the chaser motion is described by the torque-free Euler equations, while the relative attitude dynamics can be obtained substituting kinematics relationship in the Euler absolute equations of the target spacecraft. The resulting dynamic system is:

$$\boldsymbol{I}_t\dot{\boldsymbol{\omega}}_r + \boldsymbol{\omega}_r \times \boldsymbol{I}_t\boldsymbol{\omega}_r = \boldsymbol{M}_{app} - \boldsymbol{M}_g - \boldsymbol{M}_{ci}, \tag{2.17}$$

$$\boldsymbol{M}_{app} = \boldsymbol{I}_t\boldsymbol{\omega}_r \times \boldsymbol{\Gamma}\boldsymbol{\omega}_c, \tag{2.18}$$

$$\boldsymbol{M}_{ci} = \boldsymbol{I}_t\boldsymbol{\Gamma}\dot{\boldsymbol{\omega}}_c, \tag{2.19}$$

$$\boldsymbol{M}_g = \boldsymbol{M}_{gc} + \boldsymbol{M}_{gcoup}, \tag{2.20}$$

$$\boldsymbol{M}_{gc} = \boldsymbol{\Gamma}\boldsymbol{\omega}_c \times \boldsymbol{I}_t\boldsymbol{\Gamma}\boldsymbol{\omega}_c, \tag{2.21}$$

$$\boldsymbol{M}_{gcoup} = (\boldsymbol{\omega}_r \times \boldsymbol{I}_t\boldsymbol{\Gamma}\boldsymbol{\omega}_c + \boldsymbol{\Gamma}\boldsymbol{\omega}_c \times \boldsymbol{I}_t\boldsymbol{\omega}_r), \tag{2.22}$$

where $\boldsymbol{I}_t \in \mathbb{R}^{3\times3}$ is the matrix of inertia of the target, $\boldsymbol{M}_{app} \in \mathbb{R}^3$ is the apparent torque, $\boldsymbol{M}_{ci} \in \mathbb{R}^3$ is the chaser-inertial torque and $\boldsymbol{M}_g \in \mathbb{R}^3$ is the gyroscopic torque.

2.3 Space robot dynamics

In the dynamics for the filters, the robotic arm is considered folded. Once it is deployed, the space robot, made up of spacecraft and manipulator, is modeled as a multibody system composed of $n + 1$ rigid bodies connected with n revolute joints (see Fig. 2.3). No disturbances caused by the environment (e.g., gravity gradient, air drag and magnetic forces) are taken into account, because they are expected to be considerably smaller than the actuation forces. Note that this is a commonly accepted assumption in space robotics. In the dynamics formulation, a contact on a generic point along the robot is considered. This situation is very general, including both planned contact at the end-effector and unexpected collision.
Four main reference frames are defined. One, denoted by $\mathcal{B}$, is the body frame located on the center-of-mass (CM) of the spacecraft. The second one, denoted by $\mathcal{C}$, is a frame with rotating axes, parallel to $\mathcal{B}$, placed on the CM of the space robot. The third one, denoted by $\mathcal{E}$, is a frame located on the end-effector. The last one is the inertial frame, denoted by $\mathcal{T}$.

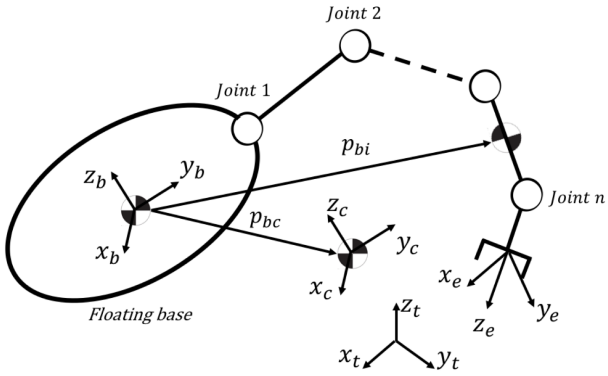

Figure 2.3: *Floating space robot.*

In order to transform forces and velocities between reference frames, the Adjoint transformation [57] is introduced:

$$\boldsymbol{A}_{xy} = \begin{bmatrix} \boldsymbol{R}_{xy} & [\boldsymbol{p}_{xy}]^{\times}\boldsymbol{R}_{xy} \\ \boldsymbol{0} & \boldsymbol{R}_{xy} \end{bmatrix} \in \mathbb{R}^{6\times 6}, \tag{2.23}$$

where $\boldsymbol{p}_{xy} \in \mathbb{R}^3$ and $\boldsymbol{R}_{xy} \in \mathrm{SO}(3)$ indicate the generic position vector, expressed in $\mathcal{X}$, and the rotation matrix from frame $\mathcal{X}$ to frame $\mathcal{Y}$, respectively. Finally, the identity matrix and zero matrix are denoted by $\boldsymbol{E}$ and $\boldsymbol{0}$ of suitable dimensions, respectively.
The dynamics of the space robot can be expressed as follows:

$$\begin{aligned} &\underbrace{\begin{bmatrix} \boldsymbol{M}_t & \boldsymbol{M}_{tr} & \boldsymbol{M}_{tm} \\ \boldsymbol{M}_{tr}^T & \boldsymbol{M}_r & \boldsymbol{M}_{rm} \\ \boldsymbol{M}_{tm}^T & \boldsymbol{M}_{rm}^T & \boldsymbol{M}_m \end{bmatrix}}_{\boldsymbol{M}(\boldsymbol{q})} \begin{bmatrix} \dot{\boldsymbol{v}}_b \\ \dot{\boldsymbol{\omega}}_b \\ \ddot{\boldsymbol{q}} \end{bmatrix} + \\ &+ \underbrace{\begin{bmatrix} \boldsymbol{C}_t & \boldsymbol{C}_{tr} & \boldsymbol{C}_{tm} \\ \boldsymbol{C}_{rt} & \boldsymbol{C}_r & \boldsymbol{C}_{rm} \\ \boldsymbol{C}_{mt} & \boldsymbol{C}_{mr} & \boldsymbol{C}_m \end{bmatrix}}_{\boldsymbol{C}(\boldsymbol{q},\dot{\boldsymbol{q}},\boldsymbol{v}_b,\boldsymbol{\omega}_b)} \begin{bmatrix} \boldsymbol{v}_b \\ \boldsymbol{\omega}_b \\ \dot{\boldsymbol{q}} \end{bmatrix} = \begin{bmatrix} \boldsymbol{f}_b \\ \boldsymbol{m}_b \\ \boldsymbol{\tau} \end{bmatrix} + \begin{bmatrix} \boldsymbol{f}_{ext,b} \\ \boldsymbol{m}_{ext,b} \\ \boldsymbol{\tau}_{ext} \end{bmatrix}, \end{aligned} \tag{2.24}$$

where

$$\begin{bmatrix} \boldsymbol{f}_{ext,b} \\ \boldsymbol{m}_{ext,b} \\ \boldsymbol{\tau}_{ext} \end{bmatrix} = \begin{bmatrix} \boldsymbol{A}_{pb}^T \\ \boldsymbol{J}_p^T \end{bmatrix} \boldsymbol{\mathcal{F}}_{ext}, \tag{2.25}$$

and where $\boldsymbol{\mathcal{F}}_{ext} = [\boldsymbol{f}_{ext}^T \ \boldsymbol{m}_{ext}^T]^T \in \mathbb{R}^6$ is the contact wrench at a generic point p along the robot; $\boldsymbol{J}_p = [\boldsymbol{J}_{vp}^T \boldsymbol{J}_{\omega p}^T]^T \in \mathbb{R}^{6\times n}$ is the fixed-base robot's Jacobian for the generic contact point p, with $\boldsymbol{J}_{vp} \in \mathbb{R}^{3\times n}$, $\boldsymbol{J}_{\omega p} \in \mathbb{R}^{3\times n}$ being the Jacobians mapping $\dot{\boldsymbol{q}}$ into the linear and angular velocity of a frame located on the point p, respectively; $\boldsymbol{v}_b, \boldsymbol{\omega}_b \in \mathbb{R}^3$ are the linear and angular velocity of the base expressed in $\mathcal{B}$; $\boldsymbol{q}, \dot{\boldsymbol{q}} \in \mathbb{R}^n$ are the joint angles and velocities; $\boldsymbol{f}_b, \boldsymbol{m}_b \in \mathbb{R}^3$ are the commanded base force and moment around $\mathcal{B}$, expressed in $\mathcal{B}$; $\boldsymbol{\tau} \in \mathbb{R}^n$ are the commanded joint torques; the submatrices $\boldsymbol{M}_t, \boldsymbol{M}_{tr}, \boldsymbol{M}_r \in \mathbb{R}^{3\times 3}$ compose the inertia matrix of the system regarded as a composite rigid body; the submatrices $\boldsymbol{M}_{tm}, \boldsymbol{M}_{rm} \in \mathbb{R}^{3\times n}$ are the coupling inertia matrices; $\boldsymbol{M}_m \in \mathbb{R}^{n\times n}$ is the inertia matrix of the manipulator; $\boldsymbol{C}(\boldsymbol{q}, \dot{\boldsymbol{q}}, \boldsymbol{v}_b, \boldsymbol{\omega}_b) \in \mathbb{R}^{(6+n)\times(6+n)}$ is the Coriolis/centrifugal matrix. The analytical expressions of the inertia matrix can be found in [43].
The total generalized momentum around $\mathcal{B}$ and expressed in $\mathcal{B}$, denoted by $\boldsymbol{h}_b \in \mathbb{R}^6$, can be written as

$$\boldsymbol{h}_b = \begin{bmatrix} \boldsymbol{h}_b^t \\ \boldsymbol{h}_b^r \end{bmatrix} = \begin{bmatrix} \boldsymbol{M}_t & \boldsymbol{M}_{tr} \\ \boldsymbol{M}_{tr}^T & \boldsymbol{M}_r \end{bmatrix} \begin{bmatrix} \boldsymbol{v}_b \\ \boldsymbol{\omega}_b \end{bmatrix} + \begin{bmatrix} \boldsymbol{M}_{tm} \\ \boldsymbol{M}_{rm} \end{bmatrix} \dot{\boldsymbol{q}}, \tag{2.26}$$

with $\boldsymbol{h}_b^t, \boldsymbol{h}_b^r \in \mathbb{R}^3$ being the translational and rotational momentum, respectively.

2.4 Passivity and input-to-state stability

In this section, the definitions and theorems used in Chapter 6 to prove the input-to-state stability are reported.
Considering the following general dynamic system:

$$\begin{aligned} \dot{\boldsymbol{x}} &= f(\boldsymbol{x}, \boldsymbol{u}) \\ \boldsymbol{y} &= h(\boldsymbol{x}, \boldsymbol{u}) \end{aligned} \tag{2.27}$$

where $\boldsymbol{x} \in \mathbb{R}^n$, $\boldsymbol{u} \in \mathbb{R}^m$, and $\boldsymbol{y} \in \mathbb{R}^g$ are the state vector, input vector and output vector, respectively.
Definition 1 [58] *The system* (2.27) *is passive if there exists a continuously differentiable positive semidefinite function* $V(\boldsymbol{x})$ *such that*

$$\boldsymbol{u}^T\boldsymbol{y} \geq \dot{V} = \frac{dV}{d\boldsymbol{x}} f(\boldsymbol{x},\boldsymbol{u}), \quad \forall(\boldsymbol{x},\boldsymbol{u}) \tag{2.28}$$

Definition 2 [58] *The system* (2.27) *is Input-to-State Stable (ISS) if there exist functions* [1] $\beta \in \mathcal{KL}$ *and* $\gamma \in \mathcal{K}$ such that

$$|\boldsymbol{x}(t,\boldsymbol{x}_0,\boldsymbol{u})| \leq \beta(|\boldsymbol{x}_0|,t) + \gamma\left(\sup(|\boldsymbol{u}|)\right) \tag{2.29}$$

for all $t \geq 0$*, all* $\boldsymbol{x}_0 \in \mathbb{R}^n$*, and all* $\boldsymbol{u}$ *.*

Definition 3 [59] *The system* (2.27) *admits an Input-Output-to-State-Stable Lyapunov function (IOSS-Lyapunov) if there exist a differentiable V:* $\mathbb{R}^n \to \mathbb{R}$ *such that* $\alpha_1(|\boldsymbol{x}|) \leq V(\boldsymbol{x}) \leq \alpha_2(|\boldsymbol{x}|)$ *for some* $\alpha_1, \alpha_2 \in \mathcal{K}_\infty$*, and for all* $\boldsymbol{x}, \boldsymbol{u}$*:*

$$\dot{V} \leq -\gamma(|\boldsymbol{x}|) + \sigma(|\boldsymbol{u}|) + \lambda(|\boldsymbol{y}|) \tag{2.30}$$

where $\sigma, \lambda \in \mathcal{K}$ and $\gamma \in \mathcal{K}_\infty$.

Definition 4 [59] *The system* (2.27) *admits a quasi ISS Lyapunov function (qISS-Lyapunov) if there exist a differentiable V:* $\mathbb{R}^n \to \mathbb{R}$ *such that* $\alpha_1(|\boldsymbol{x}|) \leq V(\boldsymbol{x}) \leq \alpha_2(|\boldsymbol{x}|)$ *for some* $\alpha_1, \alpha_2 \in \mathcal{K}_\infty$*, and for all* $\boldsymbol{x}, \boldsymbol{u}$*:*

$$\dot{V} \leq -\bar{\gamma}(|\boldsymbol{y}|) + \sigma(|\boldsymbol{u}|) \tag{2.31}$$

where $\sigma, \bar{\gamma} \in \mathcal{K}_\infty$.

Theorem 1 [59] *The system* (2.27) *is Input-to-State Stable provided that:*

- *it admits a qISS-Lyapunov function:* $\dot{V}_1 \leq -\bar{\gamma}(|\boldsymbol{y}|) + \sigma_1(|\boldsymbol{u}|)$
- *it admits a IOSS-Lyapunov function:* $\dot{V}_2 \leq -\gamma(|\boldsymbol{x}|) + \sigma_2(|\boldsymbol{u}|) + \lambda(|\boldsymbol{y}|)$
- $\limsup_{r\to\infty} \lambda(r)/\bar{\gamma}(r) < +\infty$

[1] A scalar continuous function $\alpha(r)$, defined for $r \in [0, a)$, belongs to class $\mathcal{K}$ if it is strictly increasing and $\alpha(0) = 0$; it belongs to class $\mathcal{K}_\infty$ is it is defined for all $r \geq 0$ and $\alpha(r) \to \infty$ as $r \to \infty$. A scalar function $\beta(r, s)$, defined for $r \in [0, a)$ and $s \in [0, \infty)$, belongs to class $\beta \in \mathcal{KL}$ if, for each fixed s, the mapping $\beta(r, s)$ belongs to $\mathcal{K}$ with respect to r and, for each fixed r, the mapping $\beta(r, s)$ is decreasing with respect to s and $\beta(r, s) \to 0$ as $s \to \infty$.

CHAPTER 3

Relative pose estimation through DA-based HNEKF

This chapter is devoted to introducing the algorithm of the DA-based numerical extended Kalman filter and to assess its performance considering the relative pose estimation problem, which is crucial in many in-orbit space robotic operations. The analysis of the effects of high-order expansion is also reported taking as study example an Earth-orbiting spacecraft. Finally, having in mind the on-board application, the DA-based HNEKF is implemented on a BeagleBone Black, a platform representative of the limited computational capability of typical processors used on satellites.

3.1 High order extended Kalman filter

Consider the equations of motion and measurement equations describing a generic dynamical system:

$$\begin{aligned} \boldsymbol{x}_{k+1} = &\quad \boldsymbol{\Phi}(t_{k+1}; \boldsymbol{x}_k, t_k) + \boldsymbol{w}_k, \\ \boldsymbol{z}_{k+1} = &\quad \boldsymbol{h}(\boldsymbol{x}_{k+1}, t_{k+1}) + \boldsymbol{v}_{k+1}, \end{aligned} \tag{3.1}$$

where $\boldsymbol{x}_k \in \mathbb{R}^m$ is the vector of state, $\boldsymbol{w}_k \in \mathbb{R}^m$ is the process noise per-

turbing the state, $\boldsymbol{z}_k \in \mathbb{R}^n$ is the vector of actual measurements, $\boldsymbol{h} \in \mathbb{R}^n$ is the measurement function, and $\boldsymbol{v}_{k+1} \in \mathbb{R}^n$ is the measurement noise characterizing the observation error. The process noise and the measurement noise are assumed to be uncorrelated, that is, $E\{\boldsymbol{v}_i\ \boldsymbol{w}_j^T\} = 0$, with the autocorrelations $E\{\boldsymbol{w}_i\ \boldsymbol{w}_j^T\} = \boldsymbol{Q}_i\delta_{ij}$ and $E\{\boldsymbol{v}_i\ \boldsymbol{v}_j^T\} = \boldsymbol{R}_i\delta_{ij}$ for all discrete time indexes i and j. $E\{\}$ denotes the expectation operator and δ_{ij} the Kronecker delta.
For both EKF and HNEKF, the filtering process on the system model equations (3.1) can be summarized as follows:

1. *Prediction step*: at time t_{k+1}, the mean and covariance of the state vector, $\boldsymbol{m}_{k+1}^- \in \mathbb{R}^m$ and $\boldsymbol{P}_{k+1}^- \in \mathbb{R}^{m\times m}$, and the mean of the measurements, $\boldsymbol{n}_{k+1}^- \in \mathbb{R}^n$, are estimated as:

$$\begin{aligned} m_{k+1,i}^- &= E\{\Phi_i(t_{k+1};\boldsymbol{x}_k,t_k) + w_{k,i}\}, \\ P_{k+1,ij}^- &= E\{[\Phi_i(t_{k+1};\boldsymbol{x}_k,t_k) - m_{k+1,i}^- + w_{k,i}][\Phi_j(t_{k+1};\boldsymbol{x}_k,t_k)+ \\ &\quad -m_{k+1,j}^- + w_{k,j}]\}, \\ n_{k+1,p}^- &= E\{h_p(\boldsymbol{x}_{k+1},t_{k+1}) + v_{k+1,p}\}, \end{aligned} \tag{3.2}$$

   where $i,j = 1,...,m$, $p = 1,...,n$, and $m_{k+1,i}^-$, $P_{k+1,ij}^-$ and $n_{k+1,l}^-$ are the components of $\boldsymbol{m}_{k+1}^-$, $\boldsymbol{P}_{k+1}^-$, and $\boldsymbol{n}_{k+1}^-$ respectively;

2. *Update step*: the new measurements acquired at time t_{k+1}, $\boldsymbol{z}_{k+1}$, are incorporated into the updated estimate of the state vector and covariance matrix as follows:

$$\begin{aligned} P_{k+1,pq}^{zz} &= E\{[h_p(\boldsymbol{x}_{k+1},t_{k+1}) - n_{k+1,p}^- + v_{k+1,p}][h_p(\boldsymbol{x}_{k+1},t_{k+1})+ \\ &\quad -n_{k+1,q}^- + v_{k+1,p}]\}, \\ P_{k+1,ip}^{xz} &= E\{[\Phi_i(t_{k+1};\boldsymbol{x}_k,t_k) - m_{k+1,i}^- + w_{k,i}][h_p(\boldsymbol{x}_{k+1},t_{k+1})+ \\ &\quad -n_{k+1,p}^- + v_{k+1,p}]\}, \\ \boldsymbol{K}_{k+1} &= \boldsymbol{P}_{k+1}^{xz}(\boldsymbol{P}_{k+1}^{zz})^{-1}, \\ \boldsymbol{m}_{k+1}^+ &= \boldsymbol{m}_{k+1}^- + \boldsymbol{K}_{k+1}(\boldsymbol{z}_{k+1} - \boldsymbol{n}_{k+1}^-), \\ \boldsymbol{P}_{k+1}^+ &= \boldsymbol{P}_{k+1}^- - \boldsymbol{K}_{k+1}\boldsymbol{P}_{k+1}^{zz}\boldsymbol{K}_{k+1}^T, \end{aligned} \tag{3.3}$$

   where $q = 1,...,n$, $\boldsymbol{K}_{k+1} \in \mathbb{R}^{m\times n}$ is the Kalman gain matrix, $\boldsymbol{P}_{k+1}^{xz} \in \mathbb{R}^{m\times n}$ is the cross-covariance matrix of the state and the measurement, and $\boldsymbol{P}_{k+1}^{zz} \in \mathbb{R}^{n\times n}$ is the covariance matrix of the measurements.

In the classical EKF scheme, at each time t_k, the equations of motion and the measurement equation (3.1) are linearized about the current estimate of the mean and take the form:

$$\begin{aligned} \boldsymbol{x}_{k+1} &= \boldsymbol{m}_{k+1}^{-} + \boldsymbol{A}_k \delta\boldsymbol{x}_k + \boldsymbol{w}_k, \\ \boldsymbol{z}_{k+1} &= \boldsymbol{h}(\boldsymbol{m}_{k+1}^{-}, t_{k+1}) + \boldsymbol{C}_k \delta\boldsymbol{x}_k + \boldsymbol{v}_{k+1}, \end{aligned} \tag{3.4}$$

where $\boldsymbol{A}_k = \frac{\partial \boldsymbol{\Phi}(t_{k+1};\boldsymbol{x}_k,t_k)}{\partial \boldsymbol{x}_k} \in \mathbb{R}^{m\times m}$, $\boldsymbol{C}_k = \frac{\partial \boldsymbol{h}(\boldsymbol{x}_{k+1},t_{k+1})}{\partial \boldsymbol{x}_k} \in \mathbb{R}^{n\times m}$, and $\delta\boldsymbol{x}_k \in \mathbb{R}^m$ is the deviation of the estimated mean from the true trajectory at time t_k, i.e., $\delta\boldsymbol{x}_k = \boldsymbol{x}(t_k) - \boldsymbol{m}_k^{+}$, and $\boldsymbol{m}_{k+1}^{-}$ is computed as

$$\boldsymbol{m}_{k+1}^{-} = \boldsymbol{\Phi}(t_{k+1}; \boldsymbol{m}_k^{+}, t_k). \tag{3.5}$$

Thus, the expectation operator in Eqs. (3.2) and (3.3) can take advantage of the linearity of Eq. (3.4) with respect to the state.
Conversely, the HNEKF sequentially estimates the spacecraft state and the associated uncertainty by incorporating system's nonlinearity in terms of higher-order Taylor expansions. The arbitrary order expansion of the equations of motion and measurement equations can be written, and component-wise reads:

$$\begin{aligned} x_{k+1,i} &= \Phi_i(t_{k+1}; \boldsymbol{m}_k^{+}, t_k) + \textstyle\sum_{r=1}^{v} \frac{1}{r!} \Phi^{i,\gamma_1\dots\gamma_r}_{(t_{k+1},t_k)} \delta x_{k,1}^{\gamma_1} \dots \delta x_{k,m}^{\gamma_r} + w_{k,i}, \\ z_{k+1,p} &= h_p(\boldsymbol{\Phi}(t_{k+1}; \boldsymbol{m}_k^{+}, t_k), t_{k+1}) + \textstyle\sum_{r=1}^{v} \frac{1}{r!} h^{p,\gamma_1\dots\gamma_r}_{(t_{k+1},t_k)} \delta x_{k,1}^{\gamma_1} \dots \delta x_{k,m}^{\gamma_r} + \\ &\quad + v_{k+1,p}, \end{aligned} \tag{3.6}$$

where v is the order of the expansion, $\gamma_i \in \{1, ..., m\}$, $\Phi^{i,\gamma_1\dots\gamma_r}_{(t_{k+1},t_k)}$ includes the higher-order partials of the solution flow, which map the deviations at time k to time $k+1$, and $h^{p,\gamma_1\dots\gamma_r}_{(t_{k+1},t_k)}$ includes the higher-order partials of the measurement function.
The Taylor polynomials of Eq. (3.6) can be inserted into Eqs. (3.2) and (3.3) to obtain the steps of the high-order extended Kalman filter:

1. *Prediction step*: at time t_{k+1}, the mean and covariance of the state vector, $\boldsymbol{m}_{k+1}^{-}$ and $\boldsymbol{P}_{k+1}^{-}$, and the mean of the measurements, $\boldsymbol{n}_{k+1}^{-}$, are estimated as:

$$\begin{aligned} m_{k+1,i}^{-} &= \Phi_i(t_{k+1}; \boldsymbol{m}_k^{+}, t_k) + \textstyle\sum_{r=1}^{v} \frac{1}{r!} \Phi^{i,\gamma_1\dots\gamma_r}_{(t_{k+1},t_k)} E\{\delta x_{k,1}^{\gamma_1} \dots \delta x_{k,m}^{\gamma_r}\}, \\ P_{k+1,ij}^{-} &= \textstyle\sum_{r=1}^{v} \sum_{s=1}^{v} \frac{1}{r!s!} \Phi^{i,\gamma_1\dots\gamma_r}_{(t_{k+1},t_k)} \Phi^{j,\xi_1\dots\xi_s}_{(t_{k+1},t_k)} E\{\delta x_{k,1}^{\gamma_1} \dots \delta x_{k,m}^{\gamma_r} \delta x_{k,1}^{\xi_1} \dots \delta x_{k,m}^{\xi_s}\} + \\ &\quad - \delta m_{k+1}^{i} \delta m_{k+1}^{j} + Q_k^{ij}, \\ n_{k+1,p}^{-} &= h_p(\boldsymbol{\Phi}(t_{k+1}; \boldsymbol{m}_k^{+}, t_k), t_{k+1}) + \textstyle\sum_{r=1}^{v} \frac{1}{r!} h^{p,\gamma_1\dots\gamma_r}_{(t_{k+1},t_k)} E\{\delta x_{k,1}^{\gamma_1} \dots \delta x_{k,m}^{\gamma_r}\}, \end{aligned} \tag{3.7}$$

where $\xi_i \in \{1, ..., m\}$ and $\delta m_{k+1}^{i} = \Phi_i(t_{k+1}; \boldsymbol{m}_k^{+}, t_k) - m_{k+1,i}^{-}$;

2. *Update step*: the new measurements acquired at time t_{k+1}, $\boldsymbol{z}_{k+1}$, are incorporated into the updated estimate of the state vector and covariance matrix as follows:

$$\begin{aligned}
P^{zz}_{k+1,pq} &= \sum_{r=1}^{v}\sum_{s=1}^{v}\frac{1}{r!s!}h^{p,\gamma_1\dots\gamma_r}_{(t_{k+1},t_k)}h^{q,\xi_1\dots\xi_s}_{(t_{k+1},t_k)}E\{\delta x^{\gamma_1}_{k,1}\dots\delta x^{\gamma_r}_{k,m}\delta x^{\xi_1}_{k,1}\dots\delta x^{\xi_s}_{k,m}\}+\\
&\quad -\delta n^{p}_{k+1}\delta n^{q}_{k+1}+R^{pq}_{k+1},\\
P^{xz}_{k+1,ip} &= \sum_{r=1}^{v}\sum_{s=1}^{v}\frac{1}{r!s!}\Phi^{i,\gamma_1\dots\gamma_r}_{(t_{k+1},t_k)}h^{p,\xi_1\dots\xi_s}_{(t_{k+1},t_k)}E\{\delta x^{\gamma_1}_{k,1}\dots\delta x^{\gamma_r}_{k}\delta x^{\xi_1}_{k,m}\dots\delta x^{\xi_s}_{k}\}+\\
&\quad -\delta m^{i}_{k+1}\delta n^{p}_{k+1},\\
\boldsymbol{K}_{k+1} &= \boldsymbol{P}^{xz}_{k+1}(\boldsymbol{P}^{zz}_{k+1})^{-1},\\
\boldsymbol{m}^{+}_{k+1} &= \boldsymbol{m}^{-}_{k+1}+\boldsymbol{K}_{k+1}(\boldsymbol{z}_{k+1}-\boldsymbol{n}^{-}_{k+1}),\\
\boldsymbol{P}^{+}_{k+1} &= \boldsymbol{P}^{-}_{k+1}-\boldsymbol{K}_{k+1}\boldsymbol{P}^{zz}_{k+1}\boldsymbol{K}^{T}_{k+1},
\end{aligned} \tag{3.8}$$

where $\delta n^{p}_{k+1}=h_p(\boldsymbol{\Phi}(t_{k+1};\boldsymbol{m}^{+}_{k},t_k),t_{k+1})-n^{-}_{k+1,p}$.

3.2 The DA-based HNEKF

The DA implementation of the HNEKF relies on the fact that DA can easily provide the arbitrary order Taylor expansion of both $\boldsymbol{\Phi}$ and $\boldsymbol{h}$ in Eq. (3.1). Indeed,$\Phi^{i,\gamma_1\dots\gamma_r}_{(t_{k+1},t_k)}$ and $h^{p,\gamma_1\dots\gamma_r}_{(t_{k+1},t_k)}$ in Eq. (3.7) are obtained by integrating the equations of motion and evaluating the measurement equations in the DA framework. Note that, in order to apply standard HNEFK, each high-order partial is computed by integrating for each time interval a dedicated differential equation that must be derived analytically (see Park and Scheeres [26]). Conversely, in the DA framework, this operation is completely avoided thanks to the fact that the high-order partials are automatically obtained from the DA-based integration of the dynamic system [30]. If the case of variables with Gaussian random distributions is considered, the higher-order moments $E\{\delta x^{\gamma_1}_{k}\dots\delta x^{\gamma_p}_{k}\}$ in Eqs. (3.7)-(3.8) can be completely described, at first, by the first two moments (i.e., mean and covariance), and can be easily computed in terms of the covariance matrix using Isserlis' formula on the monomials of the Taylor polynomial [60]. This is an approximation of the actual propagated probability density function since, due to the nonlinear dynamics, the system loses its Gaussian assumption.

3.2.1 Order comparison

Before showing the results of the DA-based HNEKF applied to the relative pose estimation problem, the effects of considering high-order expansion of the dynamic flow in the extended Kalman filter is discussed.
Consider the illustrative example of an Earth-orbiting spacecraft. The second-order differential equation governing the motion is

$$\frac{d\dot{\boldsymbol{r}}}{dt} = -\frac{\mu}{r^3}\boldsymbol{r}, \tag{3.9}$$

where $\boldsymbol{r} \in \mathbb{R}^3$ is the position vector of the spacecraft and μ is the Earth gravitational parameter. It is assumed that there is no external disturbing force for the system except the gravitational force between the Earth and the spacecraft. The initial true position and velocity assumed for this test are

$$\boldsymbol{x}_0 = \begin{bmatrix} \boldsymbol{r}_0 \\ \boldsymbol{v}_0 \end{bmatrix} = \begin{bmatrix} -0.68787 \\ -0.39713 \\ +0.28448 \\ -0.51331 \\ +0.98266 \\ +0.37611 \end{bmatrix}, \tag{3.10}$$

where the length units are scaled by the orbit semi-major axis (a=8788 km) and the time by $\sqrt{\frac{a^3}{\mu}}$. The initial estimates for the state are 10% off from the true initial state values shown in Eq. 3.10. The adopted initial error covariance is a diagonal matrix with variance 0.01 for the position vector components and 10^{-4} for the velocity vector components. The measurements used in the simulation are the radial position of the spacecraft with respect to the Earth and the line of sight directions to the planet:

$$\begin{aligned} z_1 &= r + v_1, \\ z_2 &= \arctan\left(\frac{y}{x}\right) + v_2, \\ z_3 &= \arcsin\left(\frac{z}{r}\right) + v_3, \end{aligned} \tag{3.11}$$

where $v_i \in \mathbb{R}$, represents the measurement noise. The standard deviation of the measurement error for the radial position is assumed to be 10^{-3} km. The angle error is assumed to be $1.745\ 10^{-6}$ rad following the conventional measurement accuracy for the directional measurement. No process noise is included.

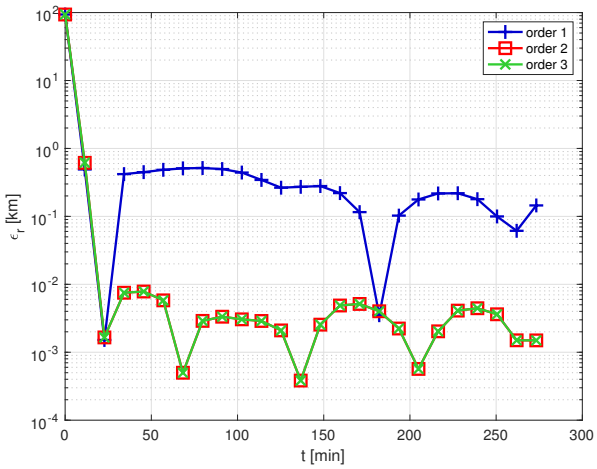

Figure 3.1: *Orbit determination on Keplerian dynamics, 12 measurements per orbit: position error profiles of the DA-based HNEKF at different orders.*

The position and velocity error profiles obtained with the DA-based HNEKF using first, second, and third order expansions are compared in Figs. 3.1 and 3.2. The position and velocity errors, ϵ_r and ϵ_v respectively, are defined as the Euclidean norm of the difference vector between the estimated position and velocity, and the corresponding true vectors. In one orbit a total number of 12 measurements separated by equal time intervals is considered. Note that the results obtained with first order expansions are representative of the performance of a classical EKF scheme. The simulation results show that the estimation accuracy significantly improves when we move from a first order to a second order filter. This confirms that the higher order filters can extract more information from the available nonlinear measurements compared to the first order filter. On the other hand, Figs. 3.1 and 3.2 show that there is no accuracy gain when we use the third order filter, as the errors profiles corresponding to the second and third order basically overlap.
Figures 3.3 and 3.4 show the standard deviation profiles for the spacecraft position and velocity. More specifically, the figures report the quantities

$$\begin{aligned} \sigma_r &= \sqrt{\sigma_{xx}^2 + \sigma_{yy}^2 + \sigma_{zz}^2}, \\ \sigma_v &= \sqrt{\sigma_{vx}^2 + \sigma_{vy}^2 + \sigma_{vz}^2}, \end{aligned} \tag{3.12}$$

where $\sigma_{xx}^2, \sigma_{yy}^2, \sigma_{zz}^2, \sigma_{vx}^2, \sigma_{vy}^2, \sigma_{vz}^2 \in \mathbb{R}$ are the diagonal terms of the estimated covariance matrix. The filter shows the same behavior in terms of accuracy gain when different observation frequencies are adopted. Figures

3.5 and 3.6 show the position error profiles obtained when a total number of 6 and 24 measurements separated by equal time intervals is considered. As can be seen, the results confirm that the estimation accuracy significantly improves when we move from a first to a second order filter and that no further gain is obtained with the third order filter.
The lack of a significant improvement in terms of accuracy between the second and third order filters lies in the basic assumption of Kalman filters, i.e. in the hypothesis that all random distributions are Gaussian and, then, completely described by their mean and covariance.
To get a deeper insight, consider a spacecraft at the pericenter of an elliptical orbit of eccentricity $e = 0.5$, moving in Keplerian dynamics (see Fig. 3.7 for a schematic representation of the example). Assume the lengths are scaled by the orbit pericenter r_p and the time by $\sqrt{r_p^3/\mu}$. Thus, the nominal initial state is:

$$\begin{aligned} x_0 &= 1, \\ y_0 &= 0, \\ z_0 &= 0, \\ v_{x_0} &= 0, \\ v_{y_0} &= \sqrt{1+e}, \\ v_{z_0} &= 0. \end{aligned} \tag{3.13}$$

The initial position of the spacecraft is assumed to be uncertain with stan-

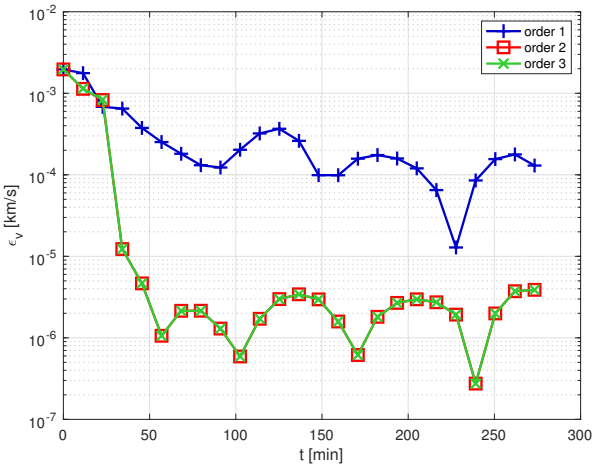

Figure 3.2: *Orbit determination on Keplerian dynamics, 12 measurements per orbit: velocity error profiles of the DA-based HNEKF at different orders.*

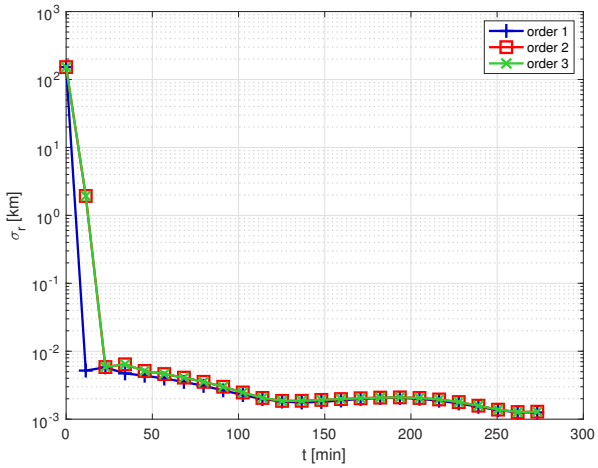

Figure 3.3: *Orbit determination on Keplerian dynamics, 12 measurements per orbit: σ_r profiles of the DA-based HNEKF at different orders.*

dard deviations $3\sigma_x = 0.008$ and $3\sigma_y = 0.08$ on the x and y components of the position vector, with no correlation between the different components. The uncertain initial state is propagated forward to the final epoch $t_f = 0.95\,T$, where $T = 2\pi$ is the nominal period of the orbit. First of all, a Monte Carlo simulation is carried out to propagate 10^5 initial conditions to t_f and to compute the resulting mean and covariance, which are used as reference for the following analysis. As can be seen from Fig. 3.8, the samples of the Monte Carlo simulation at t_f exhibit an evident nonlinear distribution. Using the techniques introduced in Sect. 2.1, DA is then used to compute arbitrary order Taylor expansions of the spacecraft state at t_f with respect to x_0 and y_0. The resulting polynomials are used to compute the propagated mean and covariance using the formulas of Eq. (3.7). Figure 3.8 reports the results obtained for different expansion orders. As shown in the figure, the first order expansion fails to accurately estimate the exact mean and covariance, which are represented by the result of the Monte Carlo simulation. The second order expansion already introduces sufficient information for an accurate representation of both moments. The third order expansion provides only a slight further improvement in terms of accuracy. Thus, being based on a Gaussian representation of the propagated uncertainties, the accuracy of the extended Kalman filter significantly benefits of a second order expansion of the flow of the dynamics. However, no relevant improvement is obtained with higher orders.
The importance of higher order partials emerges in the computation of

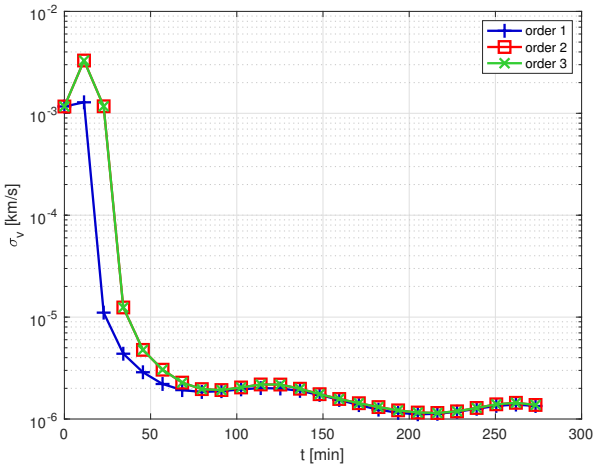

Figure 3.4: *Orbit determination on Keplerian dynamics, 12 measurements per orbit: σ_v profiles of the DA-based HNEKF at different orders.*

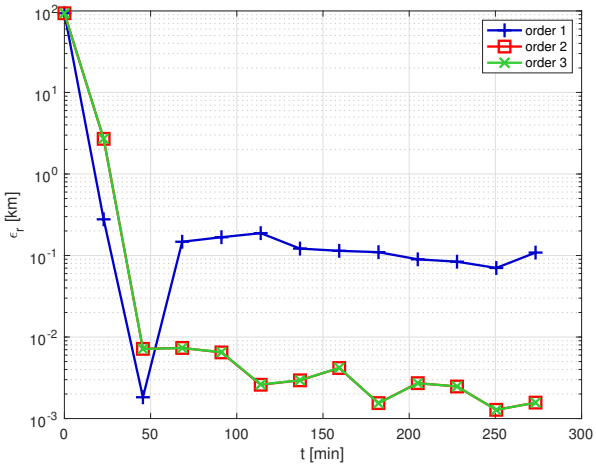

Figure 3.5: *Orbit determination on Keplerian dynamics, 6 measurements per orbit: position error profiles of the DA-based HNEKF at different orders.*

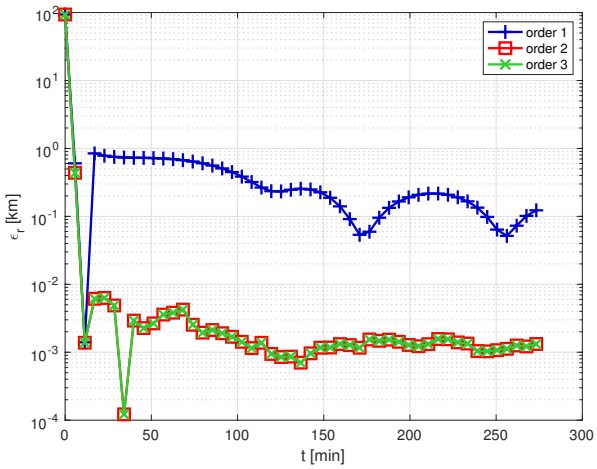

Figure 3.6: *Orbit determination on Keplerian dynamics, 24 measurements per orbit: position error profiles of the DA-based HNEKF at different orders.*

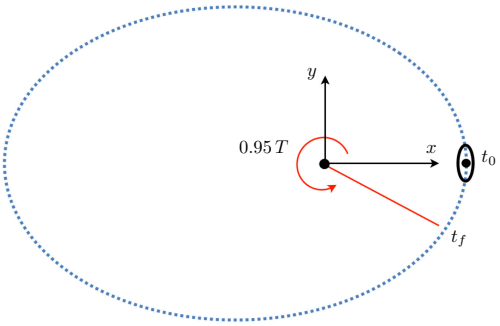

Figure 3.7: *Schematic representation of the illustrative example on the Keplerian dynamics.*

higher order moments. The DA-based estimates of the mean, covariance, skewness, and kurtosis are compared with their values obtained with the Monte Carlo simulation in Table 3.1. More specifically, the following moments are computed [61]:

1. Mean: $\mu = E\{x(t_f)\}$
2. Variance: $\sigma^2 = E\{[x(t_f) - \mu]^2\}$
3. Skewness: $\gamma = E\{[x(t_f) - \mu]^3\}/\sigma^3$
4. Kurtosis: $\kappa = E\{[x(t_f) - \mu]^4\}/\sigma^4 - 3$.

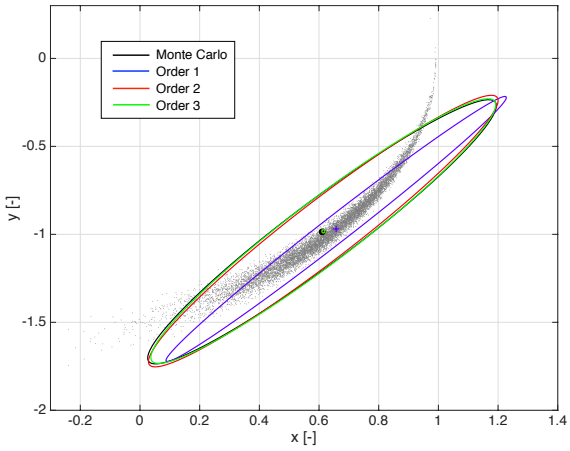

Figure 3.8: *Propagated mean and covariance for the illustrative example on Keplerian dynamics: comparison between a Monte Carlo simulation and the DA-based estimation at different orders. Grey dots represent the propagated samples of the Monte Carlo simulation.*

Table 3.1: *DA-based estimates of the moments for the illustrative example on Keplerian dynamics.*

Moment	Monte Carlo	Order 1	Order 2	Order 3
μ	0.6143	0.6574	0.6142	0.6142
σ	0.0366	0.0353	0.0373	0.0363
γ	-0.5638	0	-0.5548	-0.5662
κ	0.2545	0	0.4247	0.2214

Note that, in the DA-based computation of the moments, $x(t_f)$ is replaced by the corresponding Taylor expansion. Thus, similarly to Eq. (3.7), the computation of the above expectations reduces to the computation of the expectation of the resulting monomials, which can be addressed using Isserlis' formula [62]. As can be seen from Table 3.1, the second order expansion is sufficient to obtain an accurate estimate of the variance. However, a third order expansion is needed to adequately approximate the skewness and the kurtosis. Based on these results, the assessment of the performance of the DA-based HNEKF, applied to the relative pose estimation problem, will be limited to the use of first and second order expansions in the following analyses.

3.3 Relative Pose Estimation

The DA-based HNEKF is proposed to face the challenging problem of estimating the spacecraft relative state for proximity operations during a rendezvous with an uncooperative target. In particular, the ESA e.Deorbit mission [53] is considered as reference and Envisat is selected as target satellite.
In the following analysis, the relative dynamics and kinematics reported in Sect. 2.2 are used and the following assumptions are made. Firstly, an *a priori* knowledge of both chaser and target is assumed, i.e. the inertia properties are perfectly known. Secondly, the chaser motion is supposed to be deterministic and, thus, the related data are not affected by noise and uncertainties. Finally, neither flexible dynamics nor external disturbances are considered. It should be noticed that neglecting external disturbances and flexibility entails the decoupling of the relative translational and rotational dynamics. Decoupling the dynamics is beneficial for the onboard implementation of the DA-based HNEKF, as the number of coefficients needed to represent DA quantities increases almost exponentially with the number of variables. Therefore, decoupling the dynamics grants a significant reduction of the memory requirements.

3.3.1 Measurement model

In real applications, relative position and relative attitude measurements can be obtained by processing images from a camera. In this study, they are generated numerically exploiting a suitable error model.
While the relative position is already part of the state vector, and thus it is linearly related to it, the attitude is provided in terms of roll, pitch and yaw angles. Consequently, it is necessary to derive the rotation matrix $\mathbf{\Gamma}$ from the MRP (see Eq. (2.13)) and afterwards compute the roll, pitch and yaw angles from the associated parameterization:

$$\phi = \arctan(\mathbf{\Gamma}(3,2)/\mathbf{\Gamma}(3,3)), \tag{3.14}$$

$$\theta = \arctan(\mathbf{\Gamma}(2,1)/\mathbf{\Gamma}(1,1)), \tag{3.15}$$

$$\psi = \arcsin(-\mathbf{\Gamma}(3,1)), \tag{3.16}$$

where ϕ, θ, $\psi \in \mathbb{R}$ are the roll, pitch and yaw angles, respectively, whereas $\mathbf{\Gamma}(i,j)$ is the component of the rotation matrix $\mathbf{\Gamma}$ in the position (i,j). It

can be easily observed that the relations binding the MRP and the measured attitude introduce other nonlinearities in the problem.
For the measurements generation, the true states of the target spacecraft are computed during the integration of the dynamic equations (see Sects. 2.2.1-2.2.2). Then, the measured quantities are derived as previously explained and noise is introduced by adopting the exponentially correlated random variable model [63]

$$\tilde{e}(t_{k+1}) = K\tilde{e}(t_k) + \sqrt{1-K^2}\cdot\mathcal{N}(0,\sigma), \tag{3.17}$$

$$K = e^{-1/(f_a\tau)}, \tag{3.18}$$

where $\tilde{e} \in \mathbb{R}$ is the error w.r.t. the true state, $\mathcal{N}(0,\sigma) \in \mathbb{R}$ is a random number generated with a normal distribution of zero mean and standard deviation $\sigma \in \mathbb{R}$, $f_a \in \mathbb{R}$ is the measurement acquisition frequency and $\tau \in \mathbb{R}$ is the autocorrelation time. In this model the error at time $k+1$ is exponentially correlated to the error at the previous instant and this correlation decays with a time scale defined by τ. Considering a camera, this seems to be a more reasonable model with respect to the Gaussian one in which error values at different time instant are completely uncorrelated.

3.3.2 Software architecture

Fig. 3.9 reports the software architecture, which is made up of three main blocks. The first one is the "dynamics simulator+noise generator" that receives as inputs the initial states, then propagates the dynamics through a variable-step integrator (Runge-Kutta78) and generates the measurements adding noise computed with the exponentially correlated random model (Eqs. (3.17)-(3.18)). These computations are performed in advance and the outputs are loaded in memory before running the filter.
For the filtering, the decoupling of the dynamics is exploited to split the problem into two parts: the estimation of the relative translational states ($\boldsymbol{r}_r$ and $\boldsymbol{v}_r$) and the estimation of the relative rotational states ($\boldsymbol{\zeta}$ and $\boldsymbol{\omega}_r$). In this way, six DA variables have to be initialized for each filter instead of twelve, lightening the computational burden. In both filters the required measurements and chaser absolute state are loaded at the beginning and an initial estimate of the relative states, in terms of mean and covariance, has to be provided. For the relative dynamics propagation inside the filter, a 4^{th}-order Runge-Kutta integrator is exploited since it is a better solution for embedded systems in terms of computational effort.
Finally, the estimated relative state is compared with the true state propagated by the dynamics simulator to assess the performance of the filters.

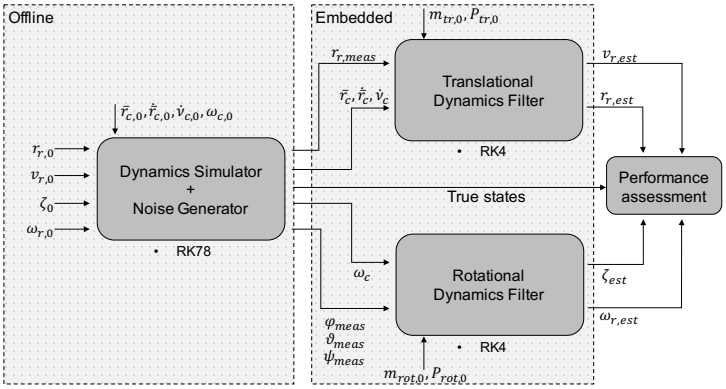

Figure 3.9: *Software architecture.*

3.4 Results

In the numerical analysis, the chaser and the target are assumed to lie on the same orbit at a distance that is compatible with the camera performance. The mass properties of the two spacecraft are listed in Table 3.2. The initial conditions of the relative states are reported in Table 3.3. The attitude is initialized randomly, while the angular velocity is selected in order to have an absolute value of about 2.5 deg/s.
In the following sections, first, the accuracy and robustness of the first and second order filter are assessed, and then an analysis on the required computational time is performed in order to verify the real-time feasibility.

Table 3.2: *Mass properties.*

	Chaser	Target
M (kg)	1435	7828.867
I_{xx} (kgm^2)	2040	17023.3
I_{yy} (kgm^2)	1670	124825.7
I_{zz} (kgm^2)	2570	129112.2
I_{xy} (kgm^2)	130	397.1
I_{xz} (kgm^2)	25	-2171.4
I_{yz} (kgm^2)	-55	344.2

Table 3.3: *Initial conditions.*

Tr. Dyn.		Rot. Dyn.	
x (m)	-0.002	ϕ (rad)	1.66
y (m)	-31.17	θ (rad)	2.27
z (m)	0	ψ (rad)	-0.38
$\dot{x}$ (m/s)	-3.5e-6	$\omega_{r,x}$ (rad/s)	0.02
$\dot{y}$ (m/s)	-2.0e-6	$\omega_{r,y}$ (rad/s)	0.02
$\dot{z}$ (m/s)	0	$\omega_{r,z}$ (rad/s)	0.04

3.4.1 Accuracy and robustness analysis

Before illustrating the results, some comments are provided to guide the reader through the following analyses. First, the target velocity can be assumed to be the most uncertain variable since neither *a priori* knowledge nor direct measurements are available. Then, low measurement acquisition frequencies could be required (or are at least beneficial) for limited-resource systems. Therefore, a Monte-Carlo-based sensitivity analysis is carried out to assess the robustness of the first and second order filter with various acquisition frequencies and initial uncertainty in the relative velocity. In addition, the effects of different initial angular position uncertainties, initial angular rate and level of measurement noise are investigated. The examined cases are reported in Table 3.4 for the translational filter and in Tables 3.5-3.6 for the rotational filter, with $\sigma_{i,0}$ and σ_i^s being the initial standard deviation and the sensor standard deviation, respectively, of the variable i. The factors K and G reported in the tables are used to generate the different levels of uncertainty starting from the nominal one.
Particular attention is paid on the performance of the rotational filter since it has to deal with more complex dynamics. Indeed, the translational dynamics is very slow and almost linear and, thus, less significant results are expected, as it will be shown further.
For each case, 1000 samples are generated around the true initial condi-

Table 3.4: *Translational dynamics: sensitivity to initial velocity uncertainty and acquisition frequency.*

Dynamics		Sensors		Frequency
$\sigma_{r_r,0}$ (m)	1	$\sigma_{x,y}^s$ (m)	0.02	0.1 Hz to 3 Hz
$\sigma_{v_r,0}$ (m/s)	$K \cdot 0.1$	σ_z^s (m)	0.03	
$K = [0.1, 0.5, 1, 5, 10]$				

Table 3.5: *Rotational dynamics: sensitivity to angular velocity uncertainty and acquisition frequency*

Dynamics		Sensors		Initial Conditions		Frequency
$\sigma_{\zeta,0}$ ()	0.002	$\sigma^s_{\phi,\theta}$ (rad)	0.003	$\omega_{r,x}$ (rad/s)	0.1	0.1 Hz
$\sigma_{\omega_r,0}$ (rad/s)	$K \cdot 0.01$	σ^s_{ψ} (rad)	0.006	$\omega_{r,y}$ (rad/s)	0.2	to 3 Hz
				$\omega_{r,z}$ (rad/s)	0.2	
$K = [0.1, 0.5, 1, 5, 10]$						

Table 3.6: *Rotational dynamics: sensitivity to level of measurement noise.*

	Dynamics		Sensors		Frequency
case 1	$\sigma_{\zeta,0}$ ()	$G \cdot 0.002$	$\sigma^s_{\phi,\theta}$ (rad)	$G \cdot 0.003$	3 Hz
	$\sigma_{\omega_r,0}$ (rad/s)	0.01	σ^s_{ψ} (rad)	$G \cdot 0.006$	
case 2	$\sigma_{\zeta,0}$ ()	$G \cdot 0.002$	$\sigma^s_{\phi,\theta}$ (rad)	$G \cdot 0.003$	0.4 Hz
	$\sigma_{\omega_r,0}$ (rad/s)	0.01	σ^s_{ψ} (rad)	$G \cdot 0.006$	
	$G = [1, 2, 4]$				

tions, according to the statistics, and then the furthest 100 are selected and used as initial estimates of the relative states in the filter. This choice is motivated by the will to study the worst circumstances, in which the non-linearities are expected to play a prominent role.
Afterwards, the performance is quantified by means of some statistical indices, reported in Eqs. 3.19-3.20.

$$ {}_n\bar{\mu} = \frac{\sum_{i=1}^{100} RMSE_i}{100}, \tag{3.19} $$

$$ {}_n\sigma_{\bar{\mu}} = \sqrt{\frac{\sum_{i=1}^{100} (\bar{\mu} - RMSE_i)^2}{100}}. \tag{3.20} $$

$RMSE_i \in \mathbb{R}$ is the root mean square error of the estimated variables computed at steady state for the i^{th} simulation, ${}_n\bar{\mu} \in \mathbb{R}$ and ${}_n\sigma_{\bar{\mu}} \in \mathbb{R}$ are the mean and the standard deviation of RMSE, respectively, considering the filter of order n. Figure 3.10 provides a graphical reference for the different indices. $\bar{\mu}$ gives the mean accuracy of the filter, while $\sigma_{\bar{\mu}}$ quantifies the dispersion around the mean. If the standard deviation is high, the final accuracy strongly depends on the estimate of the initial condition and thus large initial errors may result in bad performance or even failure.
In the following, the main outcomes of the simulations are discussed. All the detailed results of the numerical test campaign are reported in [33].

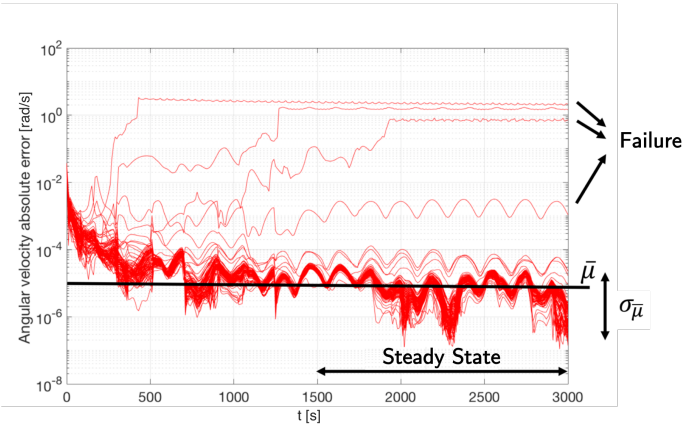

Figure 3.10: *Graphical representation of the statistical indices.*

Translational dynamics filter

As already pointed out, the translational dynamics is slow and almost linear since the two spacecraft are very close on the same orbit, which is nearly circular. Therefore, high-order filters do not provide better performance w.r.t. a linear one, which is already capable of following the dynamic evolution. Indeed, both first and second order filters succeed in all the considered conditions of acquisition frequency and initial velocity uncertainty with the same estimation error at steady state, which is in the order of 10^{-2} m for the position and 10^{-5} m/s for the velocity. As example, in Fig. 3.11 the absolute position and velocity errors considering a frequency of 3 Hz and $\sigma_{v_r,0} = 0.01$ m/s are reported.

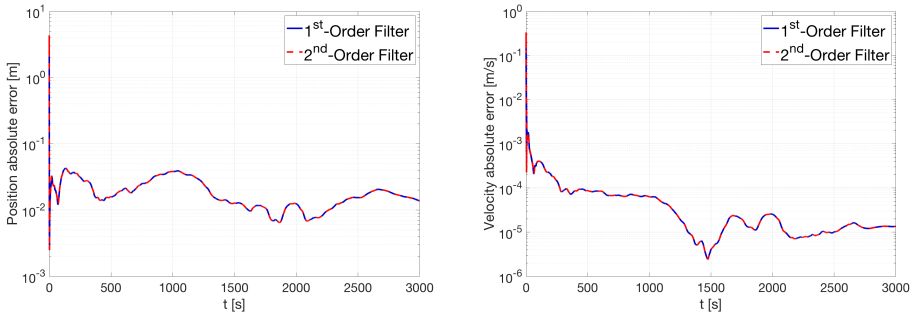

(a) **(b)**

Figure 3.11: *Position (a) and velocity (b) absolute error with a frequency of* 3 *Hz and* $\sigma_{v_r,0} = 0.01$ *m/s.*

Rotational dynamics filter

Regarding the rotational dynamics filter, the nonlinearities affect the estimation problem more significantly, especially in case of high uncertainties and low observability of the system. Focusing initially on the case with the nominal target's initial angular velocity and the uncertainties reported in Table 3.5, the performance of the first order filter, in terms of ${}_1\bar{\mu}$ and ${}_1\sigma_{\bar{\mu}}$, are shown in Tables 3.7-3.8. Analogously, Tables 3.9-3.10 refer to the second order filter. These results are obtained taking into account only the converging solutions. For $\sigma_{\omega_r,0} = 0.1$ rad/s and a frequency of 0.1 Hz, neither of the two filters converge.
However, in order to compare the two filters and have a deeper insight into their performance, the ratios $\frac{{}_2\bar{\mu}}{{}_1\bar{\mu}}$ and $\frac{{}_2\sigma_{\bar{\mu}}}{{}_1\sigma_{\bar{\mu}}}$ are computed and reported in Tab. 3.11-3.12. The superscript reports the success percentage of the second order filter, while the subscript the success percentage of the first order filter. On one hand, it can be observed that first and second order filters show the same performance for low uncertainties and high frequencies. However, moving to high uncertainties and low frequencies, the second order filter starts outperforming the first order one. Indeed, even though ${}_1\bar{\mu}$ is very similar to ${}_2\bar{\mu}$, ${}_1\sigma_{\bar{\mu}}$ is significantly larger than ${}_2\sigma_{\bar{\mu}}$, namely the first order filter features a higher dispersion of the steady-state estimation error (see Fig. 3.12). This means that, in case of large deviations from the true initial conditions, the first order filter performance deteriorates, leading to final estimates that are up to 1 order of magnitude worse than the ones of the second order filter (see Fig. 3.13).
Finally, the second order filter turns out to be also more robust in terms of failures. Indeed, in some cases, the first order filter is not able to deal with the nonlinearity and diverges, while the second order filter converges.

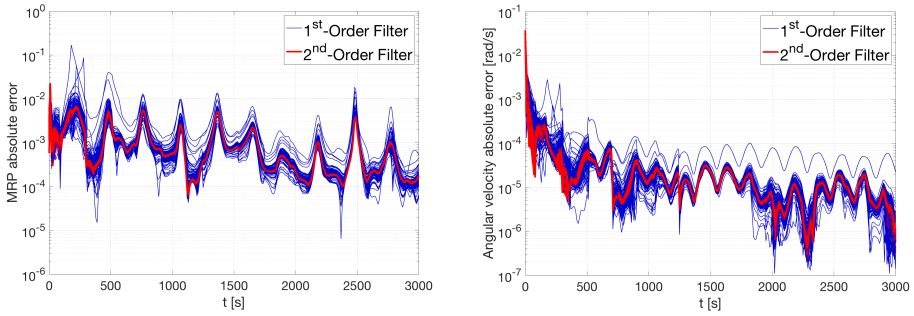

Figure 3.12: *MRP (a) and angular velocity (b) absolute error with a frequency of* 0.1 *Hz and* $\sigma_{\omega_r,0} = 0.01$ *rad/s.*

Table 3.7: ${}_1\bar{\mu}$ *in the sensitivity analysis to initial angular velocity uncertainty and acquisition frequency with nominal initial angular rate of the target.*

Freq.	$\sigma_{\omega_r,0}$ (rad/s)				
(Hz)	0.001	0.005	0.01	0.05	0.1
0.1	7.55e-04	7.59e-04	8.92e-04	3.79e-03	-
0.4	1.16e-03	1.16e-03	1.16e-03	1.29e-03	1.47e-03
1	1.22e-03	1.22e-03	1.22e-03	1.22e-03	1.23e-03
3	5.35e-04	5.35e-04	5.35e-04	5.35e-04	5.35e-04

(a) *Modified Rodrigues Parameters*

Freq.	$\sigma_{\omega_r,0}$ (rad/s)				
(Hz)	0.001	0.005	0.01	0.05	0.1
0.1	1.13e-05	1.13e-05	1.20e-05	3.86e-05	-
0.4	3.91e-06	3.91e-06	3.91e-06	4.45e-06	4.81e-06
1	3.16e-06	3.16e-06	3.16e-06	3.16e-06	3.17e-06
3	3.06e-06	3.07e-06	3.06e-06	3.07e-06	3.07e-06

(b) *Relative Angular Velocity (rad/s)*

Table 3.8: ${}_1\sigma_{\bar{\mu}}$ *in the sensitivity analysis to initial angular velocity uncertainty and acquisition frequency with nominal initial angular rate of the target.*

Freq.	$\sigma_{\omega_r,0}$ (rad/s)				
(Hz)	0.001	0.005	0.01	0.05	0.1
0.1	7.89e-06	1.28e-05	3.24e-04	1.59e-03	-
0.4	5.26e-06	3.40e-06	3.92e-06	3.79e-04	3.38e-04
1	2.56e-06	1.54e-06	1.54e-06	4.70e-06	2.21e-05
3	1.13e-07	7.03e-08	7.19e-08	7.25e-08	1.05e-07

(a) *Modified Rodrigues Parameters*

Freq.	$\sigma_{\omega_r,0}$ (rad/s)				
(Hz)	0.001	0.005	0.01	0.05	0.1
0.1	7.98e-08	6.94e-08	4.24e-06	2.78e-05	-
0.4	2.95e-08	1.61e-08	1.89e-08	1.82e-06	1.95e-06
1	1.92e-09	1.18e-09	1.15e-09	3.54e-09	2.11e-08
3	4.40e-09	2.56e-09	2.34e-09	2.67e-09	3.30e-09

(b) *Relative Angular Velocity (rad/s)*

Table 3.9: ${}_2\bar{\mu}$ *in the sensitivity analysis to initial angular velocity uncertainty and acquisition frequency with nominal initial angular rate of the target.*

Freq.	$\sigma_{\omega_r,0}$ (rad/s)				
(Hz)	0.001	0.005	0.01	0.05	0.1
0.1	7.51e-04	7.51e-04	7.59e-04	9.70e-04	-
0.4	1.16e-03	1.16e-03	1.16e-03	1.16e-03	1.18e-03
1	1.22e-03	1.22e-03	1.22e-03	1.22e-03	1.22e-03
3	5.35e-04	5.35e-04	5.35e-04	5.35e-04	5.35e-04

(a) *Modified Rodrigues Parameters*

Freq.	$\sigma_{\omega_r,0}$ (rad/s)				
(Hz)	0.001	0.005	0.01	0.05	0.1
0.1	1.09e-05	1.09e-05	1.09e-05	1.09e-05	-
0.4	4.61e-06	4.61e-06	4.61e-06	4.61e-06	4.61e-06
1	2.62e-06	2.62e-06	2.62e-06	2.62e-06	2.62e-06
3	1.48e-06	1.48e-06	1.48e-06	1.48e-06	1.48e-06

(b) *Relative Angular Velocity (rad/s)*

Table 3.10: ${}_2\sigma_{\bar{\mu}}$ *in the sensitivity analysis to initial angular velocity uncertainty and acquisition frequency with nominal initial angular rate of the target.*

Freq.	$\sigma_{\omega_r,0}$ (rad/s)				
(Hz)	0.001	0.005	0.01	0.05	0.1
0.1	7.22e-06	6.95e-06	6.89e-06	4.86e-04	-
0.4	5.24e-06	3.38e-06	3.78e-06	3.25e-06	3.93e-05
1	2.56e-06	1.54e-06	1.54e-06	3.01e-06	1.92e-06
3	1.14e-07	7.08e-08	7.23e-08	7.25e-08	9.68e-08

(a) *Modified Rodrigues Parameters*

Freq.	$\sigma_{\omega_r,0}$ (rad/s)				
(Hz)	0.001	0.005	0.01	0.05	0.1
0.1	7.06e-08	5.51e-08	9.31e-08	4.28e-06	-
0.4	2.93e-08	1.60e-08	1.85e-08	2.32e-08	1.52e-07
1	1.90e-09	1.16e-09	1.14e-09	2.26e-09	1.34e-09
3	4.41e-09	2.56e-09	2.35e-09	2.66e-09	3.15e-09

(b) *Relative Angular Velocity (rad/s)*

Table 3.11: $\frac{2\bar{\mu}}{1\bar{\mu}}$ *in the sensitivity analysis to initial angular velocity uncertainty and acquisition frequency with nominal initial angular rate of the target.*

Freq.	$\sigma_{\omega_r,0}$ (rad/s)				
(Hz)	0.001	0.005	0.01	0.05	0.1
0.1	0.994^{100}_{100}	0.993^{100}_{100}	0.850^{100}_{93}	0.255^{50}_{11}	$-^{0}_{0}$
0.4	0.996^{100}_{100}	0.997^{100}_{100}	0.997^{100}_{100}	0.902^{100}_{88}	0.800^{99}_{96}
1	0.988^{100}_{100}	0.989^{100}_{100}	0.989^{100}_{100}	0.991^{100}_{100}	0.996^{100}_{100}
3	1.000^{100}_{100}	1.000^{100}_{100}	1.000^{100}_{100}	1.000^{100}_{100}	1.000^{100}_{100}

(a) *Modified Rodrigues Parameters*

Freq.	$\sigma_{\omega_r,0}$ (rad/s)				
(Hz)	0.001	0.005	0.01	0.05	0.1
0.1	0.998^{100}_{100}	0.998^{100}_{100}	0.941^{100}_{93}	0.334^{50}_{11}	$-^{0}_{0}$
0.4	0.999^{100}_{100}	0.999^{100}_{100}	0.999^{100}_{100}	0.881^{100}_{88}	0.815^{99}_{96}
1	0.999^{100}_{100}	0.999^{100}_{100}	0.999^{100}_{100}	0.999^{100}_{100}	0.997^{100}_{100}
3	1.000^{100}_{100}	1.000^{100}_{100}	1.000^{100}_{100}	1.000^{100}_{100}	1.000^{100}_{100}

(b) *Relative Angular Velocity (rad/s)*

Table 3.12: $\frac{2\sigma_{\bar{\mu}}}{1\sigma_{\bar{\mu}}}$ *in the sensitivity analysis to initial angular velocity uncertainty and acquisition frequency with nominal initial angular rate of the target.*

Freq.	$\sigma_{\omega_r,0}$ (rad/s)				
(Hz)	0.001	0.005	0.01	0.05	0.1
0.1	0.914^{100}_{100}	0.543^{100}_{100}	0.021^{100}_{93}	0.305^{50}_{11}	$-^{0}_{0}$
0.4	0.998^{100}_{100}	0.995^{100}_{100}	0.965^{100}_{100}	0.008^{100}_{88}	0.116^{99}_{96}
1	0.999^{100}_{100}	0.999^{100}_{100}	0.997^{100}_{100}	0.641^{100}_{100}	0.086^{100}_{100}
3	1.000^{100}_{100}	1.000^{100}_{100}	1.000^{100}_{100}	0.999^{100}_{100}	0.919^{100}_{100}

(a) *Modified Rodrigues Parameters*

Freq.	$\sigma_{\omega_r,0}$ (rad/s)				
(Hz)	0.001	0.005	0.01	0.05	0.1
0.1	0.884^{100}_{100}	0.794^{100}_{100}	0.022^{100}_{93}	0.157^{50}_{11}	$-^{0}_{0}$
0.4	0.994^{100}_{100}	0.994^{100}_{100}	0.998^{100}_{100}	0.012^{100}_{88}	0.078^{99}_{96}
1	0.989^{100}_{100}	0.986^{100}_{100}	0.989^{100}_{100}	0.638^{100}_{100}	0.633^{100}_{100}
3	1.000^{100}_{100}	1.000^{100}_{100}	1.000^{100}_{100}	0.998^{100}_{100}	0.955^{100}_{100}

(b) *Relative Angular Velocity (rad/s)*

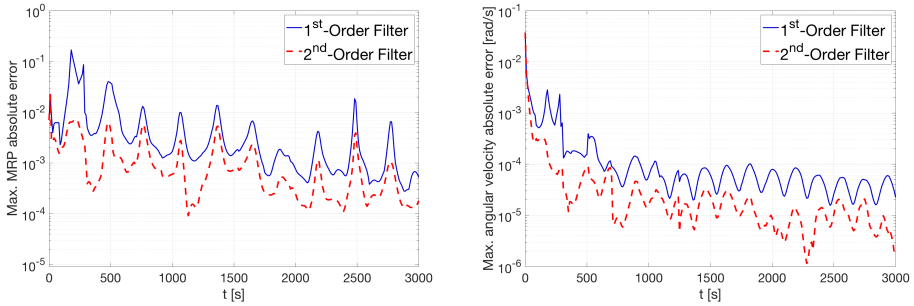

Figure 3.13: *Maximum values of MRP (a) and angular velocity (b) absolute error with a frequency of* 0.1 *Hz and* $\sigma_{\omega_r,0} = 0.01$ *rad/s.*

The analyses of the other examined cases provide similar results and stress the superiority of the second order filter for high uncertainties and low acquisition frequencies. The same result is obtained for the different levels of measurement noise as reported in Tables 3.13 and 3.14. In fact, higher uncertainties, either in dynamics knowledge or in the measurements (Tables 3.5-3.6, respectively), cause an increase of the final error dispersion of the linear filter and thus a worse performance deterioration with respect to the nonlinear one, leading to errors up to two orders of magnitude larger. When the initial angular rate is increased, the area in which the second order filter is more robust becomes larger, for equal uncertainty and frequency domain, see Tables 3.15-3.16. This case is similar to reducing the acquisition frequency and thus the observability of the system, increasing nonlinearity effects.

Table 3.13: $\frac{2\bar{\mu}}{1\bar{\mu}}$ *in the sensitivity analysis to the levels of measurement noise from Table 3.6.*

Freq. (Hz)	G		
	1	2	4
0.4	0.997^{100}_{100}	0.960^{99}_{91}	0.994^{98}_{75}
3	1.000^{100}_{100}	1.000^{100}_{100}	0.999^{99}_{99}

(a) *Modified Rodrigues Parameters*

Freq. (Hz)	G		
	1	2	4
0.4	0.999^{100}_{100}	0.973^{99}_{91}	1.004^{98}_{75}
3	1.000^{100}_{100}	1.001^{100}_{100}	1.000^{99}_{99}

(b) *Relative Angular Velocity (rad/s)*

Table 3.14: $\frac{2\sigma_{\bar{\mu}}}{1\sigma_{\bar{\mu}}}$ *in the sensitivity analysis to the levels of measurement noise from Table 3.6.*

Freq.	G		
(Hz)	1	2	4
0.4	0.965^{100}_{100}	0.042^{99}_{91}	0.037^{98}_{75}
3	1.000^{100}_{100}	1.020^{100}_{100}	0.887^{99}_{99}

(a) *Modified Rodrigues Parameters*

Freq.	G		
(Hz)	1	2	4
0.4	0.998^{100}_{100}	0.033^{99}_{91}	0.088^{98}_{75}
3	1.000^{100}_{100}	1.002^{100}_{100}	1.023^{99}_{99}

(b) *Relative Angular Velocity (rad/s)*

Table 3.15: $\frac{2\bar{\mu}}{1\bar{\mu}}$ *in the sensitivity analysis to initial angular velocity uncertainty and acquisition frequency with increased initial angular rate of the target (see Table 3.5).*

Freq.	$\sigma_{\omega_r,0}$ (rad/s)				
(Hz)	0.001	0.005	0.01	0.05	0.1
0.1	0.975^{86}_{83}	0.923^{95}_{95}	0.620^{94}_{40}	$-^{0}_{0}$	$-^{0}_{0}$
0.4	0.996^{100}_{100}	0.996^{95}_{95}	0.996^{96}_{96}	0.939^{98}_{88}	0.803^{91}_{75}
1	0.996^{100}_{100}	0.996^{98}_{98}	0.996^{96}_{96}	0.996^{98}_{98}	0.991^{97}_{95}
3	1.000^{100}_{100}	1.000^{100}_{100}	1.000^{100}_{100}	1.000^{100}_{100}	1.000^{100}_{100}

(a) *Modified Rodrigues Parameters*

Freq.	$\sigma_{\omega_r,0}$ (rad/s)				
(Hz)	0.001	0.005	0.01	0.05	0.1
0.1	0.906^{86}_{83}	0.957^{95}_{95}	0.458^{94}_{40}	$-^{0}_{0}$	$-^{0}_{0}$
0.4	1.001^{100}_{100}	1.001^{95}_{95}	1.001^{96}_{96}	0.533^{98}_{88}	0.396^{91}_{75}
1	0.999^{100}_{100}	0.999^{98}_{98}	0.999^{96}_{96}	0.999^{98}_{98}	0.995^{97}_{95}
3	0.998^{100}_{100}	0.998^{100}_{100}	0.998^{100}_{100}	0.998^{100}_{100}	0.998^{100}_{100}

(b) *Relative Angular Velocity (rad/s)*

Table 3.16: $\frac{2\sigma_{\bar{\mu}}}{1\sigma_{\bar{\mu}}}$ *in the sensitivity analysis to initial angular velocity uncertainty and acquisition frequency with increased initial angular rate of the target (see Table 3.5).*

Freq.	$\sigma_{\omega_r,0}$ (rad/s)				
(Hz)	0.001	0.005	0.01	0.05	0.1
0.1	0.826^{86}_{83}	0.124^{95}_{95}	0.037^{94}_{40}	$-^{0}_{0}$	$-^{0}_{0}$
0.4	0.979^{100}_{100}	0.974^{95}_{95}	0.921^{96}_{96}	0.009^{98}_{88}	0.364^{91}_{75}
1	0.995^{100}_{100}	0.994^{98}_{98}	0.992^{96}_{96}	0.598^{98}_{98}	0.027^{97}_{95}
3	1.005^{100}_{100}	1.000^{100}_{100}	1.004^{100}_{100}	1.007^{100}_{100}	0.960^{100}_{100}

(a) *Modified Rodrigues Parameters*

Freq.	$\sigma_{\omega_r,0}$ (rad/s)				
(Hz)	0.001	0.005	0.01	0.05	0.1
0.1	0.832^{86}_{83}	0.169^{95}_{95}	0.080^{94}_{40}	$-^{0}_{0}$	$-^{0}_{0}$
0.4	1.013^{100}_{100}	0.996^{95}_{95}	0.964^{96}_{96}	0.005^{98}_{88}	0.154^{91}_{75}
1	1.016^{100}_{100}	1.074^{98}_{98}	1.064^{96}_{96}	0.696^{98}_{98}	0.362^{97}_{95}
3	1.008^{100}_{100}	1.008^{100}_{100}	1.001^{100}_{100}	1.008^{100}_{100}	0.972^{100}_{100}

(b) *Relative Angular Velocity (rad/s)*

3.4.2 Computational time on the BeagleBone Black

This section addresses the assessment of the required computational effort of the DA-based HNEKF on the BeagleBone Black (BBB) Single Board Computer, based on an ARMv7 processor (Cortex A8) @ 1GHz with 512Mb of RAM. The BBB is deemed to be representative of the limited computational capability available on onboard space processors. The filter is entirely compiled out of C11 code directly on the target ARM platform, which is running a tailored Linux 4.9 kernel and proper GCC compiler.
In order to asses the feasibility of the developed filter on the embedded hardware, a Real-Time Operative System (RTOS) should have been employed, allowing the real time scheduling of the filter task at the desired frequency. However, the filter does not really acquire measurements since those are generated in advance by the dynamics simulator. Therefore, an accurate real time scheduling is not strictly required. Indeed, the computational time required by each step of the filter can be measured and compared to the time step at the desired frequency, checking that it is smaller.
To this aim, the duty cycle concept is introduced. The duty cycle represent the fraction of the available sampling time which is used by the filter task.

Therefore, given the execution time t_{exec} and defining the sampling time as

$$t_a = \frac{1}{f_a}, \tag{3.21}$$

the duty cycle is:

$$DC = \frac{t_{exec}}{t_a}. \tag{3.22}$$

The analysis is carried out considering different sampling frequencies and processor clock frequencies on the BBB. More specifically, the sampling frequencies are $f_a = [0.1, 0.4, 1, 3]$ Hz while the clock frequencies are $clk = \left[100^1, 275, 720, 1000\right]$ MHz. First and second order filters are executed considering both the translational and rotational dynamics. The results of the execution time and duty cycle are reported in Table 3.17.

Table 3.17: *Filter execution on BBB.*

Execution Time [s] - Order 1				
$f_a \backslash$clk	100	275	720	1000
0.1	0.381	0.303	0.110	0.006
0.4	0.115	0.091	0.035	0.004
1	0.062	0.049	0.018	0.002
3	0.026	0.021	0.008	0.001

Duty Cycle [%] - Order 1				
$f_a \backslash$clk	100	275	720	1000
0.1	3.8%	1.2%	0.1%	0.0%
0.4	4.6%	0.4%	0.0%	0.0%
1	6.2%	0.3%	0.0%	0.0%
3	7.8%	0.2%	0.0%	0.0%

Execution Time [s] - Order 2				
$f_a \backslash$clk	100	275	720	1000
0.1	1.342	1.072	0.413	0.043
0.4	0.426	0.339	0.129	0.014
1	0.25	0.199	0.077	0.011
3	0.124	0.099	0.039	0.007

Duty Cycle [%] - Order 2				
$f_a \backslash$clk	100	275	720	1000
0.1	13.4%	14.4%	5.9%	0.3%
0.4	17.0%	5.8%	0.7%	0.0%
1	25.0%	5.0%	0.4%	0.0%
3	37.2%	3.7%	0.1%	0.0%

It is clear that both first and second order filters are always feasible, as the duty cycle remains always well below the 50%, thus allowing for the filtering and also other necessary tasks. Not surprisingly, the duty cycle increases when reducing the clock frequency as the processor is capable of executing less operation per seconds. Moreover, at constant clock frequency, the duty cycle reduces when reducing the sampling frequency, demonstrating that the longer propagation time span, needed for computing the expectations, is not highly influencing the overall computational time. Concentrating on the lower clock frequency, it is possible to see how the second order filter is more feasible at lower sampling frequencies, that are the cases in which this filter outperforms the first order version.

[1] Interpolated

CHAPTER 4

Relative pose estimation through DA-based UKF

After introducing the DA-based HNEKF, another Kalman filter is implemented in the DA framework: the unscented Kalman filter. It is shown that the DA-based UKF is computationally lighter than the standard version. The performance for the relative pose estimation problem is assessed and a comparison with the DA-based HNEKF is performed, considering both accuracy and computational time.

4.1 Unscented Kalman filter

Differently from the HNEKF, in the unscented Kalman filter the prediction step relies on the unscented transformation (UT). Such transformation is based on the intuition that *it is easier to approximate a Gaussian (probability) distribution than to approximate an arbitrary nonlinear function or transformation* (see [64] [65] [66]). Following this statement, the aim of the unscented transformation is to find a parametrization which accurately describes the mean and the covariance information of the initial variable and, at the same time, permits the direct propagation of the information through

the set of nonlinear equations (e.g. functions, transformations,..). In order to approximate the mean $\boldsymbol{m}$ and covariance $\boldsymbol{P}$ of the m-dimensional state vector $\boldsymbol{x}$, a set of $2m+1$ sigma points, collected in a structure $\mathcal{X}$, are exploited and computed as follows:

$$\mathcal{X}^{\{1\}} = \boldsymbol{m}, \tag{4.1}$$

$$\mathcal{X}^{\{i\}} = \boldsymbol{m} + (\sqrt{(m+\lambda)\boldsymbol{P}}\,)_{i-1}, \qquad i = 2, ..., m+1 \tag{4.2}$$

$$\mathcal{X}^{\{i\}} = \boldsymbol{m} - (\sqrt{(m+\lambda)\boldsymbol{P}}\,)_{i-m-1}, \qquad i = m+2, ..., 2m+1 \tag{4.3}$$

where $\lambda \in \mathbb{R}$ is a scaling parameter, while $(\sqrt{(m+\lambda)\boldsymbol{P}}\,)_i$ is the *i*th row or column of the matrix square root of $(m+\lambda)\boldsymbol{P}$. Defining $\boldsymbol{S} \in \mathbb{R}^{m \times m}$ such that $\boldsymbol{P} = \boldsymbol{S}\boldsymbol{S}$, the matrix square root is computed through diagonalization:

$$\begin{aligned}
\boldsymbol{P} &= \boldsymbol{V}\boldsymbol{D}\boldsymbol{V}^{-1} \\
&= \boldsymbol{V} \begin{bmatrix} d_{11} & \dots & 0 \\ 0 & \ddots & 0 \\ 0 & \dots & d_{mm} \end{bmatrix} \boldsymbol{V}^{-}1 \\
&= \boldsymbol{V} \begin{bmatrix} \sqrt{d_{11}} & \dots & 0 \\ 0 & \ddots & 0 \\ 0 & \dots & \sqrt{d_{mm}} \end{bmatrix} \begin{bmatrix} \sqrt{d_{11}} & \dots & 0 \\ 0 & \ddots & 0 \\ 0 & \dots & \sqrt{d_{mm}} \end{bmatrix} \boldsymbol{V}^{-}1.
\end{aligned} \tag{4.4}$$

Therefore, the matrix square root of the covariance $\boldsymbol{P}$ can be obtained as

$$\boldsymbol{S} = \boldsymbol{V} \begin{bmatrix} \sqrt{d_{11}} & \dots & 0 \\ 0 & \ddots & 0 \\ 0 & \dots & \sqrt{d_{mm}} \end{bmatrix} \boldsymbol{V}^{-1}, \tag{4.5}$$

so that:

$$\boldsymbol{S}\boldsymbol{S} = (\boldsymbol{V}\boldsymbol{D}^{1/2}\boldsymbol{V}^{-1})(\boldsymbol{V}\boldsymbol{D}^{1/2}\boldsymbol{V}^{-1}) = \boldsymbol{P}. \tag{4.6}$$

In this study the Cholesky Matrix Square Root is adopted. This decomposition, often used in UKF implementation, is efficient and stable, and thus particularly suitable for real-time estimation [67] [65].
Defined the sigma points, two weights are associated to each of them, computed as

$$w_{m,1} = \frac{\lambda}{m+\lambda}, \tag{4.7}$$

$$w_{P,1} = w_{m,1} + (1 - \alpha^2 + \beta), \tag{4.8}$$

$$w_{m,i} = w_{P,i} = \frac{1}{2(m+\lambda)}, \qquad i = 2, ..., 2m+1 \tag{4.9}$$

where $w_{m,i} \in \mathbb{R}$ is a weight referred to the mean, while $w_{P,i} \in \mathbb{R}$ is referred to the covariance. Parameters $k \geq 0$ and $\alpha \in (0, 1]$ define how far from the mean the sigma points are located. β is typically chosen equal to 2, since this value is the optimal choice for Gaussian distributions. Finally, λ is a combination of the other parameters:

$$\lambda = \alpha^2(m + k) - m. \tag{4.10}$$

It can be noted that there is no unique solution for the sigma points vector and the weights vectors, thus the sigma points can (but do not have to) lie on the main axes of the covariance matrix. However, the selection must be such that the following equations are respected:

$$\sum_{i=1}^{2m+1} w_i = 1, \tag{4.11}$$

$$\boldsymbol{m} = \sum_{i=1}^{2m+1} w_{m,i} \mathcal{X}^{\{i\}}, \tag{4.12}$$

$$\boldsymbol{P} = \sum_{i=1}^{2m+1} w_{P,i} (\mathcal{X}^{\{i\}} - \boldsymbol{m})(\mathcal{X}^{\{i\}} - \boldsymbol{m})^T. \tag{4.13}$$

The UKF prediction starts with a set of sigma points around the initial conditions, and their relative weights. Afterwards, the set gets transformed by initializing each sigma point through the process model (consider also here the generic dynamic system in Eq. (3.1)), giving the transformed set

$$\mathcal{X}_{k+1}^{\{i\}} = \boldsymbol{\Phi}(t_{k+1}; \mathcal{X}_k^{\{i\}}, t_k). \tag{4.14}$$

Finally, the mean and the covariance of the propagated set is evaluated by weighting each transferred sigma point:

$$\boldsymbol{m}_{k+1}^- = \sum_{i=1}^{2m+1} w_{m,i} \mathcal{X}_{k+1}^{\{i\}}, , \tag{4.15}$$

$$\boldsymbol{P}_{k+1}^- = \sum_{i=1}^{2m+1} w_{P,i} \{\mathcal{X}_{k+1}^{\{i\}} - \boldsymbol{m}_{k+1}^-\}\{\mathcal{X}_{k+1}^{\{i\}} - \boldsymbol{m}_{k+1}^-\}^T. \tag{4.16}$$

The same approach is adopted for the measurement vector, where each sigma point goes through the observation model (Eq. (3.1)), and then the predicted measurements are calculated:

$$\mathcal{Z}_{k+1}^{\{i\}} = \boldsymbol{h}(\mathcal{X}_{k+1}^{\{i\}}, t_{k+1}), \tag{4.17}$$

$$\boldsymbol{n}_{k+1}^{-} = \sum_{i=1}^{2m+1} w_{m,i} \mathcal{Z}_{k+1}^{\{i\}}. \tag{4.18}$$

Since the observation noise is independent and additive, the covariance matrix of the measurement and the cross-covariance matrix of the state and the measurement are evaluated as:

$$\boldsymbol{P}_{k+1}^{zz} = \sum_{i=1}^{2m+1} w_{P,i} \{\mathcal{Z}_{k+1}^{\{i\}} - \boldsymbol{n}_{k+1}^{-}\} \{\mathcal{Z}_{k+1}^{\{i\}} - \boldsymbol{n}_{k+1}^{-}\}^T + \boldsymbol{R}_{k+1}, \tag{4.19}$$

$$\boldsymbol{P}_{k+1}^{xz} = \sum_{i=1}^{2m+1} w_{P,i} \{\mathcal{X}_{k+1}^{\{i\}} - \boldsymbol{m}_{k+1}^{-}\} \{\mathcal{Z}_{k+1}^{\{i\}} - \boldsymbol{n}_{k+1}^{-}\}^T. \tag{4.20}$$

This completes the UKF prediction process and the filtering can continue with the update equations of the classical Kalman filter.

4.2 DA-based UKF

The UKF can be developed into the DA framework becoming the DA-based unscented Kalman filter (UKFDA). This filter provides an improvement by reducing the computational time of the classical UKF when the equations of motion are complex. DA is used to Taylor expand the function $\boldsymbol{\Phi}$ in Eq. (3.1): as a result, it builds an analytical map that connects the state at time k with the state at time $k+1$. The resulting polynomials can be evaluated to map the sigma points through the model equations, replacing multiple integrations of $\boldsymbol{\Phi}$. Consequently, the DA-based approach tends to outperform the classical one when the integration of $\boldsymbol{\Phi}$ is computationally demanding. The order at which the Taylor polynomial is computed can be arbitrarily selected.

More specifically, at each step, the state $\boldsymbol{x}$ is initialized as DA variable around the current mean and propagated in the DA framework through the equations of motions and of the measurements. Then the polynomials are evaluated at the sigma points. The distance of each sigma point is known and given by the columns (or rows) of the matrix $\boldsymbol{S} = \pm\sqrt{(m+\lambda)\boldsymbol{P}}$. The sigma points are propagated by simply evaluating the Taylor expansion at

each column of $\boldsymbol{S}$. As a results, the UKFDA turns out to be faster than the plain UKF. Figure 4.1 gives a visual idea of the different propagation technique used by the two unscented Kalman filters.

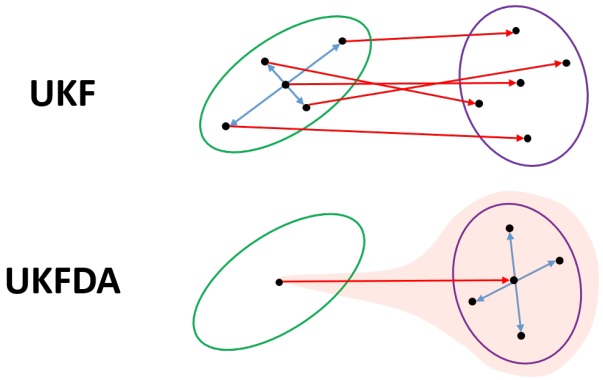

Figure 4.1: *The propagation approaches of the sigma points in the UKF, classic, and UKFDA, through polynomial transition map.*

4.3 Relative Pose Estimation

As for the DA-based HNEKF, the ESA's e.Deorbit mission is taken as reference. Again the relative dynamics and kinematics introduced in Sect. 2.2 are used and the same assumptions done for the HNEKF are valid hereafter. In the following, a more realistic measurement model is introduced for the assessment of the performance of the DA-based UKF.

4.3.1 Measurement model

In real applications, the image processing software is set up to look for some target points in each image taken: these points are referred to as markers [68]. Therefore, a measurement model that considers marker positions instead of directly states is developed. The software processes the image sent from the camera and analyses it: once the position of the markers is found, it sends this information to the filter. A common solution is to select the target corners as markers. Assuming to have information about Envisat's mass, dimensions, center of mass (CM) location, moments of inertia, geometrical center (GC) and volume [69], markers can provide information about the spacecraft position and attitude, since their location with respect to the center of mass ($\boldsymbol{\varrho}_i \in \mathbb{R}^3$), in the target body-fixed reference frame, is known (see Table 4.1).
Envisat main body, without the solar panel, can be described as a simple

parallelepiped with 8 corners: these corners have been selected as the filter markers. Each marker is called with an alphabetical letter in order to have a clear identification: marker A, B, C, D, E, F, G, and H.

Table 4.1: *Assumed Envisat markers position vectors with respect to its center of mass.*

Marker	$\boldsymbol{\varrho}_i$ [m]		
A	+8.9150	+1.3840	+1.5970
B	+8.9150	+1.3840	-1.6030
C	+8.9150	-1.3660	-1.6030
D	+8.9150	-1.3660	+1.5970
E	-1.1050	+1.3840	+1.5970
F	-1.1050	+1.3840	-1.6030
G	-1.1050	-1.3660	-1.6030
H	-1.1050	-1.3660	+1.5970

Being $\boldsymbol{r}_r$ the position vector of the target center of mass with respect to the chaser center of mass, the measurements are calculated separately for each single marker in the following way:

$$\boldsymbol{z}_i = \boldsymbol{\Gamma}^T \boldsymbol{\varrho}_i + \boldsymbol{r}_r, \qquad i = A, \ldots, H \tag{4.21}$$

where $\boldsymbol{z}_i \in \mathbb{R}^3$ is the position of marker i with respect to the chaser center of mass and the rotation matrix $\boldsymbol{\Gamma}$ comes from the knowledge of the MRP. Afterwards, noise is introduced additively as an exponentially correlated random variable according to the model reported in Eqs. 3.17-3.18.
The camera is not able to locate all the markers position in one single frame due to the fact that Envisat structure will cover some markers. The visibility and the correct association of a corner to the correspondent marker is fundamental since the larger the number of located markers the better the estimation accuracy. Therefore, the markers visibility must be assessed.
When thinking about visibility of the corners of a parallelepiped, it is better to understand which face of the parallelepiped is visible and then associate the respective corners. Basically, there are only three different options: 1, 2 or 3 faces are visible, and thus 4, 6 or 7 markers are visible in each frame.
In order to implement this process, a set of unit vectors $\hat{\boldsymbol{\eta}}_i \in \mathbb{R}^3$, with $i = \alpha, \ldots, \zeta$ indicating the faces, is defined in the target body-fixed reference frame. In Table 4.2 the faces with the associated markers and unit vectors are listed.
The requirement for the face visibility is expressed by the following inequality:

$$\boldsymbol{r}_r \cdot \boldsymbol{\Gamma}^T \hat{\boldsymbol{\eta}}_i < 0. \tag{4.22}$$

Table 4.2: *Envisat main body faces and visible markers relations.*

Face	$\hat{\eta}_i$	Markers Seen
$\boldsymbol{\alpha}$	$\hat{\eta}_\alpha = \begin{bmatrix} 1 \\ 0 \\ 0 \end{bmatrix}$	A - B - C - D
$\boldsymbol{\beta}$	$\hat{\eta}_\beta = \begin{bmatrix} 0 \\ 1 \\ 0 \end{bmatrix}$	A - B - E - F
$\boldsymbol{\gamma}$	$\hat{\eta}_\gamma = \begin{bmatrix} 0 \\ 0 \\ 1 \end{bmatrix}$	A - D - E - H
$\boldsymbol{\delta}$	$\hat{\eta}_\delta = \begin{bmatrix} -1 \\ 0 \\ 0 \end{bmatrix}$	E - F - G - H
$\boldsymbol{\epsilon}$	$\hat{\eta}_\epsilon = \begin{bmatrix} 0 \\ -1 \\ 0 \end{bmatrix}$	C - D - G - H
$\boldsymbol{\zeta}$	$\hat{\eta}_\zeta = \begin{bmatrix} 0 \\ 0 \\ -1 \end{bmatrix}$	B - C - F - G

If the scalar product between the relative chaser-target position vector and the unit vector perpendicular to the face is negative, it means that the face is looking forward the camera and the markers associated to the face are visible.
In the following, the performance of the filters will be assessed both exploiting the whole set of available markers, which means a shape-shifting measurement vector that adapts to the number of visible markers for each acquisition, and limiting the set to three markers, namely the minimum number to derive the target state.
In the latter case, the selection of the markers is based on a simple criterion: the filter has to work with the 3 markers creating the triangle with the largest area on the plane of sight. The plane of sight, from now on called π_1, is the plane defined by the relative position chaser-target vector and passing through the target center of mass. This plane gives information on how the camera sees the target. Therefore, each marker is projected on π_1 and its projection represents the vertex of a number of triangles depending on the number of visible markers. Afterwards, the area of the triangles is evaluated and the maximum one is selected.

The marker projection is performed as follows:

$$b_i = \frac{\boldsymbol{r}_r}{||\boldsymbol{r}_r||} \cdot \boldsymbol{\Gamma}^T \boldsymbol{\varrho}_i, \tag{4.23}$$

$$\tilde{\boldsymbol{\varrho}}_i = \boldsymbol{\Gamma}^T \boldsymbol{\varrho}_i - b_i \frac{\boldsymbol{r}_r}{||\boldsymbol{r}_r||}, \tag{4.24}$$

where $\tilde{\boldsymbol{\varrho}}_i \in \mathbb{R}^3$ is the vector projection of the marker i on π_1, and $b_i \in \mathbb{R}$ is the scalar projection of the marker vector $\boldsymbol{\varrho}_i$ on direction $\frac{\boldsymbol{r}_r}{||\boldsymbol{r}_r||}$.
In order to identify the markers forming the triangle with the maximum area, it is convenient to notice that Envisat geometrical model is a slender parallelepiped with one predominant principal inertia axis $\tilde{\boldsymbol{\upsilon}}$, expressed here in the chaser body-fixed reference frame, and subdivide the markers into two groups at the ends of this axis: the $master$ group and $slave$ group. The former group presents more visible markers than the latter one. Then, it is possible to define a line l through a versor $\hat{\boldsymbol{\upsilon}} \in \mathbb{R}^3$ obtained by projecting the axis $\tilde{\boldsymbol{\upsilon}} \in \mathbb{R}^3$ on plane π_1, as reported below:

$$\hat{\boldsymbol{\upsilon}} = \tilde{\boldsymbol{\upsilon}} - (\frac{\boldsymbol{r}_r}{||\boldsymbol{r}_r||} \cdot \tilde{\boldsymbol{\upsilon}}) \frac{\boldsymbol{r}_r}{||\boldsymbol{r}_r||}. \tag{4.25}$$

The markers combination that has the triangle with the largest area can be directly found by selecting the two furthest marker projections from line l in the $master$ group and the nearest marker projection in the $slave$ group. The distance $d_i \in \mathbb{R}$ of each marker projection from line l is evaluated in the following way:

$$d_i = ||\tilde{\boldsymbol{\varrho}}_i \times \hat{\boldsymbol{\upsilon}}||. \tag{4.26}$$

Virtually, 56 combinations of 3 markers can be identified, since the total number of markers is 8. However, some combinations are physically impossible due to Envisat geometry model, i.e. opposite markers can not be visible at the same time. Hence, there are 4 pairs of markers that will never be part of the same group: AG, BH, CE and DF, and they lead to a total of 24 $impossible$ combinations. Moreover, 3 markers belonging to the same side of the parallelepiped can not be chosen, and thus only 24 combination are actually allowed. Table 4.3 reports and classifies all the combinations of 3 markers.

4.3.2 Software architecture

Also in this case the software architecture is reported (Fig. 4.2). Similarly to the DA-based HNEKF, the first block is the "dynamics simulator+noise

Table 4.3: *Classification of all possible combination of 3 markers.*

	Groups							
impossible	ABG	ACG	ADG	AEG	AFG	AGH	ABH	BCH
	BDH	BEH	BFH	BGH	ACE	BCE	CDE	CEF
	CEG	CEH	ADF	BDF	CDF	DEF	DFG	DFH
forbidden	ABC	ABD	BCD	ACD	EFG	EFH	FGH	EGH
allowed	ABE	ABF	BCF	BCG	CDH	CDG	ADE	ADH
	ACF	ACH	BDE	BDG	AEF	BEF	BFG	CFG
	CGH	DGH	AEH	DEH	BEG	DEG	AFH	CFH

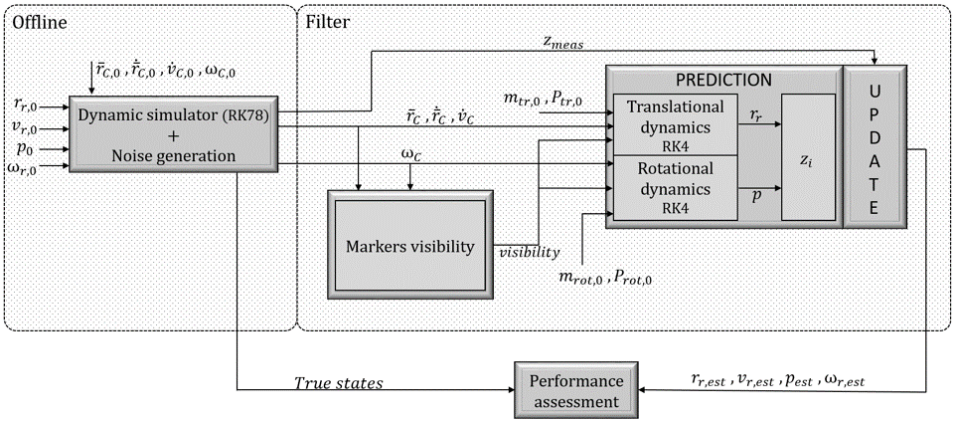

Figure 4.2: *Software architecture.*

generator" that receives as inputs the initial states, then propagates the dynamics through a variable-step integrator (Runge-Kutta78) and generates the measurements adding noise computed with the exponentially correlated random model (Eqs. 3.17-3.18). These computations are performed in advance and the outputs are loaded in memory before running the filter.

For the filtering, the decoupling of the equations of motion can be exploited to separate the propagation of the two dynamics, translational and rotational, leading to a faster and more efficient algorithm. Also in this case, a fixed-step integrator is used, because computationally lighter. On the other hand, and differently from the situation presented in the previous chapter, the translational and rotational information has to be used jointly to estimate the measurements, since the measurement equations are coupled.

The filter is initialized providing an initial estimate of the relative states in terms of mean and covariance. Moreover, before starting the estimation, the filter uses the information of the previous step to calculate the markers visibility.

Finally, the estimated relative state is compared with the true state propagated by the dynamics simulator to assess the performance of the filters.

4.4 Results

The simulation scenario used to assess the performance of the DA-based UKF is the same presented in Sect. 4.4 for the DA-based HNEKF. The initial condition are reported in Table 3.3. The attitude is initialized randomly, while the angular velocity is selected in order to have an absolute value of about 2.5 deg/s.
In this section, the performance of the DA-based UKF, of the standard UKF and of the DA-based HNEKF are compared. In the comparison, the marker-based measurement model presented in Sect. 4.3.1 is used also in the implementation of the DA-based HNEKF, whose Taylor expansion is limited to the first and second order. Indeed, no relevant improvement is obtained with higher orders, as shown in the Sect. 3.2.1, since Kalman filters are based on a Gaussian representation of the propagated uncertainties.

Table 4.4: *Sensitivity to acquisition frequency, initial linear and angular velocity uncertainty.*

Dynamics		Sensors		Frequency
$\sigma_{r_r,0}$ (m)	$K \cdot 1$	$\sigma^s_{x,y}$ (m)	0.02	0.05 Hz to 3 Hz
$\sigma_{v_r,0}$ (m/s)	$K \cdot 0.1$	σ^s_z (m)	0.03	
$\sigma_{\zeta,0}$ ()	$K \cdot 0.002$			0.05 Hz to 3 Hz
$\sigma_{\omega_r,0}$ (rad/s)	$K \cdot 0.01$			
$K = [1, 5, 10]$				

4.4.1 Accuracy and robustness analysis

A Monte-Carlo-based sensitivity analysis, taking the furthest 100 samples among the 1000 generated around the true initial conditions, is carried out to assess the robustness of linear and nonlinear filters with various acquisition frequencies and initial uncertainty reported in Table 4.4, with $\sigma_{i,0}$ and σ^s_i being the initial standard deviation and the sensor standard deviation, respectively, of the variable i. The factor K is used to generate different levels of uncertainty starting from the nominal one.
The performance are quantified by means of the statistical indexes introduced in Eq. (3.19) and Eq. (3.20), which are computed considering only

the simulations that converge reaching a final error at steady state one order of magnitude lower than the initial error. In the comparison, the name of the filter is reported in the left subscript.
In the following the case with 3 markers is deeply analyzed because it is the most significant situation. The results and conclusions considering the case with the whole set of markers are basically the same, since the extended set just slightly improves the accuracy of the filters.
In this analysis, the first and second order DA-based HNEKF are referred to as EKFDA1 and EKFDA2, respectively, while the DA-based UKF is referred to as UKFDA2 since it exploits a second order Taylor expansion of the flow.

Translational dynamics

As already observed in the previous chapter, the translational dynamics is almost static and linear since the two spacecraft are very close on the same orbit, which is nearly circular. In Sect. 3.4.1, it has been explained that high-order filters do not provide better performance with respect to the linear one, which is already capable of following the dynamic evolution. However, differently from case of the previous chapter, here the measurement equations are nonlinear and coupled. In particular, the performance of the translational filter strictly depends on the performance of the rotational one. Indeed, the rotational states are the most demanding ones to be estimated, due to the high nonlinearities in the dynamics. At the higher acquisition frequencies, both first and second order filters provide good performance with the similar error at steady state, which is in the order of 10^{-4} m for the position and 10^{-7} m/s for the velocity. The estimation of the translational states deteriorates at lower frequency due to the coupling with the rotational states. Consequently, the rotational filter is deemed to deserve a deeper study since the performance limitations derive from it. In fact, as already stated, the nonlinearities affect the estimation process more significantly, especially in case of high uncertainties and low observability of the system, and for this reason it merits a more detailed analysis.

Rotational dynamics

From Tables 4.5-4.6, it can be noticed that filters do not show significant difference in the performance for low uncertainties and high acquisition frequency. However, the situation changes moving to high uncertainties and low frequency. Especially, it can be observed how the convergence is

Table 4.5: *3 markers: sensitivity analysis for rotational dynamics.*

Modified Rodrigues Parameters				Relative Angular Velocity (rad/s)			
Freq.	**K**			Freq.	**K**		
(Hz)	**1**	**5**	**10**	(Hz)	**1**	**5**	**10**
$EKFDA1\bar{\mu}$							
0.05	9.29e-4	2.54e-3	-	**0.05**	1.78e-5	4.15e-5	-
0.1	4.47e-4	1.05e-3	2.43e-3	**0.1**	1.17e-5	2.02e-5	2.96e-5
0.5	8.68e-5	1.08e-4	3.07e-4	**0.5**	1.30e-6	2.20e-6	7.12e-6
1	6.74e-5	7.66e-5	1.27e-4	**1**	4.36e-7	8.58e-7	2.50e-6
3	8.51e-6	1.40e-5	3.46e-5	**3**	1.30e-7	3.17e-7	9.88e-7
$EKFDA1\sigma_{\bar{\mu}}$							
0.05	1.43e-4	1.02e-3	-	**0.05**	5.60e-6	1.76e-5	-
0.1	8.46e-5	7.98e-4	1.65e-3	**0.1**	3.23e-6	2.11e-5	1.71e-5
0.5	3.22e-6	4.12e-5	3.42e-4	**0.5**	1.52e-7	1.36e-6	7.88e-6
1	3.03e-6	2.29e-5	9.79e-5	**1**	1.66e-8	5.68e-7	2.94e-6
3	4.48e-7	7.83e-6	3.60e-5	**3**	1.08e-8	2.63e-7	1.21e-6
$EKFDA2\bar{\mu}$							
0.05	9.12e-4	1.76e-3	-	**0.05**	2.05e-5	2.42e-5	-
0.1	4.55e-4	8.15e-4	1.71e-3	**0.1**	1.24e-5	1.80e-5	3.14e-5
0.5	8.80e-5	1.07e-4	2.95e-4	**0.5**	1.37e-6	2.16e-6	6.83e-6
1	6.46e-5	7.34e-5	1.24e-4	**1**	4.41e-7	8.38e-7	2.45e-6
3	7.76e-6	1.31e-5	3.36e-5	**3**	1.25e-7	3.04e-7	9.68e-7
$EKFDA2\sigma_{\bar{\mu}}$							
0.05	4.42e-5	3.48e-4	-	**0.05**	2.64e-6	8.49e-6	-
0.1	1.93e-5	5.00e-4	1.58e-3	**0.1**	9.24e-7	1.27e-5	3.33e-5
0.5	3.44e-6	3.87e-5	3.23e-4	**0.5**	1.57e-7	1.29e-6	7.48e-6
1	3.07e-6	2.24e-5	9.64e-5	**1**	2.49e-8	5.34e-7	2.89e-6
3	3.50e-7	7.58e-6	3.57e-5	**3**	6.71e-9	2.54e-7	1.20e-6
$UKFDA2\bar{\mu}$							
0.05	9.12e-4	2.19e-3	2.67e-3	**0.05**	1.89e-5	3.96e-5	4.82e-5
0.1	4.53e-4	1.06e-3	2.42e-3	**0.1**	1.20e-5	1.94e-5	3.91e-5
0.5	8.79e-5	1.08e-4	3.00e-4	**0.5**	1.37e-6	2.21e-6	6.98e-6
1	6.47e-5	7.38e-5	1.24e-4	**1**	4.42e-7	8.39e-7	2.46e-6
3	7.76e-6	1.31e-5	3.38e-5	**3**	1.25e-7	3.03e-7	9.69e-7
$UKFDA2\sigma_{\bar{\mu}}$							
0.05	9.99e-5	1.39e-3	1.32e-4	**0.05**	2.98e-6	4.46e-5	2.16e-5
0.1	7.22e-5	8.90e-4	1.77e-3	**0.1**	3.17e-6	1.55e-5	3.70e-5
0.5	3.53e-6	4.04e-5	3.29e-4	**0.5**	1.59e-7	1.35e-6	7.60e-6
1	3.07e-6	2.24e-5	9.67e-5	**1**	2.48e-8	5.46e-7	2.90e-6
3	3.50e-7	7.58e-6	3.57e-5	**3**	6.72e-9	2.54e-7	1.20e-6

Table 4.6: *3 markers: success rate for each combination of frequency and amplitude factor, for rotational dynamics.*

	EKFDA1			EKFDA2			UKF			UKFDA2		
Freq.	**K**			**K**			**K**			**K**		
(Hz)	**1**	**5**	**10**	**1**	**5**	**10**	**1**	**5**	**10**	**1**	**5**	**10**
0.05	8	5	0	8	7	0	11	8	2	11	8	2
0.1	58	30	11	63	72	27	57	41	16	57	41	16
0.5	100	100	100	100	100	100	100	100	100	100	100	100
1	100	100	100	100	100	100	100	100	100	100	100	100
3	100	100	100	100	100	100	100	100	100	100	100	100

not achieved by the EKFDA (both 1 and 2) in the case with frequency 0.05 Hz and $\mathbf{K} = 10$ and fewer samples reach convergence for similar scenarios. The UT-based filters have higher convergence rate of samples at low frequency with respect to DA-based HNEKF filters, but the EKFDA2 still shows slightly better accuracy. On the other hand, the EKFDA1 is the least accurate filter. These results confirm what was already observed in the analysis in Sect. 3.4.1. Even if the improvement gained by high order filters in terms of the mean error accuracy is not so marked, ${}_{EKFDA1}\sigma_{\bar{\mu}}$ shows higher values, namely an higher dispersion of the final error. As already observed, this means that, in case of large deviations from the true initial conditions, the first order filter performance deteriorate leading to final estimates worse than the second order filters. To visualize this result, see Fig. 4.3. Note that in Fig. 4.3 all the simulations that converge are reported to mark the concept, and not only the ones reaching a final error an order of magnitude lower than the initial one. Hence, it is clear that filters that work with the full knowledge of the first two moments perform better with respect to the filter based on linearization. Among them, EKFDA2 seems to appear the filter with the best accuracy, especially for low frequencies and high uncertainties, indeed it presents lower standard deviations.
The filters based on the UT, i.e. UKF and UKFDA2, provide the same results: their difference is not at the accuracy level but on the computational time required by the filter itself, as it will be shown later. In fact, the introduction of the DA inside the UKF has the purpose of implementing a faster filter, while the accuracy is not improved.
For completeness, Tables 4.7-4.8 reports the results considering the whole set of visible markers. As already explained, the conclusions that can be drawn are analogous to the ones of the 3-markers case.

Table 4.7: *All visible markers: success rate for each combination of frequency and amplitude factor, for rotational dynamics.*

	EKFDA1			EKFDA2			UKF			UKFDA2		
Freq.	**K**			**K**			**K**			**K**		
(Hz)	**1**	**5**	**10**	**1**	**5**	**10**	**1**	**5**	**10**	**1**	**5**	**10**
0.05	8	6	2	8	17	3	12	11	3	12	11	3
0.1	59	41	18	69	79	36	64	57	24	64	57	24
0.5	100	100	100	100	100	100	100	100	100	100	100	100
1	100	100	100	100	100	100	100	100	100	100	100	100
3	100	100	100	100	100	100	100	100	100	100	100	100

Table 4.8: *All visible markers: sensitivity analysis for rotational performance.*

Modified Rodriguez Parameters				Relative Angular Velocity (rad/s)			
Freq.	**K**			Freq.	**K**		
(Hz)	**1**	**5**	**10**	(Hz)	**1**	**5**	**10**
$EKFDA1\bar{\mu}$							
0.05	8.90e-4	1.98e-3	5.13e-3	**0.05**	1.82e-5	3.48e-5	4.31e-5
0.1	4.43e-4	1.33e-3	2.64e-3	**0.1**	9.46e-6	2.51e-5	3.24e-5
0.5	9.46e-5	1.06e-4	2.27e-4	**0.5**	1.93e-6	2.31e-6	5.37e-6
1	5.16e-5	5.39e-5	6.87e-5	**1**	3.93e-7	5.30e-7	1.11e-6
3	9.44e-6	1.06e-5	1.44e-5	**3**	1.52e-7	1.95e-7	3.55e-7
$EKFDA1\sigma_{\bar{\mu}}$							
0.05	1.49e-4	6.31e-4	3.34e-4	**0.05**	3.84e-4	1.94e-5	3.79e-5
0.1	6.96e-5	1.17e-4	2.20e-3	**0.1**	2.75e-6	2.40e-5	2.46e-5
0.5	1.81e-6	3.27e-5	2.13e-4	**0.5**	8.81e-8	1.01e-6	4.48e-6
1	1.24e-6	8.82e-6	3.27e-5	**1**	1.21e-8	2.07e-7	9.52e-7
3	1.37e-7	1.44e-6	7.30e-6	**3**	6.16e-9	6.63e-8	2.79e-7
$EKFDA2\bar{\mu}$							
0.05	9.36e-4	1.21e-3	2.82e-3	**0.05**	2.35e-5	2.51e-5	2.17e-5
0.1	4.49e-4	7.60e-4	1.23e-3	**0.1**	1.05e-5	1.64e-5	2.24e-5
0.5	9.46e-5	1.04e-4	2.13e-4	**0.5**	1.96e-6	2.25e-6	5.01e-6
1	5.07e-5	5.30e-5	6.79e-5	**1**	3.88e-7	5.24e-7	1.10e-6
3	9.17e-7	9.98e-6	1.41e-5	**3**	1.49e-7	1.91e-7	3.50e-7
$EKFDA2\sigma_{\bar{\mu}}$							
0.05	1.54e-5	4.01e-4	2.21e-3	**0.05**	6.56e-7	6.79e-6	8.79e-6
0.1	9.47e-6	6.23e-4	1.10e-3	**0.1**	4.29e-6	1.19e-5	2.38e-5
0.5	1.75e-6	3.05e-5	1.96e-4	**0.5**	8.47e-8	9.51e-7	4.17e-6
1	1.23e-6	8.67e-6	3.24e-5	**1**	1.03e-8	2.02e-7	9.41e-7
3	1.23e-7	1.38e-6	7.25e-6	**3**	5.58e-9	6.45e-8	2.77e-7
$UKFDA2\bar{\mu}$							
0.05	8.54e-4	1.77e-3	2.79e-3	**0.05**	1.91e-5	3.05e-5	2.60e-5
0.1	4.50e-4	1.02e-3	2.12e-3	**0.1**	1.04e-5	2.00e-5	3.22e-5
0.5	9.45e-5	1.06e-4	2.23e-4	**0.5**	1.95e-6	2.32e-6	5.29e-6
1	5.07e-5	5.30e-5	6.79e-5	**1**	3.88e-7	5.24e-7	1.11e-6
3	9.17e-7	9.98e-6	1.41e-5	**3**	1.49e-7	1.91e-7	3.50e-7
$UKFDA2\sigma_{\bar{\mu}}$							
0.05	8.86e-5	1.06e-3	1.75e-3	**0.05**	3.19e-6	2.63e-5	1.72e-5
0.1	6.31e-5	7.15e-4	1.79e-3	**0.1**	2.50e-6	1.52e-5	2.45e-5
0.5	1.85e-6	3.32e-5	2.04e-4	**0.5**	8.86e-8	1.04e-6	4.42e-6
1	1.23e-6	8.70e-6	3.25e-5	**1**	1.04e-8	2.03e-7	9.45e-7
3	1.23e-7	1.38e-6	7.25e-6	**3**	5.58e-9	6.45e-8	2.77e-7

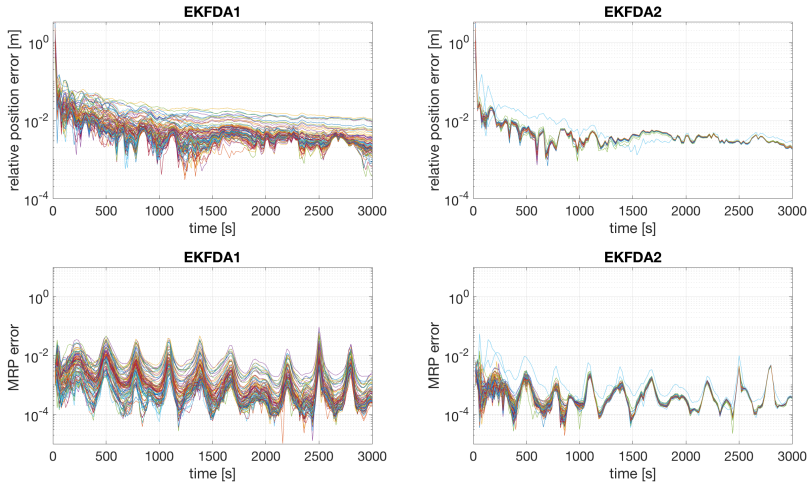

Figure 4.3: *EKFDA1 and EKFDA2 accuracy for the whole set of 100 samples in the case with frequency 0.05 Hz and* $\mathbf{K} = 1$ *for the relative position and MRP.*

4.4.2 Computational time

Table 4.9 shows the software computational time performed on a 3000 seconds simulation. The characteristic time used to describe the performance of the filters at each frequency is evaluated as a mean among all the simulations in which the error converges. The computational mean time is evaluated in the following way:

$$\Psi_f = \frac{\sum_{j=1}^{3} \frac{\sum_{i=1}^{\kappa_{f,j}} \tau_{f,j,i}}{\kappa_{f,j}}}{3}, \tag{4.27}$$

where $\Psi_f \in \mathbb{R}$ is the computational mean time associated to frequency $f = [0.05, 0.1, 0.5, 1, 3]$; j indicates the level of uncertainty used in the simulation, and thus it is related to the amplification factor K ($j = 1 \rightarrow K = 1, j = 2 \rightarrow K = 5, j = 3 \rightarrow K = 10$); $\kappa_{f,j}$ is the number of simulations in which the convergence is achieved with frequency f and amplification factor j; and $\tau_{i,j,k}$ is the computational time of the i^{th} sample in simulation (f, j). Figure 4.4 is a graphical representation of the computational time behavior of the filters at different frequencies in the case where all the visible markers are used as measurement. The computational time is the running-time on an Intel Core i7-6700K processor with a total of 4 cores @ 4.0 GHz and 16 GB of RAM.
The linear filter EKFDA1, as expected, is the fastest one. The UKFDA2

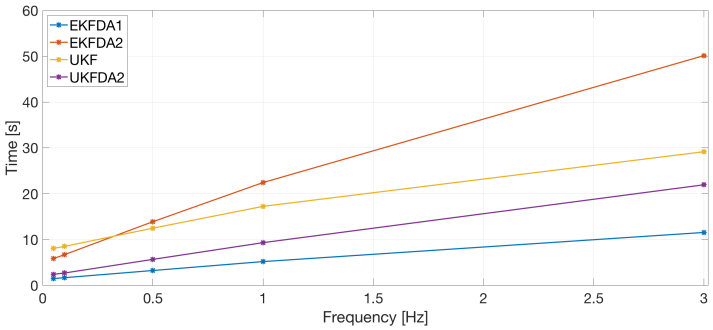

Figure 4.4: *All visible markers: mean computational time of the filters at different frequencies.*

has nearly the same trend of the UKF but it requires less time. Therefore, the improvement of including DA in the UT is evident: the two filters have the same accuracy, but the one based on DA is faster in the whole frequency range. The EKFDA2 is the filter with the most demanding computational time at high frequency, while it is faster than standard UKF at low frequency.

Table 4.9: *Computational time analysis of the filters.*

Freq. (Hz)	EKFDA1 Ψ_f (s)	EKFDA2 Ψ_f (s)	UKF Ψ_f (s)	UKFDA2 Ψ_f (s)
All Markers				
0.05	1.47	5.84	8.06	2.41
0.1	1.67	6.70	8.50	2.69
0.5	3.23	13.88	12.47	5.66
1	5.18	22.43	17.23	9.31
3	11.54	50.13	29.16	21.94
3 Markers				
0.05	1.40	5.49	7.98	2.23
0.1	1.53	6.00	8.26	2.41
0.5	2.93	10.19	11.15	4.22
1	3.37	15.25	14.29	6.43
3	6.23	30.10	20.43	13.31

Looking at Table 4.9, the overall simulation time has decreased, for each filter and for all the frequencies, in the 3 markers limitation cases. The EKFDA1 is always the fastest filter, followed by UKFDA2 with almost double computational time. The main difference between the all-markers simulation and the 3-markers one lies in the comparison between EKFDA2 and UKF. The reduced length of the measurement vector implies a faster

inversion of the measurement covariance matrix, which is the most time-demanding passage in the DA-based filter. Therefore, for the 3 marker simulation, the EKFDA2 reduces its computational time as the frequency decreases with a stronger slope compared to the UKF. As a result, EKFDA2 and UKF have almost the same computational time at 1 Hz and the UKF becomes the most demanding filter, in terms of time, at lower frequencies.

4.4.3 Acquisition Failure

Measurement failures can be critical in sequential state estimation application; indeed, the lack of proper data management could lead to an unforeseen behavior of the filters. Therefore, in this section, the filters are tested against marker position data failure.
Considering a set of 3 markers, 8 different situations can arise, depending on the number of markers not recognized. Indeed, using a binary notation where 1 identifies acquisition failure and 0 identifies the correct acquisition, the 8 combinations of possible events are 111 - 100 - 010 - 001 - 110 - 101 - 011 - 000. Given a failure probability level, $p = 20\%$, it is possible to calculate the probability of having a certain amount of failures in the set of 3 markers. Defining with α the number of markers not recognized, then the probability of having α misrecognition in a set, $\mathcal{P}_\alpha$, is evaluated according to the following equation:

$$\mathcal{P}_\alpha = [p^\alpha (1-p)^{(N-\alpha)}]\gamma \tag{4.28}$$

where N, number of elements, is in this case 3 since the set includes 3 markers, and γ is an integer number that indicates how many combinations of failures having α markers not recognized are possible.

Table 4.10: *Probability of failures in a set of 3 markers.*

α	γ	$\mathcal{P}_\alpha$
3	1	0.80%
2	3	9.60%
1	3	38.40%
0	1	51.20%

In table 4.10, it can be seen that only half of the time steps work without any failure (with probability threshold p).
Table 4.11 shows that, as expected, failures affect negatively the filters performance. Robustness to acquisition failures has been tested at low frequency, where the lack of measurement becomes more relevant. Only the results of the EKFDA2 are reported to give a comparison with respect to

Table 4.11: *Sensitivity analysis for rotational dynamics with failure.*

Modified Rodriguez Parameters				Relative Angular Velocity (rad/s)			
Freq.	**K**			Freq.	**K**		
(Hz)	**1**	**5**	**10**	(Hz)	**1**	**5**	**10**
$EKFDA2\bar{\mu}$							
0.05	9.88e-4	1.82e-3	2.54e-3	**0.05**	2.09e-5	2.17e-5	1.69e-5
0.1	4.66e-4	1.11e-3	1.42e-3	**0.1**	1.16e-5	1.99e-5	2.22e-5
0.5	9.97e-5	1.63e-4	5.71e-4	**0.5**	1.55e-6	3.72e-6	1.19e-5
$EKFDA2\sigma_{\bar{\mu}}$							
0.05	1.37e-4	7.87e-4	0	**0.05**	2.62e-6	3.85e-6	0
0.1	7.29e-5	9.21e-4	1.31e-3	**0.1**	2.76e-6	1.56e-5	1.98e-5
0.5	1.96e-5	1.46e-5	8.76e-4	**0.5**	4.93e-7	3.90e-6	1.71e-5

Table 4.12: *Success rate for each combination of frequency and amplitude factor, considering failures, for rotational dynamics.*

	EKFDA1			EKFDA2			UKF			UKFDA2		
Freq.	**K**			**K**			**K**			**K**		
(Hz)	**1**	**5**	**10**	**1**	**5**	**10**	**1**	**5**	**10**	**1**	**5**	**10**
0.05	3	3	0	6	6	1	9	2	1	10	4	1
0.1	48	24	10	63	51	20	58	31	13	58	31	13
0.5	100	100	89	100	100	94	100	100	93	100	100	93

the case without failures. It can be observed that the accuracy decreases in terms of both the mean value and standard deviation of the RMSE. However, the main difference is in the latter one. In fact, the RMSE standard deviation considerably increases, which means that, due to the stochastic nature of the failures, the convergence of one single run highly depends on when and where the failure occurs. Moreover, looking at Table 4.12 it can be noticed that the success rate of all the filters decreases further at low frequency.

The performance comparison among the filters presents the same behavior described in the simulations with no failures. However, the difference between nonlinear filters and the classical EKF is here more marked, especially in the ability of nonlinear filters to be more robust and consistent.

CHAPTER 5

Contact detection, isolation and identification for space robots

Along with the relative pose estimation of a target satellite, space robotic applications require a safe handling of the physical contact. As already explained, the space robot can be controlled to perform grasping or manipulation tasks, involving contacts, but at the same time unexpected collisions may occur due to the proximity to other objects. In both situations, the knowledge of the contact force is a valuable information to carry out the operations safely. Especially, in case of unintentional contacts, the robot must be able to detect, isolate and identify the external force in order to react properly, avoiding critical damages. To this aim, in this chapter, two observers are introduced capable of reconstructing the external contact wrench. Their performance is assessed and compared through numerical simulations. Moreover, the results of the experimental tests performed to validate the presented algorithms are shown. Finally, another approach to address the contact detection and isolation problems is discussed and compared with the previous ones. This method is based on the robot's momentum monitoring.

5.1 Nonlinear observers based on momentum

The starting point for the development of the contact force observers for orbital robots is the residual-based estimator presented in [47] for humanoids. Here, this estimator is adapted and analyzed considering a space scenario and an actuated base. The method derives from the momentum-based observer, developed for fixed-base robots [45], in which a residual vector is defined as the difference between the generalized momentum of the robot and its estimate. Under ideal condition, this residual vector turns out to be a filtered estimation of the external disturbance acting on the joints. Hereafter, the same idea is followed using the dynamics model (2.24), namely a base-joints dynamics, to obtain the estimates of $\boldsymbol{f}_{ext,b}$, $\boldsymbol{m}_{ext,b}$ and $\boldsymbol{\tau}_{ext}$.
Afterwards, the proposed observer, based on a centroid-joints dynamics, is derived and discussed. Interesting decoupling properties from the base linear velocity are highlighted, which result in improved performance when real implementation issues are considered.

5.2 Observer based on a base-joints dynamics

Considering Eq. (2.24), the dynamics of the robot can be split into base linear and rotational dynamics, i.e., the first and second rows of the equation, and joints dynamics, i.e., the third row of the equation.
Denoting by $\hat{\boldsymbol{f}}_{ext,b}, \hat{\boldsymbol{m}}_{ext,b} \in \mathbb{R}^3$ and $\hat{\boldsymbol{\tau}}_{ext} \in \mathbb{R}^n$ the residuals, they are designed as follows:

$$\hat{\boldsymbol{f}}_{ext,b} = \boldsymbol{K}_f(\underbrace{\boldsymbol{M}_t\boldsymbol{v}_b + \boldsymbol{M}_{tr}\boldsymbol{\omega}_b + \boldsymbol{M}_{tm}\dot{\boldsymbol{q}}}_{\boldsymbol{h}_b^t} + - \int_0^t (\boldsymbol{f}_b + \boldsymbol{C}_t^T\boldsymbol{v}_b + \boldsymbol{C}_{rt}^T\boldsymbol{\omega}_b + \boldsymbol{C}_{mt}^T\dot{\boldsymbol{q}} + \hat{\boldsymbol{f}}_{ext,b})ds), \tag{5.1a}$$

$$\hat{\boldsymbol{m}}_{ext,b} = \boldsymbol{K}_m(\underbrace{\boldsymbol{M}_{tr}^T\boldsymbol{v}_b + \boldsymbol{M}_r\boldsymbol{\omega}_b + \boldsymbol{M}_{rm}\dot{\boldsymbol{q}}}_{\boldsymbol{h}_b^r} + - \int_0^t (\boldsymbol{m}_b + \boldsymbol{C}_{tr}^T\boldsymbol{v}_b + \boldsymbol{C}_r^T\boldsymbol{\omega}_b + \boldsymbol{C}_{mr}^T\dot{\boldsymbol{q}} + \hat{\boldsymbol{m}}_{ext,b})ds), \tag{5.1b}$$

$$\hat{\boldsymbol{\tau}}_{ext} = \boldsymbol{K}_\tau(\underbrace{\boldsymbol{M}_{tm}^T\boldsymbol{v}_b + \boldsymbol{M}_{rm}^T\boldsymbol{\omega}_b + \boldsymbol{M}_m\dot{\boldsymbol{q}}}_{\boldsymbol{h}_j} + - \int_0^t (\boldsymbol{\tau} + \boldsymbol{C}_{tm}^T\boldsymbol{v}_b + \boldsymbol{C}_{rm}^T\boldsymbol{\omega}_b + \boldsymbol{C}_m^T\dot{\boldsymbol{q}} + \hat{\boldsymbol{\tau}}_{ext})ds), \tag{5.1c}$$

where $\boldsymbol{K}_f, \boldsymbol{K}_m \in \mathbb{R}^{3\times3}$ and $\boldsymbol{K}_\tau \in \mathbb{R}^{n\times n}$ are positive-definite diagonal matrices containing the observer gains; $\boldsymbol{h}_j \in \mathbb{R}^n$ is the joints generalized momentum.
Differentiating Eqs. (5.1a), (5.1b), and (5.1c), and exploiting the dynamics (2.24) and the property $\dot{\boldsymbol{M}} = \boldsymbol{C} + \boldsymbol{C}^T$, the resulting relations between the estimates and the true quantities are

$$\dot{\hat{\boldsymbol{f}}}_{ext,b} = \boldsymbol{K}_f(\boldsymbol{f}_{ext,b} - \hat{\boldsymbol{f}}_{ext,b}), \tag{5.2a}$$

$$\dot{\hat{\boldsymbol{m}}}_{ext,b} = \boldsymbol{K}_m(\boldsymbol{m}_{ext,b} - \hat{\boldsymbol{m}}_{ext,b}), \tag{5.2b}$$

$$\dot{\hat{\boldsymbol{\tau}}}_{ext} = \boldsymbol{K}_\tau(\boldsymbol{\tau}_{ext} - \hat{\boldsymbol{\tau}}_{ext}). \tag{5.2c}$$

From Eq. (5.2) it can be noticed that $\hat{\boldsymbol{f}}_{ext,b}$, $\hat{\boldsymbol{m}}_{ext,b}$, and $\hat{\boldsymbol{\tau}}_{ext}$ are first-order-filtered estimations of $\boldsymbol{f}_{ext,b}$, $\boldsymbol{m}_{ext,b}$, and $\boldsymbol{\tau}_{ext}$, respectively.
Increasing the observer gains reduces the time constants of the transient response of the estimates, and thus a faster estimation of $\boldsymbol{f}_{ext,b}, \boldsymbol{m}_{ext,b}$, and $\boldsymbol{\tau}_{ext}$. Ideally, if the observer gains tend to infinity, it would be achieved $\hat{\boldsymbol{f}}_{ext,b} \approx \boldsymbol{f}_{ext,b}$, $\hat{\boldsymbol{m}}_{ext,b} \approx \boldsymbol{m}_{ext,b}$ and $\hat{\boldsymbol{\tau}}_{ext} \approx \boldsymbol{\tau}_{ext}$, respectively. However, in practice, noise and uncertainties induce an upper bound on the values that the observer gains can take. Moreover, the computation of all the residuals, i.e., $\hat{\boldsymbol{f}}_{ext,b}$, $\hat{\boldsymbol{m}}_{ext,b}$, and $\hat{\boldsymbol{\tau}}_{ext}$, requires the knowledge of the base linear velocity $\boldsymbol{v}_b$. A fast and accurate estimation of the linear velocity is particularly difficult in practical applications and the observer scheme (5.1) would require very low gains resulting in limited response bandwidth. This limitation motivates the derivation of the proposed observer presented hereafter, which turns out to be more practical and better-performing.

5.3 Observer based on a centroid-joints dynamics

In this section, the robot dynamics is transformed using a new set of generalized velocities: the linear velocity of the center of mass (CM) of the whole system, the angular momentum around $\mathcal{C}$ expressed in $\mathcal{C}$ and the joints velocities. Afterwards, the transformed dynamics is used to formulate the new observer scheme.
The total momentum around $\mathcal{C}$ expressed in $\mathcal{C}$, denoted by $\boldsymbol{h}_c \in \mathbb{R}^6$, can be

found as $\boldsymbol{h}_c = \boldsymbol{A}_{cb}^{-T}\boldsymbol{h}_b$ [43][1], resulting in

$$\boldsymbol{h}_c = \begin{bmatrix} \boldsymbol{h}_c^t \\ \boldsymbol{h}_c^r \end{bmatrix} = \begin{bmatrix} m\boldsymbol{E} & -m[\boldsymbol{p}_{bc}]^\times & m\bar{\boldsymbol{J}}_v \\ \boldsymbol{0} & \boldsymbol{I}_c & \boldsymbol{I}_c\bar{\boldsymbol{J}}_\omega \end{bmatrix} \begin{bmatrix} \boldsymbol{v}_b \\ \boldsymbol{\omega}_b \\ \dot{\boldsymbol{q}} \end{bmatrix}, \tag{5.3}$$

where $\boldsymbol{h}_c^t \in \mathbb{R}^3$ is the translational momentum and $\boldsymbol{h}_c^r \in \mathbb{R}^3$ is the rotational momentum around $\mathcal{C}$, both expressed in $\mathcal{C}$, $m \in \mathbb{R}$ and $\boldsymbol{I}_c \in \mathbb{R}^{3\times3}$ are the mass and the rotational inertia around $\mathcal{C}$ of the whole body, and $\bar{\boldsymbol{J}}_v, \bar{\boldsymbol{J}}_\omega \in \mathbb{R}^{3\times n}$ are computed as follows

$$\bar{\boldsymbol{J}}_v = \frac{1}{m}\sum_{i=1}^{n} m_i \boldsymbol{R}_{ib}^T \boldsymbol{J}_{vi}, \tag{5.4}$$

$$\bar{\boldsymbol{J}}_\omega = \boldsymbol{I}_c^{-1}\sum_{i=1}^{n} \boldsymbol{R}_{ib}^T \boldsymbol{I}_i \boldsymbol{J}_{\omega i} + m_i[\boldsymbol{p}_{bi}]^\times(\boldsymbol{J}_{vi} - \bar{\boldsymbol{J}}_v), \tag{5.5}$$

with $m_i \in \mathbb{R}$ and $\boldsymbol{I}_i \in \mathbb{R}^{3\times3}$ being the mass and rotational inertia of body i, computed around its CM, and $\boldsymbol{J}_{vi}, \boldsymbol{J}_{\omega i} \in \mathbb{R}^{3\times n}$ being the Jacobians mapping $\dot{\boldsymbol{q}}$ in the linear and angular velocity of body i, respectively. The Jacobians $\bar{\boldsymbol{J}}_v$ and $\bar{\boldsymbol{J}}_\omega$ can be also computed based on the inertia model in (2.24) as:

$$\bar{\boldsymbol{J}}_v = \frac{1}{m}\boldsymbol{M}_{tm}, \tag{5.6}$$

$$\bar{\boldsymbol{J}}_\omega = \left(\boldsymbol{M}_r - \frac{1}{m}\boldsymbol{M}_{tr}^T\boldsymbol{M}_{tr}\right)^{-1}\left(\boldsymbol{M}_{rm} - \frac{1}{m}\boldsymbol{M}_{tr}^T\boldsymbol{M}_{tm}\right). \tag{5.7}$$

Introducing the linear velocity of the CM of the whole system, $\boldsymbol{v}_c = \frac{1}{m}\boldsymbol{h}_c^t \in \mathbb{R}^3$, and exploiting Eq. (5.3), a transformation matrix $\boldsymbol{\Gamma} \in \mathbb{R}^{(6+n)\times(6+n)}$ can be defined as

$$\begin{bmatrix} \boldsymbol{v}_c \\ \boldsymbol{h}_c^r \\ \dot{\boldsymbol{q}} \end{bmatrix} = \underbrace{\begin{bmatrix} \boldsymbol{E} & -[\boldsymbol{p}_{bc}]^\times & \bar{\boldsymbol{J}}_v \\ \boldsymbol{0} & \boldsymbol{I}_c & \boldsymbol{I}_c\bar{\boldsymbol{J}}_\omega \\ \boldsymbol{0} & \boldsymbol{0} & \boldsymbol{E} \end{bmatrix}}_{\boldsymbol{\Gamma}} \begin{bmatrix} \boldsymbol{v}_b \\ \boldsymbol{\omega}_b \\ \dot{\boldsymbol{q}} \end{bmatrix}. \tag{5.8}$$

[1]The equations used herein are slightly different from the ones presented in [43]: in [43] the frame $\mathcal{C}$ is nonrotating, whereas here $\mathcal{C}$ is rotating, parallel to $\mathcal{B}$.

Consequently, the generalized forces transform as

$$\begin{bmatrix} \boldsymbol{f}_b \\ \boldsymbol{m}_b \\ \boldsymbol{\tau} \end{bmatrix} = \boldsymbol{\Gamma}^T \begin{bmatrix} \boldsymbol{f}_c \\ \boldsymbol{a}_c \\ \bar{\boldsymbol{\tau}} \end{bmatrix}, \tag{5.9}$$

$$\begin{bmatrix} \boldsymbol{f}_{ext,b} \\ \boldsymbol{m}_{ext,b} \\ \boldsymbol{\tau}_{ext} \end{bmatrix} = \boldsymbol{\Gamma}^T \begin{bmatrix} \boldsymbol{f}_{ext,c} \\ \boldsymbol{a}_{ext,c} \\ \bar{\boldsymbol{\tau}}_{ext} \end{bmatrix}, \tag{5.10}$$

where $\boldsymbol{f}_c \in \mathbb{R}^3$, $\boldsymbol{a}_c \in \mathbb{R}^3$, and $\bar{\boldsymbol{\tau}} \in \mathbb{R}^n$ are new control inputs; $\boldsymbol{f}_{ext,c} \in \mathbb{R}^3$, $\boldsymbol{a}_{ext,c} \in \mathbb{R}^3$, and $\bar{\boldsymbol{\tau}}_{ext} \in \mathbb{R}^n$ are the projections of the external wrench $\boldsymbol{\mathcal{F}}_{ext}$ into the new variables space.
Then, the dynamics in the new states is derived pre-multiplying (2.24) by $\boldsymbol{\Gamma}^{-T}$ and substituting $\boldsymbol{v}_b$, $\boldsymbol{\omega}_b$, $\dot{\boldsymbol{q}}$ and their derivatives isolated from Eq. (5.8) in (2.24). The resulting system is

$$\begin{aligned} &\begin{bmatrix} m\boldsymbol{E} & \boldsymbol{0} & \boldsymbol{0} \\ \boldsymbol{0} & \boldsymbol{I}_c^{-1} & \boldsymbol{0} \\ \boldsymbol{0} & \boldsymbol{0} & \boldsymbol{M}_m^* \end{bmatrix} \begin{bmatrix} \dot{\boldsymbol{v}}_c \\ \dot{\boldsymbol{h}}_c^r \\ \ddot{\boldsymbol{q}} \end{bmatrix} + \\ &+ \begin{bmatrix} \boldsymbol{C}_c & \boldsymbol{C}_{cr} & \boldsymbol{C}_{cm} \\ -\boldsymbol{C}_{cr}^T & \boldsymbol{C}_r^* & \boldsymbol{C}_{rm}^* \\ -\boldsymbol{C}_{cm}^T & -\boldsymbol{C}_{rm}^{*T} & \boldsymbol{C}_m^* \end{bmatrix} \begin{bmatrix} \boldsymbol{v}_c \\ \boldsymbol{h}_c^r \\ \dot{\boldsymbol{q}} \end{bmatrix} = \begin{bmatrix} \boldsymbol{f}_c \\ \boldsymbol{a}_c \\ \bar{\boldsymbol{\tau}} \end{bmatrix} + \begin{bmatrix} \boldsymbol{f}_{ext,c} \\ \boldsymbol{a}_{ext,c} \\ \bar{\boldsymbol{\tau}}_{ext} \end{bmatrix}. \end{aligned} \tag{5.11}$$

where

$$\boldsymbol{M}_m^* = \boldsymbol{M}_m - \begin{bmatrix} \boldsymbol{M}_{tm}^T & \boldsymbol{M}_{rm}^T \end{bmatrix} \begin{bmatrix} \boldsymbol{M}_t & \boldsymbol{M}_{tr} \\ \boldsymbol{M}_{tr}^T & \boldsymbol{M}_r \end{bmatrix}^{-1} \begin{bmatrix} \boldsymbol{M}_{tm} \\ \boldsymbol{M}_{rm} \end{bmatrix} \in \mathbb{R}^{n \times n} \tag{5.12}$$

is the reduced inertia of the manipulator.
Expressing the dynamics in these new variables enables to obtain a system of inertially decoupled dynamic equations. Moreover, it can be demonstrated (see Appendix) that the following relations hold:

$$\boldsymbol{C}_c \boldsymbol{v}_c + \boldsymbol{C}_{cr} \boldsymbol{h}_c^r + \boldsymbol{C}_{cm} \dot{\boldsymbol{q}} = m \left[\boldsymbol{\omega}_b\right]^\times \boldsymbol{v}_c, \tag{5.13a}$$

$$-\boldsymbol{C}_{cr}^T \boldsymbol{v}_c + \boldsymbol{C}_r^* \boldsymbol{h}_c^r + \boldsymbol{C}_{rm}^* \dot{\boldsymbol{q}} = \boldsymbol{I}_c^{-1} \left[\boldsymbol{\omega}_b\right]^\times \boldsymbol{h}_c^r, \tag{5.13b}$$

$$\begin{aligned} -\boldsymbol{C}_{cm}^T \boldsymbol{v}_c - \boldsymbol{C}_{rm}^{*T} \boldsymbol{h}_c^r + \boldsymbol{C}_m^* \dot{\boldsymbol{q}} = (\dot{\boldsymbol{M}}_m^* - \frac{1}{2} \boldsymbol{M}_{m/q}^*) \dot{\boldsymbol{q}} + \\ + (\dot{\bar{\boldsymbol{J}}}_\omega^T - \bar{\boldsymbol{J}}_\omega^T \left[\boldsymbol{\omega}_b\right]^\times + \frac{1}{2} \boldsymbol{I}_{c/q}^{-T} - \bar{\boldsymbol{J}}_{\omega/q}^T) \boldsymbol{h}_c^r, \end{aligned} \tag{5.13c}$$

where

$$\boldsymbol{M}^*_{m/q} = \begin{bmatrix} \dot{\boldsymbol{q}}^T \frac{\partial \boldsymbol{M}^*_m}{\partial q_1} \\ \vdots \\ \dot{\boldsymbol{q}}^T \frac{\partial \boldsymbol{M}^*_m}{\partial q_n} \end{bmatrix} \in \mathbb{R}^{n \times n}, \tag{5.14}$$

$$\boldsymbol{I}^{-T}_{c/q} = \begin{bmatrix} \boldsymbol{h}^{rT}_c \frac{\partial \boldsymbol{I}^{-T}_c}{\partial q_1} \\ \vdots \\ \boldsymbol{h}^{rT}_c \frac{\partial \boldsymbol{I}^{-T}_c}{\partial q_n} \end{bmatrix} \in \mathbb{R}^{n \times 3}, \tag{5.15}$$

$$\bar{\boldsymbol{J}}^T_{\omega/q} = \begin{bmatrix} \dot{\boldsymbol{q}}^T \frac{\partial \bar{\boldsymbol{J}}^T_\omega}{\partial q_1} \\ \vdots \\ \dot{\boldsymbol{q}}^T \frac{\partial \bar{\boldsymbol{J}}^T_\omega}{\partial q_n} \end{bmatrix} \in \mathbb{R}^{n \times 3}. \tag{5.16}$$

The dynamic equations can be rewritten as

$$m\dot{\boldsymbol{v}}_c + m\left[\boldsymbol{\omega}_b\right]^\times \boldsymbol{v}_c = \boldsymbol{f}_c + \boldsymbol{f}_{ext,c}, \tag{5.17a}$$

$$\dot{\boldsymbol{h}}^r_c + \left[\boldsymbol{\omega}_b\right]^\times \boldsymbol{h}^r_c = \boldsymbol{m}_c + \boldsymbol{m}_{ext,c}, \tag{5.17b}$$

$$\begin{aligned} \boldsymbol{M}^*_m \ddot{\boldsymbol{q}} + (\dot{\boldsymbol{M}}^*_m - \frac{1}{2}\boldsymbol{M}^*_{m/q})\dot{\boldsymbol{q}} + (\dot{\bar{\boldsymbol{J}}}^T_\omega - \bar{\boldsymbol{J}}^T_\omega \left[\boldsymbol{\omega}_b\right]^\times + \\ + \frac{1}{2}\boldsymbol{I}^{-T}_{c/q} - \bar{\boldsymbol{J}}^T_{\omega/q})\boldsymbol{h}^r_c = \bar{\boldsymbol{\tau}} + \bar{\boldsymbol{\tau}}_{ext}, \end{aligned} \tag{5.17c}$$

where it is denoted $\boldsymbol{m}_c = \boldsymbol{I}_c \boldsymbol{a}_c \in \mathbb{R}^3$ and $\boldsymbol{m}_{ext,c} = \boldsymbol{I}_c \boldsymbol{a}_{ext,c} \in \mathbb{R}^3$.
First, note that Eqs. (5.17b) and (5.17c) do not depend on the base linear velocity anymore. On the other hand, Eq. (5.17a) depends on the base linear velocity trough $\boldsymbol{v}_c$. Second, note that $\boldsymbol{M}^*_m$, $\bar{\boldsymbol{J}}_\omega$, $\boldsymbol{M}^*_{m/q}$, $\boldsymbol{I}_{c/q}$, and $\bar{\boldsymbol{J}}_{\omega/q}$ depend only on $\boldsymbol{q}$, and $\dot{\bar{\boldsymbol{J}}}_\omega$ depends on $\boldsymbol{q}$ and $\dot{\boldsymbol{q}}$.
Starting from (5.17), the residuals $\hat{\boldsymbol{f}}_{ext,c}, \hat{\boldsymbol{m}}_{ext,c} \in \mathbb{R}^3$ and $\hat{\bar{\boldsymbol{\tau}}}_{ext} \in \mathbb{R}^n$, are

designed as

$$\hat{\boldsymbol{f}}_{ext,c} = \boldsymbol{K}_f(\underbrace{m\boldsymbol{v}_c}_{\boldsymbol{h}_c^t} - \int_0^t (\boldsymbol{f}_c - m\left[\boldsymbol{\omega}_b\right]^\times \boldsymbol{v}_c + \hat{\boldsymbol{f}}_{ext,c})ds), \tag{5.18a}$$

$$\hat{\boldsymbol{m}}_{ext,c} = \boldsymbol{K}_m(\boldsymbol{h}_c^r - \int_0^t (\boldsymbol{m}_c - \left[\boldsymbol{\omega}_b\right]^\times \boldsymbol{h}_c^r + \hat{\boldsymbol{m}}_{ext,c})ds), \tag{5.18b}$$

$$\begin{aligned}\hat{\bar{\boldsymbol{\tau}}}_{ext} = \boldsymbol{K}_\tau(\overbrace{\boldsymbol{M}_m^*\dot{\boldsymbol{q}}}^{\boldsymbol{h}_j^*} - \int_0^t (\bar{\boldsymbol{\tau}} + \frac{1}{2}\boldsymbol{M}_{m/q}^*\dot{\boldsymbol{q}} - (\dot{\bar{\boldsymbol{J}}}_\omega^T + \\ - \bar{\boldsymbol{J}}_\omega^T\left[\boldsymbol{\omega}_b\right]^\times + \frac{1}{2}\boldsymbol{I}_{c/q}^{-T} - \bar{\boldsymbol{J}}_{\omega/q}^T)\boldsymbol{h}_c^r + \hat{\bar{\boldsymbol{\tau}}}_{ext})ds),\end{aligned} \tag{5.18c}$$

where $\boldsymbol{h}_j^* \in \mathbb{R}^n$ is the new joint generalized momentum in the centroid-joints dynamics. Differentiating Eqs. (5.18a), (5.18b), and (5.18c), and using the dynamics (5.17), the resulting relations between the estimates and the true quantities are

$$\dot{\hat{\boldsymbol{f}}}_{ext,c} = \boldsymbol{K}_f(\boldsymbol{f}_{ext,c} - \hat{\boldsymbol{f}}_{ext,c}), \tag{5.19a}$$

$$\dot{\hat{\boldsymbol{m}}}_{ext,c} = \boldsymbol{K}_m(\boldsymbol{m}_{ext,c} - \hat{\boldsymbol{m}}_{ext,c}), \tag{5.19b}$$

$$\dot{\hat{\bar{\boldsymbol{\tau}}}}_{ext} = \boldsymbol{K}_\tau(\bar{\boldsymbol{\tau}}_{ext} - \hat{\bar{\boldsymbol{\tau}}}_{ext}), \tag{5.19c}$$

meaning that $\hat{\boldsymbol{f}}_{ext,c}$, $\hat{\boldsymbol{m}}_{ext,c}$, and $\hat{\bar{\boldsymbol{\tau}}}_{ext}$ are first-order-filtered estimations of $\boldsymbol{f}_{ext,c}$, $\boldsymbol{m}_{ext,c}$, and $\bar{\boldsymbol{\tau}}_{ext}$, respectively. The observations about the gains tuning made in Sect. 5.2 are also valid for the proposed observer.
Note that the residuals $\hat{\boldsymbol{m}}_{ext,c}$ and $\hat{\bar{\boldsymbol{\tau}}}_{ext}$ in (5.18b) and (5.18c) are computed without using the linear velocity. Indeed, $\boldsymbol{v}_b$ does not appear in (5.18b) and (5.18c), and the matrices therein are only function of $\boldsymbol{q}$ and $\dot{\boldsymbol{q}}$, as remarked previously. This property has an important implication from the practical point of view. Considering the on-orbit scenarios, the linear velocity is not directly measured and its accurate estimation or reconstruction is difficult. Thanks to the decoupled structure of (5.17b) and (5.17c), the residuals $\hat{\boldsymbol{m}}_{ext,c}$ and $\hat{\bar{\boldsymbol{\tau}}}_{ext}$ can be computed just relying on gyroscopes, encoders and torque sensors, which typically feature good acquisition frequency and relatively low noise. Fast and accurate knowledge of the base attitude, position

and velocity, which is often unpractical, is totally avoided. Then, the residuals $\hat{\boldsymbol{m}}_{ext,c}$ and $\hat{\bar{\boldsymbol{\tau}}}_{ext}$ can be exploited to isolate the contact point and to reconstruct the external wrench $\boldsymbol{\mathcal{F}}_{ext}$, as it will be shown in the following.

5.4 Reconstruction of the external wrench

Assuming to know the contact point along the space robot, the relation between the contact generalized forces $\boldsymbol{f}_{ext,b}$, $\boldsymbol{m}_{ext,b}$, and $\boldsymbol{\tau}_{ext}$ in (2.24) and the external wrench $\boldsymbol{\mathcal{F}}_{ext}$ can be expressed as in Eq. (2.25). Using the inverse of Eq. (5.10) and recalling that $\boldsymbol{m}_{ext,c} = \boldsymbol{I}_c \boldsymbol{a}_{ext,c}$, the relation between $\boldsymbol{f}_{ext,c}$, $\boldsymbol{m}_{ext,c}$, and $\bar{\boldsymbol{\tau}}_{ext}$ and $\boldsymbol{\mathcal{F}}_{ext}$ is given by:

$$\begin{bmatrix} \boldsymbol{f}_{ext,c} \\ \boldsymbol{m}_{ext,c} \\ \bar{\boldsymbol{\tau}}_{ext} \end{bmatrix} = \begin{bmatrix} \boldsymbol{A}_{pc}^{T} \\ \boldsymbol{J}_{p}^{*T} \end{bmatrix} \boldsymbol{\mathcal{F}}_{ext}, \tag{5.20}$$

where

$$\boldsymbol{J}_{p}^{*} = \begin{bmatrix} \boldsymbol{J}_{vp}^{*} \\ \boldsymbol{J}_{\omega p}^{*} \end{bmatrix} = \begin{bmatrix} -\boldsymbol{R}_{pb}\bar{\boldsymbol{J}}_{v} + \boldsymbol{R}_{pb}[\boldsymbol{p}_{cp}]^{\wedge}\bar{\boldsymbol{J}}_{\omega} + \boldsymbol{J}_{vp} \\ -\boldsymbol{R}_{pb}\bar{\boldsymbol{J}}_{\omega} + \boldsymbol{J}_{\omega p} \end{bmatrix} \in \mathbb{R}^{6\times n}. \tag{5.21}$$

Then, an estimate $\hat{\boldsymbol{\mathcal{F}}}_{ext}$ of the external wrench at the end-effector can be computed as

$$\hat{\boldsymbol{\mathcal{F}}}_{ext} = \left(\begin{bmatrix} \boldsymbol{A}_{pc}^{T} \\ \boldsymbol{J}_{p}^{*T} \end{bmatrix} \right)^{\#} \begin{bmatrix} \hat{\boldsymbol{f}}_{ext,c} \\ \hat{\boldsymbol{m}}_{ext,c} \\ \hat{\bar{\boldsymbol{\tau}}}_{ext} \end{bmatrix}, \tag{5.22}$$

where the operator $(\cdot)^{\#}$ stands for the Moore-Penrose pseudo inverse of the argument.

Considering $\begin{bmatrix} \boldsymbol{A}_{pc}^{T} \\ \boldsymbol{J}_{p}^{*T} \end{bmatrix}$ has maximum rank, one has the freedom to eliminate redundant rows. In particular, the estimate of the external wrench can be obtained using only $\hat{\boldsymbol{m}}_{ext,c}$ and $\hat{\bar{\boldsymbol{\tau}}}_{ext}$, and thus getting rid of the base linear velocity. Selecting the last two rows of Eq. (5.20) and taking the pseudo inverse, the following relation can be written

$$\hat{\boldsymbol{\mathcal{F}}}_{ext} = \left(\tilde{\boldsymbol{J}}_{p}^{*T} \right)^{\#} \begin{bmatrix} \hat{\boldsymbol{m}}_{ext,c} \\ \hat{\bar{\boldsymbol{\tau}}}_{ext} \end{bmatrix}, \tag{5.23}$$

with

$$\tilde{\boldsymbol{J}}_p^* = \begin{bmatrix} -\boldsymbol{R}_{pb}\,[\boldsymbol{p}_{cp}]^\times & \boldsymbol{J}_{vp}^* \\ \boldsymbol{R}_{pb} & \boldsymbol{J}_{\omega p}^* \end{bmatrix} \in \mathbb{R}^{6\times(n+3)}. \tag{5.24}$$

Clearly, the rank of $\tilde{\boldsymbol{J}}_p^*$ should be maximum to reconstruct $\hat{\boldsymbol{\mathcal{F}}}_{ext}$ correctly. Notice that by using Eq. (5.23), it is possible to estimate the external wrench acting at a generic point along the robot without using any unpractical measurements, such as the base linear velocity or the joint accelerations. In the development of the reconstruction strategy, the contact point has been assumed to be known. In case of a planned contact at the end-effector, this is true and, through the kinematics, it is straightforward to compute $\boldsymbol{p}_{ce}$ and the Jacobians $\boldsymbol{J}_{ve},\ \boldsymbol{J}_{\omega e}$ (the generic point p coincides with the end-effector) required in Eq. (5.22) and in Eq. (5.23). Conversely, when dealing with an unexpected collision, the contact point is unknown and it is necessary to isolate it before being able to reconstruct the external wrench. In the following section, a solution to this problem is proposed.

5.5 Contact point isolation

Solving the isolation problem means to locate where the contact occurred. In the following, first, a procedure to identify the contact point using all the residual vectors is presented. This procedure can be applied considering both the observer (5.1) and (5.18). Then, a different approach is proposed that relies only on $\hat{\boldsymbol{m}}_{ext,c}$ and $\hat{\tilde{\boldsymbol{\tau}}}$, avoiding the need of the base linear velocity knowledge. In the development of both strategies, it is assumed that the point of application of the external disturbance does not change during the contact and the wrench only consists in a linear force and no torque, namely $\boldsymbol{\mathcal{F}}_{ext} = [\boldsymbol{f}_{ext}^T\ \boldsymbol{0}^T]^T$. Note that these are reasonable assumptions for unexpected collisions.

5.5.1 Isolation using all the residual vectors

Considering all the residual vectors available, the contact point can be identified easily. Indeed, knowing that

$$\boldsymbol{m}_{ext,c} = [\boldsymbol{p}_{cp}]^\times \boldsymbol{f}_{ext,c}, \tag{5.25}$$

it is possible to write

$$\hat{\boldsymbol{m}}_{ext,c} = [\boldsymbol{p}_{cp}]^\times \hat{\boldsymbol{f}}_{ext,c}, \tag{5.26}$$

which means that the contact point can be found on the line

$$\boldsymbol{s}_{cp} = (-[\hat{\boldsymbol{f}}_{ext,c}]^\times)^{\#}\hat{\boldsymbol{m}}_{ext,c} + d\frac{\hat{\boldsymbol{f}}_{ext,c}}{||\hat{\boldsymbol{f}}_{ext,c}||} \in \mathbb{R}^3, \tag{5.27}$$

with d being a varying scalar.
At this point, the contact point can be identified as the intersection between $\boldsymbol{s}_{cp}$ and the space robot, whose CAD representation is known or can be simplified by primitive shapes. In order to discriminate the exact point among multiple possibilities, the estimation of the external torques can be exploited. Indeed, the exact point would be the one that minimizes $||\boldsymbol{J}_p^{*T}\hat{\boldsymbol{\mathcal{F}}}_{ext} - \hat{\hat{\boldsymbol{\tau}}}_{ext}||$. Note that the same procedure can be applied using the residuals in (5.1).
It can be observed that this method is very straightforward. However, as already pointed out, it would be more convenient, from practical point of view, to be able to isolate the contact point without relying on the base linear velocity knowledge. For this reason in the following section a different approach is proposed.

5.5.2 Isolation using only $\hat{m}_{ext,c}$ and $\hat{\hat{\tau}}_{ext}$

Assuming that the link i, on which the contact occurred, is known, the external wrench $\boldsymbol{\mathcal{F}}_{ext}$ can be transformed with respect to a frame attached on a known position to link i using the Adjoint matrix, as

$$\boldsymbol{\mathcal{F}}_i = \begin{bmatrix} \boldsymbol{f}_i \\ \boldsymbol{m}_i \end{bmatrix} = \boldsymbol{A}_{pi}^T \boldsymbol{\mathcal{F}}_{ext} = \begin{bmatrix} \boldsymbol{E} & \boldsymbol{0} \\ [\boldsymbol{p}_{ip}]^\times & \boldsymbol{E} \end{bmatrix} \begin{bmatrix} \boldsymbol{f}_{ext} \\ \boldsymbol{0} \end{bmatrix}, \tag{5.28}$$

where $\boldsymbol{p}_{ip}$ is constant.
The effect of the contact wrench at frame i can be estimated using the recostruction strategy preaviously explained as

$$\hat{\boldsymbol{\mathcal{F}}}_i = \begin{bmatrix} \hat{\boldsymbol{f}}_i \\ \hat{\boldsymbol{m}}_i \end{bmatrix} = \left(\begin{bmatrix} [\boldsymbol{p}_{ci}]^\times \boldsymbol{R}_{ib}^T & \boldsymbol{R}_{ib}^T \\ \boldsymbol{J}_{vi}^{*T} & \boldsymbol{J}_{\omega i}^{*T} \end{bmatrix} \right)^{\#} \begin{bmatrix} \hat{\boldsymbol{m}}_{ext,c} \\ \hat{\hat{\boldsymbol{\tau}}}_{ext} \end{bmatrix}, \tag{5.29}$$

where $\boldsymbol{J}_{vi}^*$, $\boldsymbol{J}_{\omega i}^*$ can be computed substituting in Eq. (5.21) $\boldsymbol{R}_{pb}$ with $\boldsymbol{R}_{ib}$, $\boldsymbol{p}_{cp}$ with $\boldsymbol{p}_{ci}$, and $\boldsymbol{J}_{vp}$, $\boldsymbol{J}_{\omega p}$ with the Jacobians mapping $\dot{\boldsymbol{q}}$ into the linear and angular velocity of frame i. At this point, manipulating Eq. (5.28), the following relation can be written

$$\hat{\boldsymbol{m}}_i = [\boldsymbol{p}_{ip}]^\times \hat{\boldsymbol{f}}_i, \tag{5.30}$$

from which the line of action of $\boldsymbol{f}_{ext}$ can be computed as

$$\boldsymbol{s}_{ip} = (-[\hat{\boldsymbol{f}}_i]^\times)^{\#} \hat{\boldsymbol{m}}_i + d_i \frac{\hat{\boldsymbol{f}}_i}{||\hat{\boldsymbol{f}}_i||} \in \mathbb{R}^3. \tag{5.31}$$

with d_i being a varying scalar. Assuming the knowledge of the geometry of the link i, the contact point can be found as the intersection bewteen the

link and the line $\boldsymbol{s}_{ip}$.
Unfortunately, the contact link is usually not known in advance. However, it is possible to overcome this issue. Indeed, the scheme just explained can be applied to each link, assuming that is the contact link. At the end, two possible results can be obtained:

- no intersections are found between the line of action and the link;
- a candidate contact point is found.

Among all the candidate points, the real contact point is the one minimizing

$$\delta_{ip} = \left\| \tilde{\boldsymbol{J}}_{p,i}^{*T} \begin{bmatrix} \hat{\boldsymbol{f}}_{ext} \\ \boldsymbol{0} \end{bmatrix} - \begin{bmatrix} \hat{\boldsymbol{m}}_{ext,c} \\ \hat{\tilde{\boldsymbol{\tau}}}_{ext} \end{bmatrix} \right\|, \tag{5.32}$$

where $\tilde{\boldsymbol{J}}_{p,i}^{*} \in \mathbb{R}^{6\times(n+3)}$ is the Jacobian at the candidate point on link i. Fig. 5.1 reports the isolation method schematically.
To conclude, the residuals $\hat{\boldsymbol{m}}_{ext,c}$ and $\hat{\tilde{\boldsymbol{\tau}}}_{ext}$ allow not only to detect and estimate a contact force, but also to isolate it without the need of the knowledge of the base linear velocity.

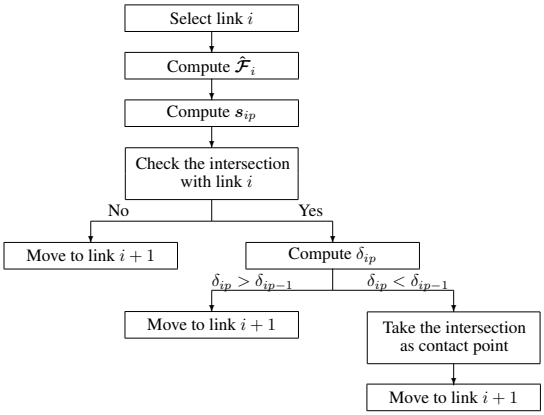

Figure 5.1: *Scheme of the proposed isolation method.*

5.6 Simulation example

In this section, the two observers are compared through numerical simulations including realistic noise models for the measurements and the reconstruction of the base linear velocity through a kinematics-based Kalman filter. The superior performance and the advantages of the proposed method based on the centroid-joints dynamics are shown.

5.6.1 Simulation scenario

A 7DoF manipulator mounted on a 6DoF floating base is considered. The kinematics and dynamics parameters are reported in Tab. 5.3.
The base is controlled to keep the initial attitude through a PD controller, whereas it is free to translate, i.e., $\boldsymbol{f}_b = \mathbf{0}$. The manipulator joints are controlled to follow a reference. Especially, joint 1 and joint 4 are commanded to follow a trapezoidal velocity profile, while the other joints are commanded to keep the initial position, i.e., $\boldsymbol{q}_0 = [-3\ 30\ 0\ 130\ 0\ -60\ 0]^T$ deg. A simple PD controller is implemented for each joint. Note that the performance of both observers does not depend on the control strategy adopted.
A constant external wrench is applied at the end-effector between $t = 2.5$ s and $t = 3.5$ s. The wrench consists of only a linear force, with value $\boldsymbol{f}_{ext} = [-10\ 5\ 8]^T$ N, and no torque.

Table 5.1: *Kinematics and dynamics parameters.*

	l [m]	m [kg]	I_x [kgm^2]	I_y [kgm^2]	I_z [kgm^2]
Base	1.2	375	280	165	250
Link 1	0.17	5.1	0.03	0.03	0.03
Link 2	1.3	18.8	1.65	1.65	0.64
Link 3	0.17	8.9	0.15	0.15	0.03
Link 4	1.3	12.0	0.25	0.25	0.03
Link 5	0.17	11.7	0.26	0.26	0.03
Link 6	0.1	5.5	0.02	0.02	0.03
Link 7	0	4.7	0.01	0.01	0.02

5.6.2 Measurement model and velocity reconstruction

The angular velocity, the joint angles and the joint torques can be directly measured using a gyro, encoders and joints torque sensors, respectively. On the other hand, the linear velocity, required for the wrench reconstruction only by the observer (5.1), and the joint velocities, required by both observers, are not directly measured but need to be reconstructed, either using a discrete derivative or by data fusion. Herein only the problem of the estimation of the linear velocity is addressed, while a simplified noise performance model is used for the joint velocities.
In order to compare the observers with similar noise conditions, the measurements of the angular velocity, joint angles and joint velocities are assumed to be affected by a white Gaussian noise with zero mean, while an uniform noise is considered for the torque sensors. For the angular velocity a bias is also introduced leading to the following model [70]:

$$\begin{aligned} \boldsymbol{\omega}_b^m &= \boldsymbol{\omega}_b + \boldsymbol{b}_\omega + \boldsymbol{\eta}_\omega, \\ \dot{\boldsymbol{b}}_\omega &= \boldsymbol{\eta}_{b\omega}, \end{aligned} \tag{5.33}$$

where $\boldsymbol{\omega}_b^m \in \mathbb{R}^3$ is the measured angular velocity of the base; the term $\boldsymbol{b}_\omega \in \mathbb{R}^3$ is the bias, considered to be a "Brownian" motion process; the terms $\boldsymbol{\eta}_\omega, \boldsymbol{\eta}_{b\omega} \in \mathbb{R}^3$ are white Gaussian noise with zero mean.
The linear velocity is reconstructed through a kinematics-based Kalman filter using a gyro and an accelerometer in the prediction step, and camera measurements for the update step. These sensors are placed on the spacecraft. The camera measures the base position with respect to the inertial frame $\mathcal{T}$ (see Fig. 2.3), that can be imagined to be located on a target object [71].
The position of the target with respect to the base $\boldsymbol{p}_{bt} \in \mathbb{R}^3$ and base velocity $\boldsymbol{v}_b$, expressed in $\mathcal{B}$, compose the state vector, and their time derivatives are

$$\begin{aligned} \dot{\boldsymbol{p}}_{bt} &= -[\boldsymbol{\omega}_b]^\times \boldsymbol{p}_{bt} - \boldsymbol{v}_b, \\ \dot{\boldsymbol{v}}_b &= -[\boldsymbol{\omega}_b]^\times \boldsymbol{v}_b + \boldsymbol{a}_b, \end{aligned} \tag{5.34}$$

where $\boldsymbol{a}_b \in \mathbb{R}^3$ is the spacecraft acceleration. Eq. (5.34) is the prediction step of the filter, where $\boldsymbol{\omega}_b$ and $\boldsymbol{a}_b$ are measured by the inertial measurement unit (IMU), including the gyro and the accelerometer.
The measurement equation is

$$\tilde{\boldsymbol{p}}_{bt} = \boldsymbol{p}_{bt}, \tag{5.35}$$

where $\tilde{\boldsymbol{p}}_{bt} \in \mathbb{R}^3$ is the measurement vector. The Kalman filter scheme is implemented using Eqs. (5.34)-(5.35).
Also for the accelerometer, the noise model (5.33) is used [72]. On the other hand, for the camera, the noise is introduced by adopting the exponentially correlated random variable model, whose equation is reported in (3.17)-(3.18).
The standard deviations and biases of the considered noise models are reported in Tab. 5.2. The vision system acquires measurements at 3 Hz, while the other sensors work at 200 Hz. The filter prediction step is performed at 200 Hz, whereas the update step at 3 Hz. Note that the attitude is controlled to be fixed. To achieve this goal, attitude measurements are necessary, and thus it is assumed that the spacecraft is equipped with a star tracker, which measures the Euler angles $\boldsymbol{\Phi} \in \mathbb{R}^3$. The exponentially correlated random variable model (Eqs. (3.17)-(3.18)) is used to reproduce the noise of the sensor, with standard deviation $\sigma_\Phi = 1.04 \cdot 10^{-4}$ rad. The star tracker

Table 5.2: *Standard deviations and biases of the considered noise model.*

σ_q [rad]	$\sigma_{\dot{q}}$ [rad/s]	σ_τ [Nm]	$\sigma_{p_{bt}}$ [m]	$\sigma_{b\omega}$ [μrad/s$^{3/2}$]
$5 \cdot 10^{-5}$	10^{-4}	0.2	0.01	$3.162 \cdot 10^{-4}$

σ_ω [μrad/s$^{1/2}$]	σ_{ba} [m/s$^{5/2}$]	σ_a [m/s$^{3/2}$]	$b_{\omega,0}$ [rad/hr]	$b_{a,0}$ [m/s^2]
0.316	$6.00 \cdot 10^{-5}$	$9.81 \cdot 10^{-5}$	0.0017	0.003

works at 3 Hz, while the controller works at 200 Hz. Hence, the EKF for quaternions presented in [73] is implemented [2]. Similar to the filter for the base velocity, the prediction is run at 200 Hz, while the update at 3 Hz.

5.6.3 Observers comparison

In [74] [3] the better performance of the proposed method based on a centroid-joints dynamics are shown considering a simplified Gaussian noise model for the linear velocity. In that case, the noise on consecutive measurements is completely uncorrelated and this feature deteriorates significantly the performance of the observer (5.1), and consequently the accuracy of the external wrench estimation. In this analysis, a more realistic condition is considered: the linear velocity is estimated through a Kalman filter, and thus it turns out to be less noisy. However, after the filter has converged, the estimation is still affected by a certain level of uncertainty. When the prediction is updated, at a frequency of 3 Hz, the velocity estimate may vary suddenly of few mm/s. This is due to the fact that the prediction step runs at a higher frequency and the error in the predicted states is accumulated. These sudden variations in the correction phase affect significantly the computation of the residuals depending on the linear velocity, namely all the ones in (5.1) and $\hat{\boldsymbol{f}}_{ext,c}$. Consequently, the accuracy of the contact wrench reconstruction deteriorates. To mitigate this issue, the observers gains should be decreased considerably, limiting the bandwidth. Conversely, the issue is completely overcome if the external wrench is estimated through (5.23), since $\hat{\boldsymbol{m}}_{ext,c}$ and $\hat{\tilde{\boldsymbol{\tau}}}$ are decoupled from the base linear velocity. Before proceeding with the comparison, note that, in this simulation, the contact point is at the end-effector, and thus it is assumed to be known.
Figs. 5.2 and 5.3 show a comparison between the reviewed method [47], adapted to space robots, and the proposed one. Fig. 5.2 compares the two

[2] In [73] the filter estimates also the angular velocity and the measurements are assumed to be acquired by a laser vision system. In this work, only the attitude is estimated and the measurements are provided by the star tracker, but the implementation of the filter is analogous.

[3] In [74], a preliminary analysis of the observers for space robots is reported. In this thesis, a more complete discussion is present, including a more realistic measurements model and the reconstruction of the linear velocity.

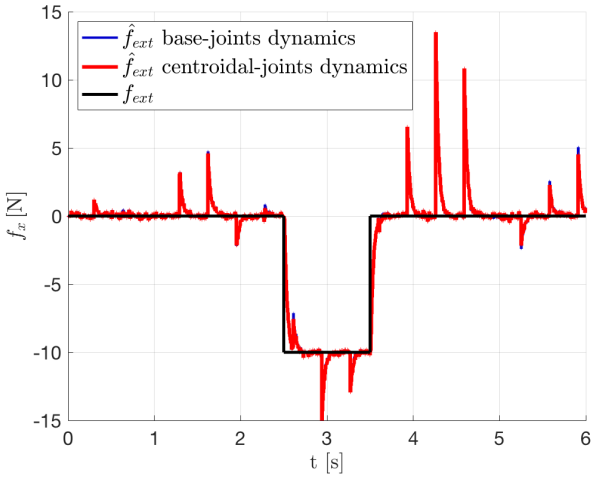

Figure 5.2: *Comparison between the reviewed observer and the proposed one, including* $\hat{\boldsymbol{f}}_{ext,b}$ *and* $\hat{\boldsymbol{f}}_{ext,c}$ *in the estimation process.*

methods when all the three residuals are used to reconstruct $\boldsymbol{f}_{ext}$. In this case, for the observer based on a base-joints dynamics, i.e., given by (5.1), a contact force estimate $\hat{\boldsymbol{f}}_{ext}$ is computed by taking the pseudo inverse of the relation (2.25) and using the residuals $\hat{\boldsymbol{f}}_{ext,b}$, $\hat{\boldsymbol{m}}_{ext,b}$, and $\hat{\boldsymbol{\tau}}_{ext}$, whereas for the observer (5.18) it is given by using the relation (5.22). On the other hand, Fig. 5.3 compares the two methods when only the angular and joint momentum residuals are used to reconstruct $\boldsymbol{f}_{ext}$. For the observer (5.1), the contact force estimate $\hat{\boldsymbol{f}}_{ext}$ is computed removing the first row of (2.25), i.e., without $\hat{\boldsymbol{f}}_{ext,b}$, and by taking the pseudo inverse of the resulting relation, while for the observer (5.18) it is given by using the relation (5.23), i.e., without $\hat{\boldsymbol{f}}_{ext,c}$. In both observers, all the gains are set equal to $30\ \mathrm{s}^{-1}$.
Fig. 5.2 shows that the estimation process is significantly affected by the uncertainty in the linear velocity and both observers provide similar bad performance. This is caused by the residuals $\hat{\boldsymbol{f}}_{ext,b}$ and $\hat{\boldsymbol{f}}_{ext,c}$, which are the ones mostly affected by the explained issue. Only one component of the force is reported, but similar results are obtained for the other two.
On the other hand, the simulation shown in Fig. 5.3, in which $\hat{\boldsymbol{f}}_{ext,b}$ and $\hat{\boldsymbol{f}}_{ext,c}$ are not used in the estimation process, highlights the advantage of using the proposed scheme based on the centroid-joints dynamics. Indeed, it provides a definitely more accurate estimate of the external force, especially during the contact. It is worth stressing that the superior performance of the proposed method derives from the complete decoupling of $\hat{\boldsymbol{m}}_{ext,c}$ and

$\hat{\bar{\boldsymbol{\tau}}}_{ext}$ from the linear velocity $\boldsymbol{v}_b$. The estimation through (5.23) turns out to be more practical and robust since it requires the use of only reliable and accurate sensors, as gyros, encoders and torque sensors. Moreover, these sensors can work at higher frequency, up to 1 KHz, providing the capability of detecting fast contacts. The estimation based on a centroid-joints dynamics does not depend on the performance of the filter which can even deteriorates due to occlusions of the camera or adverse light conditions, here not simulated.
Finally, the residuals $\hat{\boldsymbol{m}}_{ext,c}$ and $\hat{\bar{\boldsymbol{\tau}}}_{ext}$ turn out to be more adequate monitoring signals for the detection of the contact. Indeed, they are less prone to false positive than the residuals in (5.1), which show some spikes (visible in Fig. 5.3 in the force reconstruction) due to the uncertainty in the linear velocity estimation.

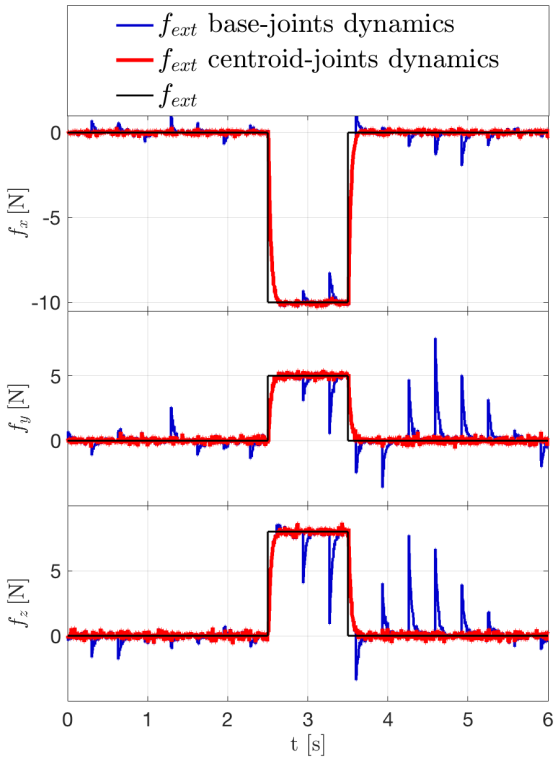

Figure 5.3: *Comparison between the reviewed observer and the proposed one, without using $\hat{\boldsymbol{f}}_{ext,b}$ and $\hat{\boldsymbol{f}}_{ext,c}$ in the estimation process.*

5.6.4 Reconstruction of the contact force on a generic point

In this section, it is shown that the proposed estimation scheme based on a centroid-joints dynamics can be used to detect and reconstruct a contact force acting on a generic point along the robot. First, the contact is detected using the residuals $\hat{\boldsymbol{m}}_{ext,c}$ and $\hat{\tilde{\boldsymbol{\tau}}}$. Then, in order to estimate the force, the contact point is isolated through the method explained in Sect. 5.5.2 and reported schematically in Fig. 5.1, which relies only on the joint and angular momentum residuals. Finally, the external force is estimated using Eq. (5.23), which requires the knowledge of contact point. The space robot is commanded to keep the initial attitude and manipulator's configuration, i.e., $\boldsymbol{q}_0 = [0\ 40\ 0\ 110\ 0\ 45\ 0]$ deg.
Similarly to the previous case, a constant external wrench is applied between $t = 2.5$ s and $t = 3.5$ s and it consists of only a linear force and no torque. In this case, the external wrench acts on a mid-section on the link 4. In this simulation, the observer's gains are set equal to $20\ \text{s}^{-1}$.
The contact point is isolated with an error of few centimeters. Then, Eq. (5.23) is used to estimate the contact force $\boldsymbol{f}_{ext}$. Fig. 5.4 shows that the proposed method provides good estimation performance even in the case of a contact on a generic point along the robot.

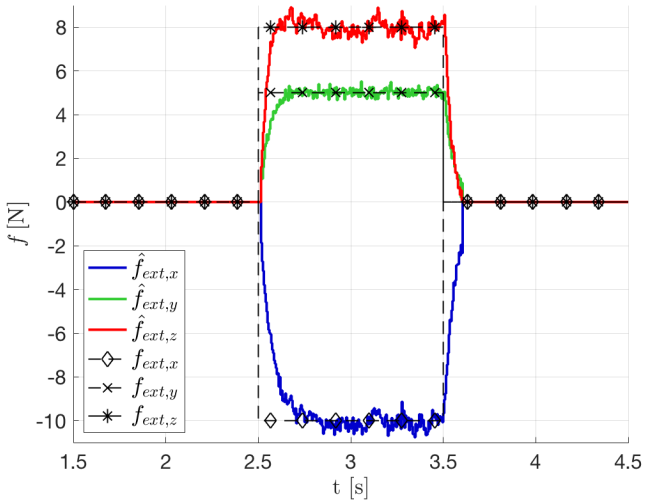

Figure 5.4: *Reconstruction of the external force acting on a generic point along the robot.*

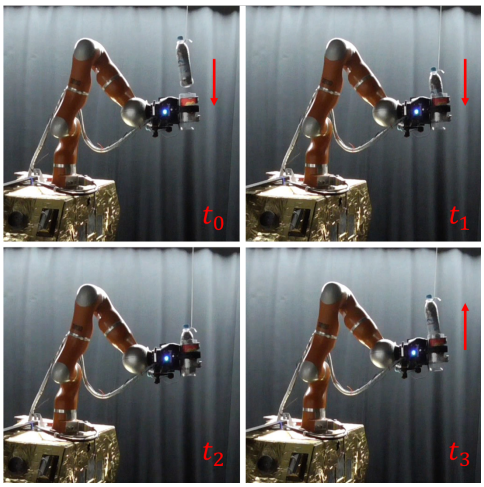

Figure 5.5: *Sequence of the experiment with a known mass (from top to bottom, from left to right).*

5.7 Experimental validation

As already explained, servicing missions are extremely complex and require advanced technologies which must be thoroughly tested before the launch. To this aim, both observers (5.1) and (5.18) have been validated on the On-Orbit Servicing Simulator (OOS-Sim) hardware-in-the-loop facility [51] at the DLR. This is a robotic simulator reproducing the in-orbit dynamics of a space robot. Thanks to the OOS-Sim, it is possible to test the algorithms, which will run on the space robot, on ground, before the actual deployment in orbit. The facility is made up of two parts: a simulator arm and a test arm. The former one is a position-controlled KUKA KR120 industrial robot which reproduces the 6DoF spacecraft's dynamics based on a real-time model integration. The latter one is a torque-controlled KUKA KR4+ lightweight robot with seven degrees of freedom, which is mounted on a satellite mockup moved by the simulator arm. In the test arm, the joint gravity torques are compensated based on an identified model, replicating the microgravity conditions. In addition to reproducing the spacecraft-manipulator dynamic coupling, the facility enables to test the observers during a true physical interaction, which is difficult to simulate numerically. Moreover, many nonidealities are taken into account, such as sensor noise, time delay, discretization, model uncertainties, friction and flexibility in the joints of the test arm. It is clear that the validation on the OOS-Sim, whose results are reported in the following, is a very important step to prove the

observers' applicability in a real scenario. It is worth recalling that also the observer (5.1), initially developed for humanoids in [47], has never been tested on real hardware before.
Before proceeding with the details of the experiments, a last remark is necessary. Differently from the test arm, the dynamics of the spacecraft is simulated based on a model, and its states are reconstructed from the forwards kinematics of the KUKA KR120 industrial robot, featuring very low level of noise and uncertainties compared to the ones expected in space. For this reason, the experiments here presented are relevant to validate the observers on real hardware, but not to compare them. Indeed, as already shown, the better performance of the proposed method are evident when more realistic noise conditions for the spacecraft's states are considered.
In order to verify the accuracy of the observers, first, an experiment in which a known constant force is applied at the end-effector has been performed. Then, the end-effector has been hit multiple times simulating a condition in which consecutive contacts occur close in time, and the correct behavior of the observers is checked. In both experiments, a compliant controller is implemented to control the end-effector position, the space robot's CM and the base attitude. Therefore, the base of the robot is fully actuated. A complete description of the control method is reported in [75].

5.7.1 Experiments with a known force

In these experiments, the gripper mounted on the test manipulator holds a container initially empty. A known mass is laid down in the container and it is removed after a certain period of time (see Fig. 5.5). The resulting action on the space robot is a step-like constant disturbance force acting at the end-effector along the gravity direction. In particular, the disturbance force in the inertial frame is equal to $\boldsymbol{f}_{ext,t} = [0 \ 0 \ -8.373]^T$ N. The observers are required to reconstruct this force correctly. In both observers, all the gains are set equal to $30 \ \mathrm{s}^{-1}$.
Figs. 5.6 and 5.7 show the reconstruction of the external force, expressed in $\mathcal{E}$[4], by the observers (5.1) and (5.18), respectively, using all the residuals. Both the observers are able to estimate the external wrench accurately and no significant differences can be noticed between them. When the mass is laid down and then removed, a small peak appears along the z direction of the end-effector frame. This can be explained by the fact that during these two phases the mass hits the container's wall along that direction, providing a small force.

[4]Note that in the experiment the y direction of the $\mathcal{E}$ frame is almost aligned with the -z direction of the inertial frame (gravity direction).

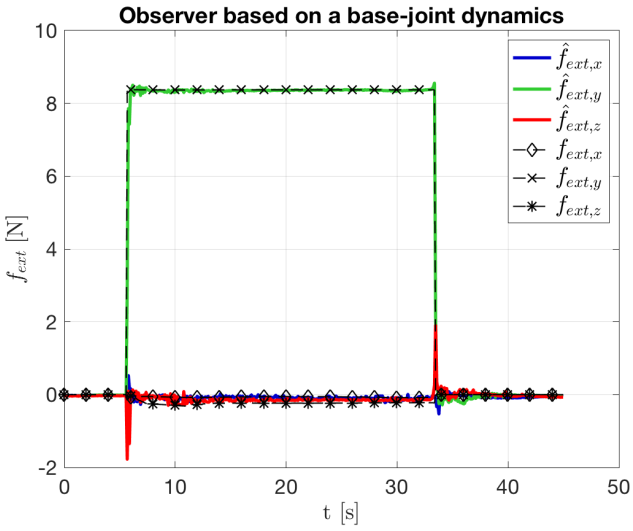

Figure 5.6: *External force estimate using the residuals of the observer based on a base-joint dynamics, including $\hat{\boldsymbol{f}}_{ext,b}$ in the estimation process.*

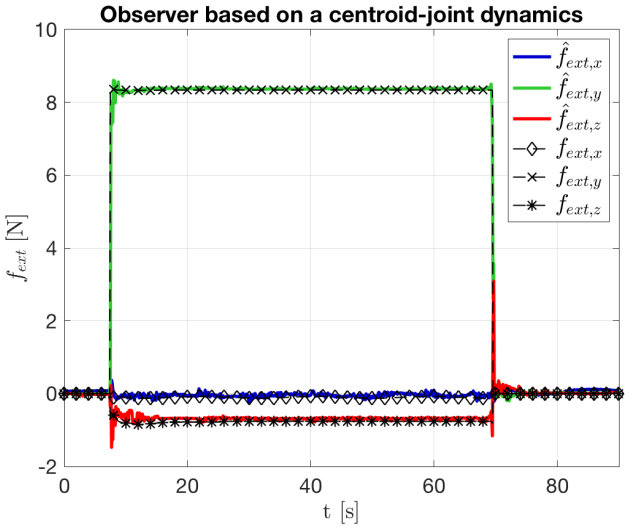

Figure 5.7: *External force estimate using the residuals of the observer based on a centroid-joint dynamics, including $\hat{\boldsymbol{f}}_{ext,c}$ in the estimation process.*

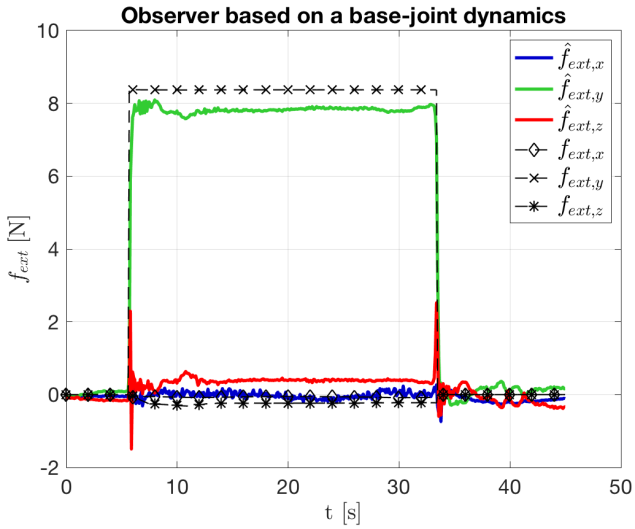

Figure 5.8: *External force estimate using the residuals of the observer based on a base-joint dynamics, without including $\hat{\boldsymbol{f}}_{ext,b}$ in the estimation process.*

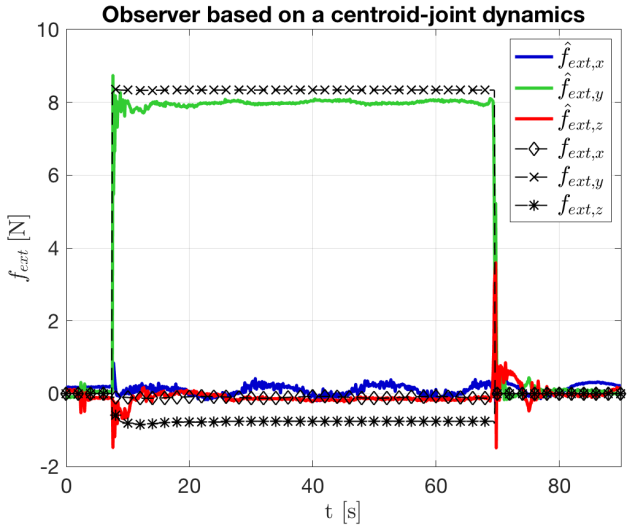

Figure 5.9: *External force estimate using the residuals of the observer based on a centroid-joint dynamics, without including $\hat{\boldsymbol{f}}_{ext,c}$ in the estimation process.*

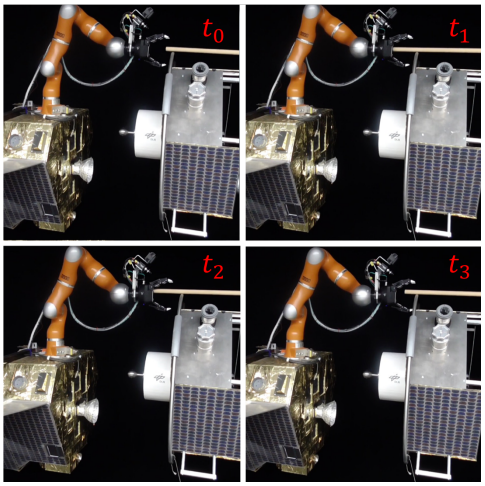

Figure 5.10: *Experiment with consecutive contacts (from top to bottom, from left to right).*

In Figs. 5.8 and 5.9, the results using only the joint and angular momentum residuals in the estimation process are reported, for the schemes (5.1) and (5.18), respectively. Again, the observed behavior is similar. In both cases the estimation of the external force is satisfactory. It can be noticed that the accuracy decreases with respect to the estimation using all the residual vectors. This is due to the fact that the gravity disturbance, affecting the test arm, is not compensated exactly because of uncertainties in the model. Therefore, this introduces an error in the estimates $\hat{\boldsymbol{\tau}}_{ext}$ and $\hat{\bar{\boldsymbol{\tau}}}_{ext}$ which is propagated to the estimate $\hat{\boldsymbol{f}}_{ext}$. In the previous case, Figs. 5.6 and 5.7, this error is mitigated by using the translational momentum residuals in the estimation process. However, note that, first, the gravity compensation error is small, and, second, it is not expected in orbit since the disturbance is induced by the artificial microgravity conditions enforced in the testing facility, whereas in orbit real microgravity conditions would be encountered. It is recalled that these experiments are significant to validate the observers (5.1) and (5.18). However, the better performance of (5.18) can not be appreciated through them since the spacecraft's states are reconstructed through the forward kinematics of the simulator arm, and thus they show a significant lower level of noise and uncertainty than the ones expected in space.

5.7.2 Experiments with consecutive contacts

In this experiment, the test arm was hit with a stick multiple times at the end-effector along different directions (see Fig. 5.10). Short and long con-

tacts were simulated and the behavior of the observers was checked. Only the results related to the observer (5.18) are reported here. However, similar results were obtained for the observer (5.1). The gains for the computation of the translational and angular momentum residuals were set equal to 30 s^{-1}, while they were increased to 100 s^{-1} for the joint momentum residuals.

The direction of the impacts can be seen in Fig. 5.11, which shows the reconstructed contact force at the end-effector, expressed in $\mathcal{E}$. In Figs. 5.12 and 5.13 the residuals $\hat{\hat{\boldsymbol{f}}}_{ext,c}$ and $\hat{\boldsymbol{m}}_{ext,c}$ are reported. It can be noted that, when the force is mostly along the z direction of the end-effector frame, the contact can be easily detected on the x and z components of $\hat{\hat{\boldsymbol{f}}}_{ext,c}$ and on the y component of $\hat{\boldsymbol{m}}_{ext,c}$. On the other hand, between $t = 230$ s and $t = 330$ s, the external force acts along the y-axis of $\mathcal{E}$ and the contact can be detected on the y component of $\hat{\hat{\boldsymbol{f}}}_{ext,c}$ and on the x and z components of $\hat{\boldsymbol{m}}_{ext,c}$. Finally, Fig. 5.14 illustrates the residuals $\hat{\hat{\boldsymbol{\tau}}}_{ext}$. The contacts are detected mostly by the monitoring signals at the first four joints, while the other three remain around zero. In particular, the contacts along the z-axis of $\mathcal{E}$ are detected by the signals at joint 2 and joint 4. Conversely, the contacts along the y-axis of $\mathcal{E}$ are seen by the signals at joint 1 and joint 3.

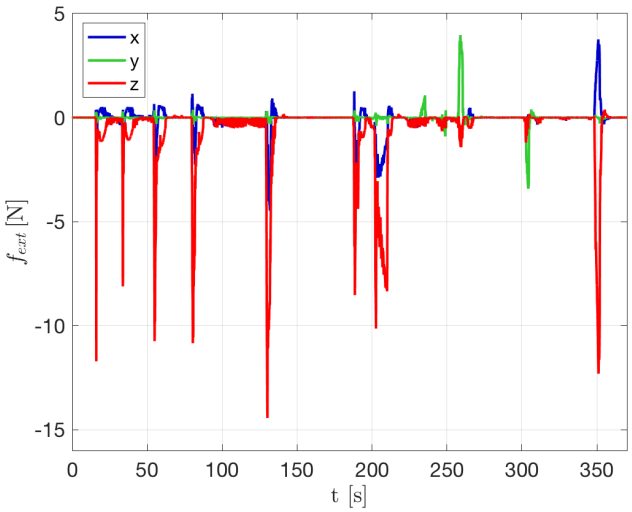

Figure 5.11: *Contact force at the end-effector of the test arm in the consecutive contacts experiment.*

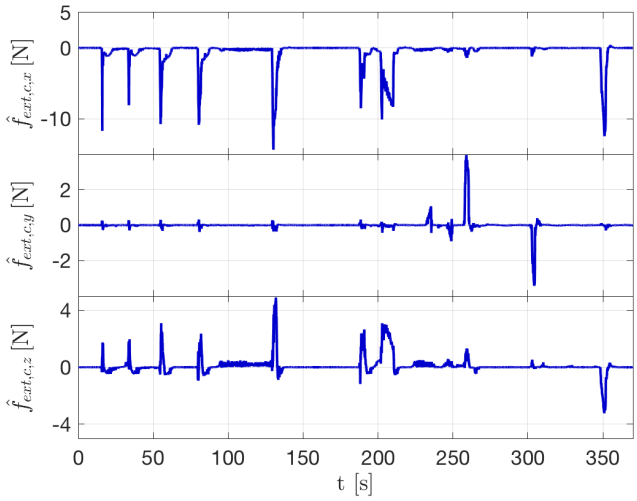

Figure 5.12: *Translation momentum residuals* $\hat{\boldsymbol{f}}_{ext,c}$ *in the consecutive contacts experiment.*

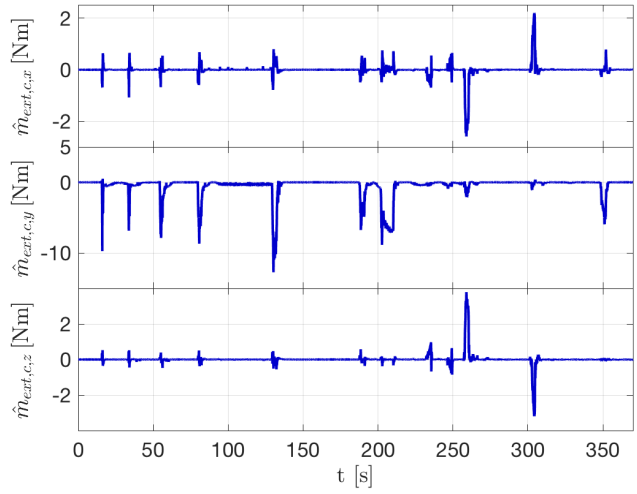

Figure 5.13: *Angular momentum residuals* $\hat{\boldsymbol{m}}_{ext,c}$ *in the consecutive contacts experiment.*

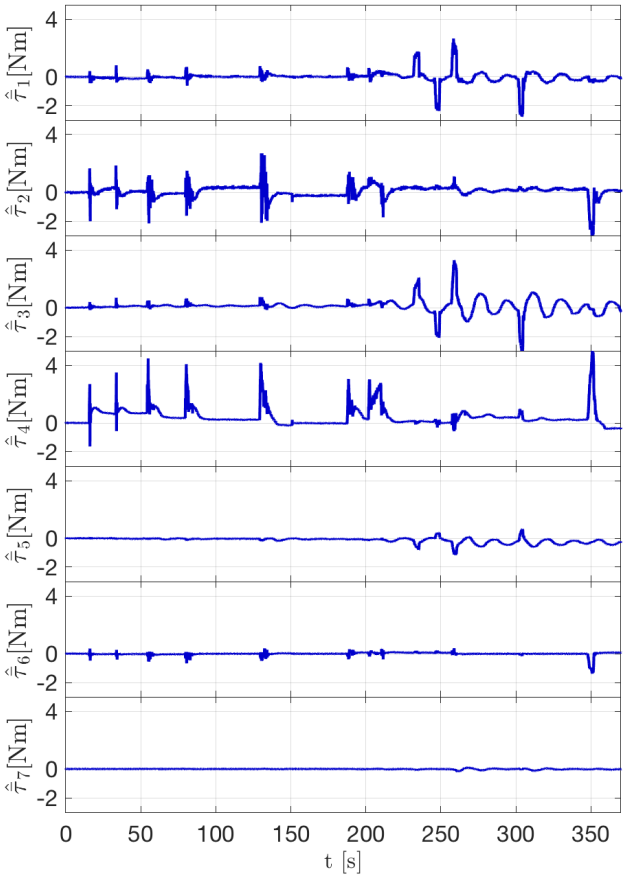

Figure 5.14: *Joint momentum residuals $\hat{\bar{\boldsymbol{\tau}}}_{ext}$ in the consecutive contacts experiment.*

5.8 On using the momentum conservation to deal with contacts

In the literature, many authors have proposed control strategies in which the base of the robot is free to translate or is completely free-floating. This is motivated by the fact that a free-floating solution, or in general a solution without the use of thrusters, enables to save a significant amount of fuel. In this last part of the chapter, another approach to address the detection and isolation problems is presented based on the momentum conservation in the free-floating motion of the spacecraft. The technique is subsequently extended to the actuated-base case, and pros and cons are discussed, also comparing it with the observer.

5.8.1 Contact detection based on momentum monitoring

If the robot operates in free-floating mode, no external forces and moments act on the system and thus the total momentum is preserved. When the contact occurs, the total momentum components, computed in an inertial reference frame, jump from a constant value to another one and therefore they can be exploited as monitoring signals for the detection phase.
To this aim, consider an additional reference frame, oriented as the inertial one, but located on the CM of the whole spacecraft-manipulator ensemble, denoted by $\mathcal{CT}$. Under ideal conditions, either the momentum around $\mathcal{T}$, $\boldsymbol{h}_t \in \mathbb{R}^6$, or the momentum around $\mathcal{CT}$, $\boldsymbol{h}_{ct} \in \mathbb{R}^6$, can be used and their variation can be detected effortlessly. However, a deeper analysis is required for practical implementation since nonidealities, especially measurement noise, affect $\boldsymbol{h}_t$ and $\boldsymbol{h}_{ct}$ differently.
The momenta $\boldsymbol{h}_t$ and $\boldsymbol{h}_{ct}$ can be computed as:

$$\boldsymbol{h}_t = \begin{bmatrix} m\boldsymbol{R}_{tb} & -m\boldsymbol{R}_{tb}[\boldsymbol{p}_{bc}]^\times & m\boldsymbol{R}_{tb}\bar{\boldsymbol{J}}_v \\ m\boldsymbol{R}_{tb}[\boldsymbol{p}_{tc}]^\times & \boldsymbol{I_t}\boldsymbol{R}_{tb} & \boldsymbol{I}_t\boldsymbol{R}_{tb}\hat{\boldsymbol{J}}_\omega \end{bmatrix} \begin{bmatrix} \boldsymbol{v}_b \\ \boldsymbol{\omega}_b \\ \dot{\boldsymbol{q}} \end{bmatrix}, \tag{5.36}$$

$$\boldsymbol{h}_{ct} = \begin{bmatrix} m\boldsymbol{R}_{tb} & -m\boldsymbol{R}_{tb}[\boldsymbol{p}_{bc}]^\times & m\boldsymbol{R}_{tb}\bar{\boldsymbol{J}}_v \\ \boldsymbol{0} & \boldsymbol{I}_c\boldsymbol{R}_{tb} & \boldsymbol{I}_c\boldsymbol{R}_{tb}\tilde{\boldsymbol{J}}_\omega \end{bmatrix} \begin{bmatrix} \boldsymbol{v}_b \\ \boldsymbol{\omega}_b \\ \dot{\boldsymbol{q}} \end{bmatrix}, \tag{5.37}$$

where $\boldsymbol{I}_t \in \mathbb{R}^{3\times3}$ is the rotational inertia around $\mathcal{T}$ of the whole multibody system, and $\hat{\boldsymbol{J}}_\omega, \tilde{\boldsymbol{J}}_\omega \in \mathbb{R}^{3\times n}$ are computed as follows

$$\hat{\boldsymbol{J}}_\omega = \boldsymbol{R}_{tb}^T\boldsymbol{I}_t^{-1}\boldsymbol{R}_{tb}\sum_{i=1}^{n}\boldsymbol{R}_{ib}^T\boldsymbol{I}_i\boldsymbol{J}_{\omega i} + m_i\boldsymbol{R}_{tb}^T[\boldsymbol{p}_{ti}]^\times\boldsymbol{R}_{tb}\boldsymbol{J}_{vi}, \tag{5.38}$$

$$\tilde{\boldsymbol{J}}_{\omega} = \boldsymbol{R}_{tb}^{T}\boldsymbol{I}_{c}^{-1}\boldsymbol{R}_{tb}\sum_{i=1}^{n}\boldsymbol{R}_{ib}^{T}\boldsymbol{I}_{i}\boldsymbol{J}_{\omega i} + m_{i}[\boldsymbol{p}_{bi}]^{\times}(\boldsymbol{J}_{vi} - \bar{\boldsymbol{J}}_{v}), \tag{5.39}$$

As regards the translational momentum, the first row of Eqs. (5.36) and (5.37), the translational velocity $\boldsymbol{v}_b$ is multiplied by the total mass of the system in both $\boldsymbol{h}_t$ and $\boldsymbol{h}_{ct}$. This means that the noise on $\boldsymbol{v}_b$ is amplified, lowering the detection sensitivity for both the cases and thus affecting the choice of the detection technique to be used, as explained in the following. On the other hand, note that the rotational part of $\boldsymbol{h}_{ct}$ shows an interesting decoupling from $\boldsymbol{v}_b$. This is an important property for detection purpose. Indeed, the translational velocity is expected to be the most noisy and uncertain variable, as already explained, and thus to affect significantly the quality of the monitored signals. Consequently, the decoupling from $\boldsymbol{v}_b$ of the angular momentum around $\mathcal{CT}$ enables to achieve higher sensitivity in the detection phase. Moreover, in order to compute $\boldsymbol{h}_t$, measurements of the base position are required, introducing other noise, while they are not necessary to compute $\boldsymbol{h}_{ct}$. Therefore, $\boldsymbol{h}_{ct}$ is expected to provide advantages, as confirmed later in Fig. 5.15, and it is chosen as monitoring quantity.

Depending on the features of the monitored signal, different detection techniques can be exploited. The easiest and, probably, the promptest approach to address the detection problem is to define a threshold below which the modulus of the monitored signal should lie. This approach is suitable for relatively low-noise signals, and thus in this analysis is applied to detect variation in the rotational momentum components. However, it is not particularly robust, in terms of false positives, when dealing with high-noise signals, like the translational momentum. In this case, a more robust technique is necessary. Different solutions have been developed in literature. In this analysis the Intersection of Confidence Intervals Change Detection Test (ICI-CDT) has been chosen, which was developed to run on embedded systems, i.e., systems with low computational capability. This strategy is a sequential change detection test that can work with noisy data without prior statistical information about the process, which is acquired in an initial training phase. It exploits the ICI-rule which is a technique that regularizes Gaussian-distributed data through polynomial regression computed on adaptive support. Especially, for the change detection test, a 0^{th} polynomial is considered since the signal is expected to be stationary.
Consider non Gaussian data. During the training phase, a training time T_0 is chosen and the available data are windowed in disjointed subsequences

composed of N instances. For each subsequence s, the sample mean $M(s)$, which is Gaussian distributed thanks to the central limit theorem, is computed. Note that it is necessary to introduce the sample mean $M(s)$ because the ICI rules work only on Gaussian-distributed data. If the incoming data are already Gaussian distributed, the algorithm can use directly them, and thus $N = 1$. The mean and standard deviation of $M(s)$, over the training set composed of $S_0 = T_0/N$ subsequences, are computed. These estimates define the confidence interval for the mean feature:

$$\Upsilon_{S_0}^M = \left[\mu_{S_0}^M - \Gamma_{cdt}\sigma_{S_0}^M, \mu_{S_0}^M + \Gamma_{cdt}\sigma_{S_0}^M\right], \tag{5.40}$$

with $\Gamma_{cdt} > 0$ controlling the amplitude of the interval. In a real scenario, the training phase is carried out before the beginning of the desired task. For instance, a series of simple manipulator's maneuvers can be designed to collect momentum information for this phase.
Once the training is completed, the ICI-CDT becomes operational. Every time N data are available, a new sequence s is created and feature extracted to populate Υ_s^M.
The ICI-rule is used to verify whether the new feature instance can be intended as a realization of the existing distribution. If not, a drift is detected. Basically, it computes the intersection of all the confidence intervals up to the current one and when the result is an empty set a change is detected. A more comprehensive discussion of these strategies can be found in [76] and [77].
The versatility, namely the possibility to work with both Gaussian ($N = 1$) and non Gaussian noise (usually, $N \geq 20$), the capability of working with high level of noise, with respect to the signal variation, and the low computational power required are the main advantages of the ICI-CDT. This technique has the main drawbacks of having to wait for N observations, in case of non Gaussian noise, and, in any case, of an increasing delay as time passes. However, the latter disadvantage could be mitigated by periodically resetting the method, each time restarting from the information of the last training.
In both strategies, i.e., the threshold approach and the ICI-CDT, a confidence parameter is used to modify the sensitivity; especially, a tradeoff between detection promptness and robustness to false positives must be made.
As last remark, in order to mitigate the occurrence of false positives, a second layer that validates the detection could be introduced. In this case, the fact that translational and rotational momentum are related to each other could be exploited to this aim. For instance, if a change is detected in some components of the rotational momentum, a change is also expected in the

translational momentum and thus this additional information can be used to validate the first detection with a certain degree of confidence. For this reason, it could be worth being able to detect changes in both rotational and translational momentum.

5.8.2 Contact isolation based on momentum monitoring

A strategy similar to the one exploiting all the residuals of the observer (see Sect. 5.5.2) can be applied to address the isolation problem.
Assuming that the contact phase is short, i.e. the point of application of the generalized contact force does not change, and that the contact only consists of a linear force and no torque, the translational and angular momentum can be exploited to isolate the contact. Indeed, considering $\boldsymbol{h}_{ct} = [\boldsymbol{h}_{ct}^{t\,T}\ \boldsymbol{h}_{ct}^{r\,T}]^T$, the second cardinal equation of dynamics can be written as

$$\frac{d\boldsymbol{h}_{ct}^r}{dt} = \boldsymbol{m}_{ext,ct} = [\boldsymbol{p}_{ctp}]^\times \boldsymbol{f}_{ext,ct} = [\boldsymbol{p}_{ctp}]^\times \frac{d\boldsymbol{h}_{ct}^t}{dt}, \tag{5.41}$$

where $\boldsymbol{f}_{ext,ct}, \boldsymbol{m}_{ext,ct} \in \mathbb{R}^3$ are the components of the projection in $\mathcal{CT}$ of $\boldsymbol{\mathcal{F}_{ext}}$ and $\boldsymbol{p}_{ctp} \in \mathbb{R}^3$ is the position vector from frame $\mathcal{CT}$ to the contact point. Integrating Eq. (5.41), under the assumptions previously stated, the following relation can be obtained:

$$\Delta\boldsymbol{h}_{ct}^r = [\boldsymbol{p}_{ctp}]^\times \Delta\boldsymbol{h}_{ct}^t, \tag{5.42}$$

Hence, the contact point lies on the line

$$\boldsymbol{l}_p = (-[\Delta\boldsymbol{h}_{ct}^t]^\times)^\# \Delta\boldsymbol{h}_{ct}^r + k\frac{\Delta\boldsymbol{h}_{ct}^t}{||\Delta\boldsymbol{h}_{ct}^t||} \in \mathbb{R}^3, \tag{5.43}$$

which passes through the contact point. Knowing $\boldsymbol{l}_p$ and the configuration of the space robot at the contact time, it is possible to find the contact point, and consequently $\boldsymbol{p}_{ctp}$, as the intersection between the line and the robot, whose representation could be simplified exploiting primitive shapes.

5.8.3 Numerical simulations

A spacecraft equipped with a 3DoF manipulator is considered. The kinematics and dynamics parameters are reported in Tab. 5.3.
Three situations are simulated, in which the robot is moving and impacts a free-floating object at a certain time instant:

- **Case I**: the system is initially stationary and the initial joints angles are $\boldsymbol{q}_0 = [25\ \ -45\ \ 81]^T$ deg. At time $t = 2$ s, the first and third

Table 5.3: *Kinematics and dynamics parameters.*

	l [m]	m [kg]	I_x [kgm^2]	I_y [kgm^2]	I_z [kgm^2]
Base	-	150	15.0	21.8	18.88
Link 1	0.17	3	0.03	0.03	0.03
Link 2	1.3	9	1.65	1.65	0.64
Link 3	1.3	6	0.25	0.25	0.03

joints are commanded to follow a trapezoidal velocity profile to reach a maximum velocity of 4.3 deg/s and -0.86 deg/s, respectively, in 1 s. At time $t = 3.887$ s, the third link impacts the free-floating object.

- **Case II**: the system is initially stationary and the initial joints angles are $\boldsymbol{q}_0 = [0\ 45\ 81]^T$ deg. At time $t = 2$ s, the third joint is commanded to follow a trapezoidal velocity profile to reach a maximum velocity of -0.86 deg/s in 1 s. At time $t = 3.202$ s, the third link impacts the free-floating object.

- **Case III**: the system is initially stationary and the initial joints angles are $\boldsymbol{q}_0 = [0\ 45\ 81]^T$ deg. At time $t = 2$ s, the first joint is commanded to follow a trapezoidal velocity profile to reach a maximum velocity of -0.86 deg/s in 1 s. At time $t = 5.83$ s, the first link impacts the free-floating object.

The contact between the robot and the object is simulated exploiting the *Dymola* library presented in [78], in which the normal force to the contact surface is modeled as follows:

$$f_n = K\delta^d + D\delta^d\dot{\delta}, \tag{5.44}$$

where $K \in \mathbb{R}$ and $D \in \mathbb{R}$ are the elastic and damping coefficients, $\delta \in \mathbb{R}$ is the penetration in the normal direction and $d \in \mathbb{R}$ is a parameter depending on the shape of the colliding objects. The tangential components of the contact force are null since friction is neglected. For the three cases, different parameters are set and are reported in Tab. 5.4. In *case I* the generated contact force is higher and its modulus is about 75 N; in *case II* the contact force has a modulus of about 15 N; in *case III* the contact force is lower with a modulus less than 5 N.
The measurements are simulated using the noise models presented for the observers. The same standard deviations are used for the Gaussian noise. In this simulations, no filters are implemented and the attitude and linear velocity measurements are modelled adding a Gaussian noise with zero mean

Table 5.4: *Contact force parameters.*

	Case I	Case II	Case III
K [N/m^d]	$2 \cdot 10^7$	$5 \cdot 10^6$	$5 \cdot 10^6$
D [Ns/m$^{(d+1)}$]	$9 \cdot 10^4$	$5 \cdot 10^3$	$5 \cdot 10^3$
d [-]	1.5	1.5	1.5

and standard deviations of 0.026 rad and of 0.001 m/s, respectively. Attitude angles measurements are acquired with a frequency of 3 Hz, while the other measurements are acquired with a frequency of 100 Hz. For the ICI-CDT, Γ_{cdt} is set equal to 2 and N equal to 20. For each case, 10 simulations are performed and mean detection time and isolation accuracy and settling time are evaluated.
Case II is used also to analyze the effects of model uncertainties on the performance. Especially, some uncertainties in the inertia matrix of the base and in the position of the base CM are introduced. 100 Gaussian-distributed models are generated, considering 20% uncertainty on the diagonal terms and 10% uncertainty on the off-diagonal terms of the inertia matrix, and 10% uncertainty on the CM. Then, the mean performance is evaluated. In this analysis, no measurement noise is taken into account.
In the following, firstly, the results of the simulations considering only measurement noise are discussed. Afterwards, the analysis continues assessing the performance in presence of model uncertainties, without noise. The choice of introducing nonidealities one by one is made to understand better their effects.

Before proceeding with the simulation results, Fig. 5.15 shows the effects of noise on the component y of the rotational momentum. At the beginning, an ideal condition is considered, then at time $t = 1$ s noise is switched on. As expected, rotational momentum around $\mathcal{CT}$ is less affected by noise than the one around $\mathcal{T}$, thanks to the decoupling from $\boldsymbol{v}_b$. It is worth stressing that this property guarantees a higher sensitivity to detection. Similar results can be obtained on the other two components.
Consider the simulations with only measurement noise affecting the system. Tab. 5.5 shows the detection delay for each component of $\boldsymbol{h}_{ct}$. The dash indicates that no variation occurred in the corresponding component. As explained, the change detection is performed with the ICI-CDT approach for the linear momentum, while with the threshold approach for the angular momentum. Both the techniques succeed in recognizing a drift in the stationarity of momentum. As expected, the threshold approach turns

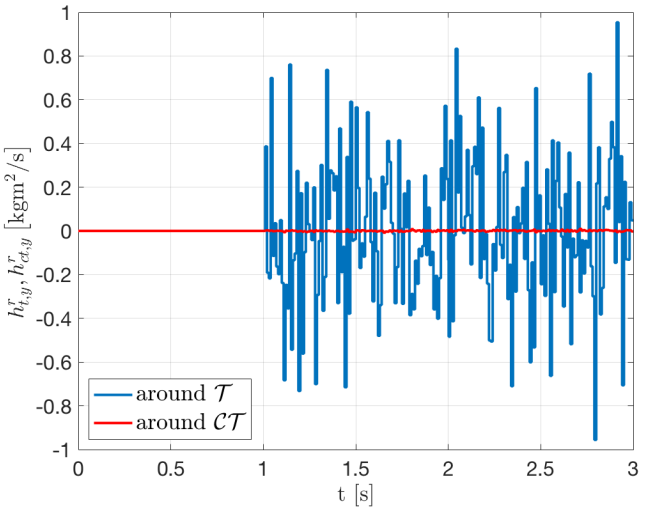

Figure 5.15: *Effects of noise on the rotational momentum around $\mathcal{T}$ and $\mathcal{CT}$.*

out to be prompter with a detection delay of few milliseconds, basically limited only by the acquisition frequency. On the other hand, it is possible to appreciate the capability of the ICI-CDT of detecting variation comparable to the level of noise, even if with an increased delay. To provide a visualization of this statement, Fig. 5.16 shows the variation in the component x of the total momentum after the collision in one simulation of *case I*. Finally, not surprisingly, the higher the intensity of the impact, the faster the detection of the contact. Indeed, the ratio between the variation in the component and the level of noise is higher.

Table 5.5: *Detection delay in seconds for each component of $\boldsymbol{h}_c$.*

	Case I	Case II	Case III
$h^t_{ct,x}$	0.595	1.399	4.116
$h^t_{ct,y}$	0.215	-	-
$h^t_{ct,z}$	-	0.879	3.532
$h^r_{ct,x}$	0.013	-	-
$h^r_{ct,y}$	0.024	0.018	0.030
$h^r_{ct,z}$	0.013	-	-

As regards the isolation, the contact point is refined iteratively computing the mean of consecutive estimates. In this way, a filtering of the noise is achieved. Tab. 5.6 reports the mean accuracy of the estimated contact point over 10 simulations with noise. The following performance parameters are

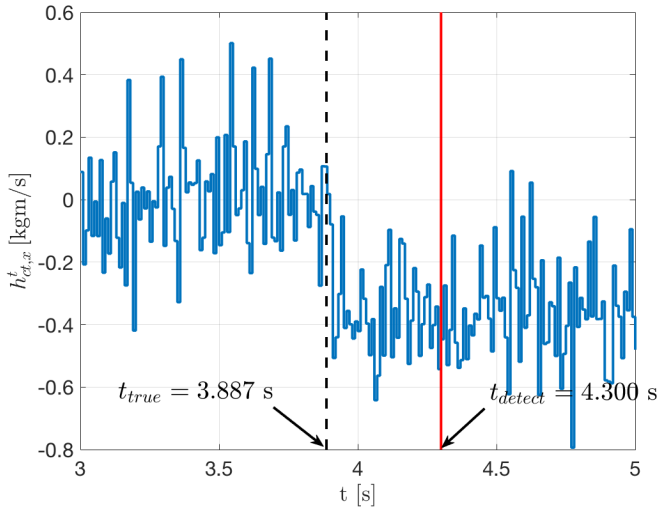

Figure 5.16: *Variation in the component x of $\boldsymbol{h}_{ct}$ due to the collision in one simulation of case I.*

used:

- absolute error $\boldsymbol{e}$;
- percent error $\boldsymbol{e}_{\%}$, considering the maximum extension of the arm as characteristic length;
- percentage of cases with correct identification of the contact link $l_{\%}$;
- the settling time t_s to reach 95% of the steady state value.

In all the simulated cases, the momentum monitoring approach provides good accuracy performance. The impacted link is always identified in *case I* and *case II*, while a failure occurs in 10% of the simulations in *case III*. The contact point is isolated with an accuracy in the order of centimeters. However, the settling time, to reach a steady state value of the estimation, tends to increase significantly when the impact force is lower and thus measurement noise is more prominent.

Finally, the performance in presence of model uncertainties is discussed. Only isolation accuracy results are reported since uncertainties affect more the isolation problem than the detection one, in which noise is prevalent.

Table 5.6: *Isolation accuracy in case of measurement noise.*

	Case I	Case II	Case III
e_x [cm]	0.48	5.12	10.73
e_y [cm]	0.24	0.003	0.03
e_z [cm]	0.88	3.64	11.05
$e_{x,\%}$	0.17	1.84	3.87
$e_{y,\%}$	0.09	0.001	0.009
$e_{z,\%}$	0.32	1.31	3.99
$l_\%$	100	100	90
t_s [s]	0.11	0.77	3.76

In Tab. 5.7, it can be observed that the error in the estimation of the contact position is in the order of centimeters and the link is always identified correctly.

Table 5.7: *Isolation accuracy in case of model uncertainties.*

e_x [cm]	e_y [cm]	e_z [cm]	$e_{x,\%}$	$e_{y,\%}$	$e_{z,\%}$	$l_\%$
2.67	2.67	2.62	0.97	0.97	0.96	100

5.8.4 Extension to actuated-base robot

In this section, the problem of extending the proposed strategy to an actuated-base robot is analyzed. An idea could be to separate the contribution to the momentum due to the contact force and due to the control inputs. Therefore, if $\boldsymbol{f}_b$ and $\boldsymbol{m}_b$ are available, for example from the controller, the momentum around $\mathcal{CT}$ due to the external disturbance, $\boldsymbol{h}_{ct}^{ext} \in \mathbb{R}^6$, can be derived as:

$$\boldsymbol{h}_{ct}^{ext} = \begin{bmatrix} \boldsymbol{h}_{ct}^{ext,t} \\ \boldsymbol{h}_{ct}^{ext,r} \end{bmatrix} = \begin{bmatrix} \boldsymbol{h}_{ct}^{t} \\ \boldsymbol{h}_{ct}^{r} \end{bmatrix} - \int_0^t \boldsymbol{A}_{ctb}^{-T} \begin{bmatrix} \boldsymbol{f}_b \\ \boldsymbol{m}_b \end{bmatrix} ds, \tag{5.45}$$

In this way, the problem becomes analogous to the previous one with the free-floating base and thus the same strategies can be exploited.
In this analysis, the system is initially stationary and the initial joints angles are $\boldsymbol{q}_0 = [0 \ 45 \ 81]^T$ deg. At time $t = 2$ s, the third joint is commanded to follow a trapezoidal velocity profile to reach a maximum velocity of -0.86 deg/s in 1 s. At time $t = 5$ s, a contact force, whose modulus is about 21 N, is introduced on the third link. The spacecraft is controlled with a PD to keep the initial position and attitude. Thrusters and reaction wheels are used as actuators. Especially, the thrusters are used only to control the

translation and the reaction wheels the rotation. The reaction wheels are in pyramid configuration and the inertia of each wheel is 0.029 kgm^2. A pulse-width pulse-frequency modulation is used for the thrusters. In order to simulate the difference between the commanded force and the actual one provided by the thrusters, a delay of 2 ms and a first order filter with time constant of 12 ms are introduced in the simulation. The noise model and the level of uncertainties are the same of the free-floating case. Here, 100 simulations are performed generating different conditions of uncertainties (the same level of uncertainties used for the free-floating case) and the mean performance are evaluated. Note that in this simulation both nonidealities are considered together. The performance of the momentum monitoring approach in case of actuated-base is reported in Tabs. 5.8 and 5.9.

Table 5.8: *Detection delay in seconds for each component of* $\boldsymbol{h}_{ct}^{ext}$.

$h_{ct,x}^{ext,t}$	$h_{ct,y}^{ext,t}$	$h_{ct,z}^{ext,t}$	$h_{ct,x}^{ext,r}$	$h_{ct,y}^{ext,r}$	$h_{ct,z}^{ext,r}$
5.216	1.991	3.170	0.019	0.019	0.019

Table 5.9: *Isolation accuracy in case of measurement noise and base actuation.*

e_x [cm]	e_y [cm]	e_z [cm]	$e_{x,\%}$	$e_{y,\%}$	$e_{z,\%}$	$l_\%$	t_s [s]
7.04	3.19	6.37	2.54	1.15	2.30	100	2.35

As in the free-floating case, the contact detection is easier and faster on the components of the rotational momentum, while the delay in the detection is significant using the translational momentum. Again, this is due to the fact that the uncertainties and noise on the linear velocity are amplified in the computation of this momentum (see Fig. 5.17). Moreover, the discrepancy between the commanded force and the real force due to the thrusters dynamics affect significantly the translational momentum.
The isolation accuracy seems satisfying. However, note that, in this case, the settling time to obtain that accuracy is very long, again due to the effects of nonidealities mainly on the translational momentum.

5.8.5 Momentum monitoring approach vs contact force observer

The momentum monitoring approach is very straightforward, especially in the free-floating motion. It seems the most natural approach: when a contact occurs, the jump in the momenta is exploited to detect it. Moreover, translational and rotational momentum can be used to isolate the contact.

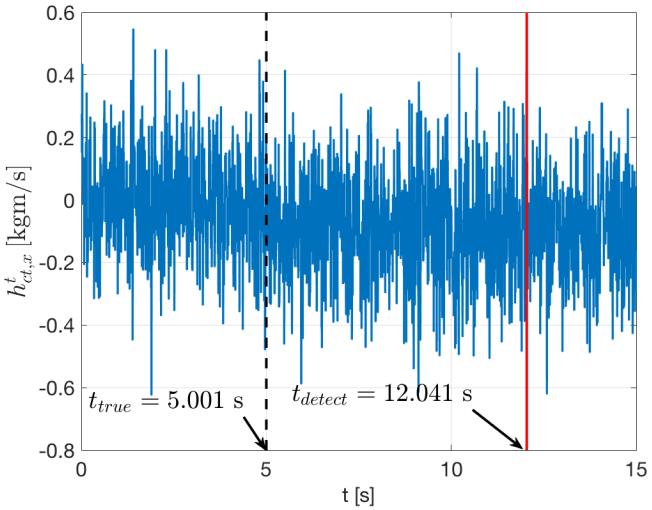

Figure 5.17: *Variation in the component x of $\boldsymbol{h}_{ct}$ due to the collision in one simulation of the actuated-base case.*

However, it has been shown that nonidealities, such as noise and uncertainties, affect significantly the computation of the total momentum, since nonidealities are amplified. Hence, the sensitivity in the detection is considerably decreased. Only for the rotational momentum, this fact is mitigated computing it around the center of mass of the whole system. Consequently, advanced and complex techniques are required to detect variation in the translational momentum and the isolation point is identified accurately with a long delay. In addition, consider the isolation strategy with the momentum monitoring. First, it is based on the assumption that the contact force is short in time, and thus it does not work properly with continuous contact. Second, in case of multiple intersections between the force line of action and the robot, it is not always easy to select the right point. Finally, both translational and rotational momentum require the knowledge of the attitude angles, whose acquisition is usually at low frequency.
The contact wrench observer, especially the one based on a centroid-joints dynamics, overcomes many of these issues. Indeed, the residuals $\hat{\boldsymbol{m}}_{ext,c}$ and $\hat{\tilde{\boldsymbol{\tau}}}_{ext}$ are computed relying only on accurate sensors with high acquisition frequency, providing a faster detection with a higher sensitivity. Therefore, a simple threshold approach can be used as detection technique, regulating the level of noise through the gains of the observer. Then, note that even if the line of action of the contact force passes through the center of mass of the space robot, which means no variations in $\hat{\boldsymbol{m}}_{ext,c}$ and in $\boldsymbol{h}_{ct}^{r,ext}$,

information related to the force are included in $\hat{\tilde{\boldsymbol{\tau}}}_{ext}$ (see Eq. (5.20)) and the contact is still detected. Moreover, they can be used to locate the exact contact point along the robot with a good accuracy and promptness. Finally, the observer enables to address not only the detection and isolation problems, but also the identification problem jointly. The main drawback of this approach is the need of computing the derivative of the inertia matrix (see Eqs. (5.14)-(5.15)-(5.16)). An efficient online algorithm to this aim was proposed in [79].

To conclude, the observer based on a centroid-joints dynamics turns out to be a better-performing and practical solution to address the detection, isolation and identification problems of a generic contact along the robot. Actually, the information of the observer and the momentum monitoring could be used together to increase the robustness of the system. Imagine an autonomous robot equipped with a contact handling system made up of two layers. In the first layer, the first and fast detection is performed, along with the isolation and a safe reaction strategy. The second layer uses all the information available to validate the detection. For instance, if a contact causes a variation in the y-component of the residual $\hat{\boldsymbol{m}}_{ext,c}$, there will be a variation also in some components of $\boldsymbol{h}_{ct}^{r,ext}$ and probably also in some components of $\hat{\tilde{\boldsymbol{\tau}}}_{ext}$. Therefore, the second layer looks for other variations in the monitoring signals and checks if they are compatible with the one detected. In this way, it is possible to validate the first detection with a certain degree of confidence, and then decide the following action. This is just an idea for future work, but it is not developed in this thesis.

CHAPTER 6

Reaction control to unexpected collisions

Once the contact has been detected and identified, two situations can be considered, requiring different control strategies. If grasping or manipulation tasks were planned and the contact has been detected at the end-effector, the goal of the controller is to keep it stabilizing the system. On the other hand, if an unexpected collision occurred, the robot should move away from the obstacle and reach a safe configuration and position. The former situation has been studied since the pioneering works on floating space robots, and different controllers have been proposed. In this work, the latter situation is considered since it is deemed to be an important building block for autonomous and safe robotic operations near other objects. Recalling the examples of the manipulator impacting a non-recognized appendage of an uncooperative and unknown target or an erroneous end-effector path planning due to inaccurate estimation of the position and velocity of a grasping point, all these situations may lead to unplanned contacts that would jeopardize the system. Consequently, a proper action in response to these unforeseen occurrences should be designed, otherwise the robot would continue to pursue its original objective pushing against the obstacle and risking to worsen the situation. Indeed, multiple contacts and instability can arise causing irreparable damages. To this aim, a coordinated

base-joints control strategy is developed to mitigate the consequences of unintentional collisions between the space robot and another object in the proximity. Its effectiveness is shown through a simulation example, considering a 7DoF manipulator mounted on a 6DoF moving base actuated by thrusters and variable speed control moment gyros (VSCMG). Moreover, it is demonstrated that the controlled system is input-to-state stable, i.e., the error is bounded even during the contact, which is of paramount importance for system safety.

6.1 Reaction control strategy

In the proposed reaction strategy, the translational degrees of freedom and manipulator's joints are controlled in order to escape from the bumped obstacle, while the spacecraft attitude is commanded to keep a certain orientation. A prescribed attitude may be necessary either to communicate information, or to keep a possible target in the field of view of the sensors, or to rotate in order to see what caused the collision.
Consider the dynamics model (2.24). Introducing the velocity of the center of mass of the whole system in the inertial frame, denoted by $\boldsymbol{v}_{c,t} \in \mathbb{R}^3$, the following transformation, through the matrix $\boldsymbol{\Gamma}_c \in \mathbb{R}^{(6+n)\times(6+n)}$, can be defined:

$$\begin{bmatrix} \boldsymbol{v}_{c,t} \\ \boldsymbol{\omega}_b \\ \dot{\boldsymbol{q}} \end{bmatrix} = \underbrace{\begin{bmatrix} \boldsymbol{R}_{tb} & -\boldsymbol{R}_{tb}[\boldsymbol{p}_{bc}]^\times & \boldsymbol{R}_{tb}\bar{\boldsymbol{J}}_v \\ \boldsymbol{0} & \boldsymbol{E} & \boldsymbol{0} \\ \boldsymbol{0} & \boldsymbol{0} & \boldsymbol{E} \end{bmatrix}}_{\boldsymbol{\Gamma}_c} \begin{bmatrix} \boldsymbol{v}_b \\ \boldsymbol{\omega}_b \\ \dot{\boldsymbol{q}} \end{bmatrix}. \tag{6.1}$$

Consequently, the generalized forces transform as

$$\begin{bmatrix} \boldsymbol{f}_b \\ \boldsymbol{m}_b \\ \boldsymbol{\tau} \end{bmatrix} = \boldsymbol{\Gamma}_c^T \begin{bmatrix} \boldsymbol{f}_{c,t} \\ \boldsymbol{m}_c \\ \bar{\boldsymbol{\tau}}^* \end{bmatrix}, \tag{6.2}$$

$$\begin{bmatrix} \boldsymbol{f}_{ext,b} \\ \boldsymbol{m}_{ext,b} \\ \boldsymbol{\tau}_{ext} \end{bmatrix} = \boldsymbol{\Gamma}_c^T \begin{bmatrix} \boldsymbol{f}_{ext,c,t} \\ \boldsymbol{m}_{ext,c} \\ \bar{\boldsymbol{\tau}}^*_{ext} \end{bmatrix}, \tag{6.3}$$

where $\boldsymbol{f}_{c,t} \in \mathbb{R}^3$, $\boldsymbol{m}_c \in \mathbb{R}^3$, and $\bar{\boldsymbol{\tau}}^* \in \mathbb{R}^n$ are new control inputs; $\boldsymbol{f}_{ext,c,t} \in \mathbb{R}^3$, $\boldsymbol{m}_{ext,c} \in \mathbb{R}^3$, and $\bar{\boldsymbol{\tau}}^*_{ext} \in \mathbb{R}^n$ are the projections of the external wrench $\boldsymbol{\mathcal{F}}_{ext}$ into the new variables space. Note that the new generalized forces are related to the ones reported in Eqs. (5.9)-(5.10). Indeed, $\boldsymbol{f}_{c,t} = \boldsymbol{R}_{tc}\boldsymbol{f}_c$, $\boldsymbol{m}_c = \boldsymbol{I}_c\boldsymbol{a}_c$, and $\bar{\boldsymbol{\tau}}^* = \bar{\boldsymbol{\tau}} + \bar{\boldsymbol{J}}_\omega^T\boldsymbol{m}_c$. Similar relations can be written for the

external generalized forces.
Then, the dynamics in the new generalized velocities is derived pre-multiplying (2.24) by $\boldsymbol{\Gamma}_c^{-T}$ and substituting $\boldsymbol{v}_b$, $\boldsymbol{\omega}_b$, $\dot{\boldsymbol{q}}$ and their derivatives isolated from Eq. (6.1) in (2.24). The resulting system is

$$\begin{aligned}
&\begin{bmatrix} m\boldsymbol{E} & \mathbf{0} & \mathbf{0} \\ \mathbf{0} & \boldsymbol{I}_c & \boldsymbol{I}_c\bar{\boldsymbol{J}}_\omega \\ \mathbf{0} & \bar{\boldsymbol{J}}_\omega^T\boldsymbol{I}_c^T & \tilde{\boldsymbol{M}}_m \end{bmatrix} \begin{bmatrix} \dot{\boldsymbol{v}}_{c,t} \\ \dot{\boldsymbol{\omega}}_b \\ \ddot{\boldsymbol{q}} \end{bmatrix} + \\
&+ \begin{bmatrix} \mathbf{0} & \tilde{\boldsymbol{C}}_{cr} & \tilde{\boldsymbol{C}}_{cm} \\ -\tilde{\boldsymbol{C}}_{cr}^T & \tilde{\boldsymbol{C}}_r & \tilde{\boldsymbol{C}}_{rm} \\ -\tilde{\boldsymbol{C}}_{cm}^T & \tilde{\boldsymbol{C}}_{mr}^T & \tilde{\boldsymbol{C}}_m \end{bmatrix} \begin{bmatrix} \boldsymbol{v}_{c,t} \\ \boldsymbol{\omega}_b \\ \dot{\boldsymbol{q}} \end{bmatrix} = \begin{bmatrix} \boldsymbol{f}_{c,t} \\ \boldsymbol{m}_c \\ \bar{\boldsymbol{\tau}}^* \end{bmatrix} + \begin{bmatrix} \boldsymbol{f}_{ext,c,t} \\ \boldsymbol{m}_{ext,c} \\ \bar{\boldsymbol{\tau}}_{ext}^* \end{bmatrix}.
\end{aligned} \tag{6.4}$$

It can be proven (see Appendix) that $\tilde{\boldsymbol{C}}_{cr}\boldsymbol{\omega}_b + \tilde{\boldsymbol{C}}_{cm}\dot{\boldsymbol{q}} = \mathbf{0}$ and

$$\begin{aligned}
-\tilde{\boldsymbol{C}}_{cr}^T\boldsymbol{v}_{c,t} + \tilde{\boldsymbol{C}}_r\boldsymbol{\omega}_b + \tilde{\boldsymbol{C}}_{rm}\dot{\boldsymbol{q}} &= \underbrace{(\dot{\boldsymbol{I}}_c + [\boldsymbol{\omega}_b]^\times\boldsymbol{I}_c)}_{\boldsymbol{C}_{bq,r}}\boldsymbol{\omega}_b + \\
&+ \underbrace{(\dot{\boldsymbol{I}}_c\bar{\boldsymbol{J}}_\omega + \boldsymbol{I}_c\dot{\bar{\boldsymbol{J}}}_\omega + [\boldsymbol{\omega}_b]^\times\boldsymbol{I}_c\bar{\boldsymbol{J}}_\omega)}_{\boldsymbol{C}_{bq,rm}}\dot{\boldsymbol{q}}, \qquad (6.5a) \\
-\tilde{\boldsymbol{C}}_{cm}^T\boldsymbol{v}_{c,t} + \tilde{\boldsymbol{C}}_{mr}^T\boldsymbol{\omega}_b + \tilde{\boldsymbol{C}}_m\dot{\boldsymbol{q}} &= \underbrace{(\dot{\tilde{\boldsymbol{M}}}_m - \frac{1}{2}\tilde{\boldsymbol{M}}_{rm/q} - \frac{1}{2}\tilde{\boldsymbol{M}}_{m/q})}_{\boldsymbol{C}_{bq,m}}\dot{\boldsymbol{q}} + \\
&+ \underbrace{(\dot{\bar{\boldsymbol{J}}}_\omega^T\boldsymbol{I}_c^T + \bar{\boldsymbol{J}}_\omega^T\dot{\boldsymbol{I}}_c^T + \frac{1}{2}\boldsymbol{I}_{c/q}^{-T}\boldsymbol{I}_c - \frac{1}{2}\bar{\boldsymbol{J}}_{\omega/q}^T\boldsymbol{I}_c^T)}_{\boldsymbol{C}_{bq,mr}}\boldsymbol{\omega}_b, \qquad (6.5b)
\end{aligned}$$

where $\boldsymbol{I}_{c/q}^{-T}$, and $\bar{\boldsymbol{J}}_{\omega/q}^T$ are defined in Eqs. (5.14)-(5.15)-(5.16), and

$$\tilde{\boldsymbol{M}}_{rm/q} = \begin{bmatrix} \boldsymbol{\omega}_b^T\frac{\partial(\boldsymbol{I}_c\bar{\boldsymbol{J}}_\omega)}{\partial q_1} \\ \vdots \\ \boldsymbol{\omega}_b^T\frac{\partial(\boldsymbol{I}_c\bar{\boldsymbol{J}}_\omega)}{\partial q_n} \end{bmatrix}, \quad \tilde{\boldsymbol{M}}_{m/q} = \begin{bmatrix} \dot{\boldsymbol{q}}^T\frac{\partial\tilde{\boldsymbol{M}}_m^*}{\partial q_1} \\ \vdots \\ \dot{\boldsymbol{q}}^T\frac{\partial\tilde{\boldsymbol{M}}_m^*}{\partial q_n} \end{bmatrix} \in \mathbb{R}^{n\times n}. \tag{6.6}$$

It is recalled that $\boldsymbol{I}_{c/q}^{-T}$ and $\bar{\boldsymbol{J}}_{\omega/q}^T$ are function of $\boldsymbol{q}$, and $\tilde{\boldsymbol{M}}_{rm/q}$ and $\tilde{\boldsymbol{M}}_{m/q}$ as well, while $\dot{\bar{\boldsymbol{J}}}_\omega$ and $\dot{\boldsymbol{I}}_c$ are function of $\boldsymbol{q}$ and $\dot{\boldsymbol{q}}$.
Therefore, the translational dynamics is completely decoupled from the ro-

tational and joints dynamics:

$$m\dot{\boldsymbol{v}}_{c,t} = \boldsymbol{f}_{c,t} + \boldsymbol{f}_{ext,c,t}, \tag{6.7a}$$

$$\boldsymbol{M}_{bq}\dot{\breve{\boldsymbol{\omega}}} + \boldsymbol{C}_{bq}\breve{\boldsymbol{\omega}} = \boldsymbol{m}^* + \boldsymbol{m}^*_{ext} \tag{6.7b}$$

where $\breve{\boldsymbol{\omega}} = [\boldsymbol{\omega}_b^T \;\; \dot{\boldsymbol{q}}^T]^T \in \mathbb{R}^{3+n}$, $\boldsymbol{m}^* = [\boldsymbol{m}_c^T \;\; \bar{\boldsymbol{\tau}}^{*T}]^T \in \mathbb{R}^{3+n}$, $\boldsymbol{m}^*_{ext} = [\boldsymbol{m}^T_{ext,c} \; \bar{\boldsymbol{\tau}}^{*T}_{ext}]^T \in \mathbb{R}^{3+n}$, and

$$\boldsymbol{M}_{bq}(\boldsymbol{q}) = \begin{bmatrix} \boldsymbol{I}_c & \boldsymbol{I}_c\bar{\boldsymbol{J}}_\omega \\ \bar{\boldsymbol{J}}_\omega^T\boldsymbol{I}_c^T & \tilde{\boldsymbol{M}}_m \end{bmatrix} \in \mathbb{R}^{(3+n)\times(3+n)}, \tag{6.8}$$

$$\boldsymbol{C}_{bq}(\boldsymbol{q}, \dot{\boldsymbol{q}}, \boldsymbol{\omega}_b) = \begin{bmatrix} \boldsymbol{C}_{bq,r} & \boldsymbol{C}_{bq,rm} \\ \boldsymbol{C}_{bq,mr} & \boldsymbol{C}_{bq,m} \end{bmatrix} \in \mathbb{R}^{(3+n)\times(3+n)}, \tag{6.9}$$

Note that, for the dynamics (6.7b), the property $\breve{\boldsymbol{\omega}}^T(\dot{\boldsymbol{M}}_{bq} - 2\boldsymbol{C}_{bq})\breve{\boldsymbol{\omega}} = 0$ is valid (see the Appendix for the demonstration).

A compliant controller is implemented for the reaction to collision exploiting the new control inputs as follows

$$\boldsymbol{f}_{c,t} = -\boldsymbol{K}_c\tilde{\boldsymbol{x}}_{c,t} - \boldsymbol{D}_c\boldsymbol{v}_{c,t} \tag{6.10}$$

$$\boldsymbol{m}^* = -\boldsymbol{J}_{\tilde{\phi}}^T\boldsymbol{K}_{bq}\tilde{\boldsymbol{\phi}} - \boldsymbol{D}_{bq}\breve{\boldsymbol{\omega}} \tag{6.11}$$

where $\tilde{\boldsymbol{x}}_{c,t} \in \mathbb{R}^3$ is the error on the position of the center of mass of the whole system, $\tilde{\boldsymbol{\phi}}^T = [2\tilde{\boldsymbol{\epsilon}}^T \;\; \tilde{\boldsymbol{q}}^T]^T \in \mathbb{R}^{3+n}$, with $\tilde{\boldsymbol{\epsilon}} \in \mathbb{R}^3$ being the vector part of the quaternion error extracted from $\boldsymbol{R}_{bb_d} = \boldsymbol{R}_{tb}^T\boldsymbol{R}_{tb_d}$, and $\tilde{\boldsymbol{q}} \in \mathbb{R}^n$ is the error on the joint angles. The rotation matrix $\boldsymbol{R}_{tb_d}$ is the desired one. The matrices $\boldsymbol{K}_c, \boldsymbol{D}_c, \boldsymbol{K}_{bq}, \boldsymbol{D}_{bq}$ are diagonal positive definite matrices of appropriate dimensions. Finally, $\boldsymbol{J}_{\tilde{\phi}}$ is defined as follows:

$$\dot{\tilde{\boldsymbol{\phi}}} = \boldsymbol{J}_{\tilde{\phi}}\breve{\boldsymbol{\omega}} \tag{6.12}$$

where

$$\boldsymbol{J}_{\tilde{\phi}} = \begin{bmatrix} (\tilde{\eta}\boldsymbol{E} - [\boldsymbol{\epsilon}]^\times) & \boldsymbol{0} \\ \boldsymbol{0} & \boldsymbol{E} \end{bmatrix} \in \mathbb{R}^{(3+n)\times(3+n)}. \tag{6.13}$$

and where $\tilde{\eta} \in \mathbb{R}$ is the scalar part of the quaternion error.
As already explained, the spacecraft is commanded to keep a desired attitute, while the manipulator is moving and the entire robot is translating

away from the obstacle. To this aim, the desired position of the center of mass $\boldsymbol{x}_{c,t,d}$ and of the joints $\boldsymbol{q}_d$ are defined as follows:

$$\boldsymbol{x}_{c,t,d} = \boldsymbol{x}_{c,t,td} + \Delta_{x_c} \frac{\hat{\boldsymbol{f}}_{ext,c,t}}{|\hat{\boldsymbol{f}}_{ext,c,t}|} \tag{6.14}$$

$$\boldsymbol{q}_d = \boldsymbol{q}_{td} + \Delta_q \frac{\hat{\bar{\boldsymbol{\tau}}}^*_{ext}}{|\hat{\bar{\boldsymbol{\tau}}}^*_{ext}|} \tag{6.15}$$

where $\boldsymbol{x}_{c,t,td}, \boldsymbol{q}_{td}$ are the positions at the detected contact time, $\hat{\boldsymbol{f}}_{ext,c,t}, \hat{\bar{\boldsymbol{\tau}}}^*_{ext}$ are the estimates of effects of the external contact force on the CM position and the joints, respectively, and Δ_{x_c}, Δ_q are some desired "bounce" coefficients. Thanks to the second term in both Eqs. (6.14) and (6.15), the robot is commanded to move along the direction of the external contact force, projected in the frame $\mathcal{CT}$ and in the joints space, and thus following the motion imposed by the force and moving away from the obstacle.
In order to compute $\hat{\boldsymbol{f}}_{ext,c,t}$ and $\hat{\bar{\boldsymbol{\tau}}}^*_{ext}$, it is possible to exploit the residuals introduced in the previous chapter in Eq. (5.18) as follows:

$$\hat{\boldsymbol{f}}_{ext,c,t} = \boldsymbol{R}_{tc} \hat{\boldsymbol{f}}_{ext,c}, \tag{6.16}$$

$$\hat{\bar{\boldsymbol{\tau}}}^*_{ext} = \hat{\bar{\boldsymbol{\tau}}}_{ext} + \bar{\boldsymbol{J}}^T_{\omega} \hat{\boldsymbol{m}}_{ext,c}. \tag{6.17}$$

Actually, it has been already shown that the estimation of $\boldsymbol{f}_{ext,c}$ is particularly affected by noise and uncertainties in the system. Therefore, it could be more convenient to use the force component of the reconstructed wrench obtained through Eq. (5.23), namely the force reconstructed by the angular and joints momentum residuals. Alternatively, a new observer, slightly different from (5.18), can be derived based on the dynamics model (6.7). This alternative scheme is presented in the following section.

6.2 Modified observer including momentum exchange devices

A new observer can be derived defining three residuals based on the dynamics (6.7). Moreover, since in this study the spacecraft is assumed to be actuated by variable speed control moment gyros, the effects of generic momentum exchange devices (MED) can be included.
Consider a reference frame attached to each MED defined by the following three versors:

- $\hat{\boldsymbol{n}}_s$ is the spin axis, along the rotation axis of the wheel;

- $\hat{\boldsymbol{n}}_t$ is the axis that completes the frame $\{\hat{\boldsymbol{n}}_s, \hat{\boldsymbol{n}}_t, \hat{\boldsymbol{n}}_g\}$
- $\hat{\boldsymbol{n}}_g$ is the gimbal axis, along the rotation axis of the gimbal.

The equations of motion for a spacecraft with a cluster of k MED have been developed in [80], and the angular momentum of the spacecraft-MED ensemble, expressed in $\mathcal{B}$, is

$$\boldsymbol{h}^r_{b,med} = \boldsymbol{I}_{b+med}\boldsymbol{\omega}_b + \boldsymbol{A}_g\boldsymbol{I}_{cg}\dot{\boldsymbol{\gamma}} + \boldsymbol{A}_s\boldsymbol{I}_{ws}\boldsymbol{\omega}_w, \tag{6.18}$$

where $\boldsymbol{A}_\star \in \mathbb{R}^{3\times k}$ is a matrix having as columns the directions of the spin, transverse and gimbal directional unit vectors expressed in the frame $\mathcal{B}$, $\boldsymbol{I}_{c\star},\ \boldsymbol{I}_{w\star} \in \mathbb{R}^{k\times k}$ are diagonal matrices having as elements the inertias of the gimbal-wheel structure ($\boldsymbol{I}_{c\star} = \boldsymbol{I}_{g\star} + \boldsymbol{I}_{w\star}$, with $\boldsymbol{I}_{g\star}$ being the inertia of the gimbal) and only-wheel structure, respectively, $\dot{\boldsymbol{\gamma}} \in \mathbb{R}^k$ is the vector of the gimbal angular velocities, expressed in the MED frame, $\boldsymbol{\omega}_w \in \mathbb{R}^k$ is the vector of the wheel angular velocities, expressed in the MED frame, and $\boldsymbol{I}_{b+med} \in \mathbb{R}^{3\times3}$ is defined as

$$\boldsymbol{I}_{b+med} = \boldsymbol{I}_b + \boldsymbol{A}_s\boldsymbol{I}_{cs}\boldsymbol{A}_s^T + \boldsymbol{A}_t\boldsymbol{I}_{ct}\boldsymbol{A}_t^T + \boldsymbol{A}_g\boldsymbol{I}_{cg}\boldsymbol{A}_g^T, \tag{6.19}$$

where $\boldsymbol{I}_b \in \mathbb{R}^{3\times3}$ is the inertia matrix of the spacecraft including the point masses of the MED.
Based on (6.7) and (6.18), the residuals $\hat{\boldsymbol{f}}_{ext,c,t}$, $\hat{\boldsymbol{m}}_{ext,c}$ and $\hat{\bar{\boldsymbol{\tau}}}^*_{ext}$ can be defined as the difference between the real momentum and the estimated one:

$$\hat{\boldsymbol{f}}_{ext,c,t} = \boldsymbol{K}_f(m\boldsymbol{v}_{c,t} - \int_0^t (\boldsymbol{f}_{c,t} + \hat{\boldsymbol{f}}_{ext,c,t})ds), \tag{6.20a}$$

$$\hat{\boldsymbol{m}}_{ext,c} = \boldsymbol{K}_m(\boldsymbol{h}^r_c + \boldsymbol{A}_g\boldsymbol{I}_{cg}\dot{\boldsymbol{\gamma}} + \boldsymbol{A}_s\boldsymbol{I}_{ws}\boldsymbol{\omega}_w - \int_0^t (-[\boldsymbol{p}_{bc}]^\times \boldsymbol{f}_b + \\ - [\boldsymbol{\omega}_b]^\times (\boldsymbol{h}^r_c + \boldsymbol{A}_g\boldsymbol{I}_{cg}\dot{\boldsymbol{\gamma}} + \boldsymbol{A}_s\boldsymbol{I}_{ws}\boldsymbol{\omega}_w) + \hat{\boldsymbol{m}}_{ext,c})ds), \tag{6.20b}$$

$$\hat{\bar{\boldsymbol{\tau}}}^*_{ext} = \boldsymbol{K}_\tau(\tilde{\boldsymbol{M}}_m\dot{\boldsymbol{q}} + \bar{\boldsymbol{J}}_w^T\boldsymbol{I}_c^T\boldsymbol{\omega}_b - \int_0^t (\bar{\boldsymbol{\tau}}^* + \frac{1}{2}(\tilde{\boldsymbol{M}}_{m/q} + \tilde{\boldsymbol{M}}_{rm/q})\dot{\boldsymbol{q}} + \\ + \frac{1}{2}(-\boldsymbol{I}_{c/q}^{-T}\boldsymbol{I}_c + \bar{\boldsymbol{J}}^T_{\omega/q}\boldsymbol{I}_c)\boldsymbol{\omega}_b + \hat{\bar{\boldsymbol{\tau}}}^*_{ext})ds), \tag{6.20c}$$

Note that $\boldsymbol{h}_c^r$ is computed here considering the presence of the momentum exchange devices.
As already explained in Sects. 5.2-5.3, the residuals $\hat{\boldsymbol{f}}_{ext,c,t}$,$\hat{\boldsymbol{m}}_{ext,c}$, and $\hat{\bar{\boldsymbol{\tau}}}^*_{ext}$, defined in this way, are the first-order-filtered estimations of $\boldsymbol{f}_{ext,c,t}$, $\boldsymbol{m}_{ext,c}$, and $\bar{\boldsymbol{\tau}}^*_{ext}$, respectively.
Also in this case, it is better, from practical point of view, to estimate the contact force relying only on the residuals $\hat{\boldsymbol{m}}_{ext,c}$ and $\hat{\bar{\boldsymbol{\tau}}}^*_{ext}$, for the same reasons reported in the previous chapter. The wrench reconstruction can be performed as follows:

$$\hat{\boldsymbol{\mathcal{F}}}_{ext} = \left(\begin{bmatrix} [\boldsymbol{p}_{cp}]^\times \boldsymbol{R}_{pb}^T & \boldsymbol{R}_{pb}^T \\ \boldsymbol{J}_{vp}^{\star T} & \boldsymbol{J}_{\omega w}^T \end{bmatrix} \right)^{\#} \begin{bmatrix} \hat{\boldsymbol{m}}_{ext,c} \\ \hat{\bar{\boldsymbol{\tau}}}^*_{ext} \end{bmatrix}, \tag{6.21}$$

where

$$\boldsymbol{J}^\star_{vp} = -\boldsymbol{R}_{pb}\bar{\boldsymbol{J}}_v + \boldsymbol{J}_{vp} \in \mathbb{R}^{3\times n}, \tag{6.22}$$

To conclude, note that Eq. (6.20b) is valid for any momentum exchange devices. Indeed, if the reaction wheels are selected, it is sufficient to set $\dot{\boldsymbol{\gamma}} = \boldsymbol{0}$; if the control moment gyros are chosen, $\boldsymbol{\omega}_w$ will be constant; finally, if the VSCMG are preferred, as in this study, both $\dot{\boldsymbol{\gamma}}$ and $\boldsymbol{\omega}_w$ can vary in time.

6.3 Discussion on the proposed control strategy

With the proposed controller, the space robot system is like split into an "external" translational motion of the entire composite body and an "internal" rotational motion modifying the configuration. The linear control actions are used only to move the center of mass of the whole system, but they are compensated at the attitude and joint level thanks to the triangular form of the equation (6.2). This can be seen imaging to impose a change in the position of the CM, keeping the attitude and joints position. The control actions $\boldsymbol{m}_c$ and $\bar{\boldsymbol{\tau}}^*$ are zero, while $\boldsymbol{f}_{ext,c,t}$ is not. When the computed control actions are transformed in the real ones provided by the actuators through Eq. (6.2), all the actuators are activated. In particular, the thrusters are used to translate the CM of the whole system, while the momentum exchange devices and the joint motors are used to keep the position compensating the disturbance caused by the thrusters.
This controller has been developed only to address the reaction to an unexpected collision. However, it could be used to the perform the required tasks, such as grasping a target. In this case, note that the translational

control is activated only when an external contact occurs, modifying the position of the CM, while in the contact-free phase only attitude and joints position are controlled. This means that the use of the thrusters can be completely avoided, in case the attitude is controlled only through momentum exchange devices, or in general can be limited, until a contact occurs, saving fuel. However, for the nominal operations, it would be better to control the manipulator in the operational space, instead of the joints space. To this aim, a controller similar to the one presented in this thesis was proposed recently in [75], which is based on this transformation:

$$\begin{bmatrix} \boldsymbol{v}_{c,t} \\ \boldsymbol{\omega}_b \\ \boldsymbol{\nu}_e^{\oplus} \end{bmatrix} = \begin{bmatrix} \boldsymbol{R}_{tb} & -\boldsymbol{R}_{tb}[\boldsymbol{p}_{bc}]^{\times} & \boldsymbol{R}_{tb}\bar{\boldsymbol{J}}_v \\ \boldsymbol{0} & \boldsymbol{E} & \boldsymbol{0} \\ \boldsymbol{0} & \boldsymbol{G}_{\omega_b} & \boldsymbol{J}_{\nu_e}^{\oplus} \end{bmatrix} \begin{bmatrix} \boldsymbol{v}_b \\ \boldsymbol{\omega}_b \\ \dot{\boldsymbol{q}} \end{bmatrix}, \tag{6.23}$$

where $\boldsymbol{\nu}_e^{\oplus} \in \mathbb{R}^6$ is called "end-effector circumcentroidal motion", i.e., the motion around the CM, $\boldsymbol{G}_{\omega_b} \in \mathbb{R}^{6\times 3}$ and $\boldsymbol{J}_{\nu_e}^{\oplus} \in \mathbb{R}^{6\times n}$ are matrices mapping the angular velocity of the spacecraft and the joints in the circumcentroidal motion. The vector $\boldsymbol{\nu}_e^{\oplus}$ is exactly equal to the vector containing the linear and angular velocity of the end-effector when the velocity of the CM of the whole system is zero. More detail about this controller can be found in [75].

The main difference between the strategy in [75] and the one proposed here is exactly the control of the manipulator that in [75] is controlled in the end-effector space. Note that these two controllers can actually work together since they address two different objectives. The space robot can be controlled by the strategy in [75] during the nominal operations, which require end-effector maneuvering. When an unexpected collision occurs, the robot switches to the control proposed in this thesis, limiting the possible damages. For the reaction phase, it is better to control the system in the joints space since the manipulator can be controlled without taking care of possible singular configurations or degrees of freedom in the end-effector's null space (in case of redundant arm). Indeed, the goal of the reaction phase is to move the robot safely and quickly in a configuration and position away from the obstacle, and this can be achieved efficiently by the proposed controller. Moreover, the information from the observer is in the joints space and provides directly a direction to follow in order to escape from the contact.

The integration of these two controllers leads to a control system capable of operating in both nominal and emergency conditions, such as an unexpected collision, and saving fuel in contact-free end-effector maneuvering.

Finally, note that the switch between the controllers is only at the manipulator level. In the simulation example at the end of the chapter, the performance of the proposed controller is assessed imaging a scenario in which a nominal operation is performed using the controller in [75] and at a certain time the robot switches the control to face an unplanned collision.

6.4 Input-to-state stability of the controlled system

All the defintions and theorems used to demonstrate the input-to-state stability (ISS) of the controlled system are reported in Chapter 2.

Consider the dynamics model (6.7b) and the control action (6.11). The controlled system is

$$\boldsymbol{M}_{bq}\dot{\breve{\boldsymbol{\omega}}} + (\boldsymbol{C}_{bq} + \boldsymbol{D}_{bq})\breve{\boldsymbol{\omega}} + \boldsymbol{J}_{\tilde{\phi}}^{T}\boldsymbol{K}_{bq}\tilde{\boldsymbol{\phi}} = \boldsymbol{m}_{ext}^{*} \tag{6.24}$$

According to the Theorem 1, in order to prove the input-to-state stability, it is necessary to show that the dynamic system (6.24) admits a quasi ISS-Lyapunov (qISS-Lyapunov) function and an Input-Output-to-State-Stable Lyapunov (IOSS-Lyapunov) function. Note that the setpoints after the contact are considered constant.
Consider the following function as candidate Lyapunov function:

$$V_{r1} = \frac{1}{2}\breve{\boldsymbol{\omega}}^{T}\boldsymbol{M}_{bq}\breve{\boldsymbol{\omega}} + \frac{1}{2}\tilde{\boldsymbol{\phi}}^{T}\boldsymbol{K}_{bq}\tilde{\boldsymbol{\phi}} \tag{6.25}$$

The time derivative of V_{r1} is

$$\begin{aligned}
\dot{V}_{r1} &= \breve{\boldsymbol{\omega}}^{T}\boldsymbol{M}_{bq}\dot{\breve{\boldsymbol{\omega}}} + \breve{\boldsymbol{\omega}}^{T}\boldsymbol{J}_{\tilde{\phi}}^{T}\boldsymbol{K}_{bq}\tilde{\boldsymbol{\phi}} + \frac{1}{2}\breve{\boldsymbol{\omega}}^{T}\dot{\boldsymbol{M}}_{bq}\breve{\boldsymbol{\omega}} = \\
&= -\breve{\boldsymbol{\omega}}^{T}\boldsymbol{D}_{bq}\breve{\boldsymbol{\omega}} + \breve{\boldsymbol{\omega}}^{T}\boldsymbol{m}_{ext}^{*} + \frac{1}{2}\breve{\boldsymbol{\omega}}^{T}(\dot{\boldsymbol{M}}_{bq} - 2\boldsymbol{C}_{bq})\breve{\boldsymbol{\omega}} = \\
&= -\breve{\boldsymbol{\omega}}^{T}\boldsymbol{D}_{bq}\breve{\boldsymbol{\omega}} + \breve{\boldsymbol{\omega}}^{T}\boldsymbol{m}_{ext}^{*} \leq -c_{r1}|\breve{\boldsymbol{\omega}}|^{2} + c_{r2}|\boldsymbol{m}_{ext}^{*}|^{2} = \\
&= -\bar{\gamma}_{r}(|\breve{\boldsymbol{\omega}}|) + \sigma_{r1}(|\boldsymbol{m}_{ext}^{*}|)
\end{aligned} \tag{6.26}$$

where $c_{r1}, c_{r2} = \text{const.} > 0$. In the computation of the derivative, the relations (6.12)-(6.24) and the property $\breve{\boldsymbol{\omega}}^{T}(\dot{\boldsymbol{M}}_{bq} - 2\boldsymbol{C}_{bq})\breve{\boldsymbol{\omega}} = 0$ have been used. For the inequality, note that for all $v, w \in \mathbb{R}$ the inequality $2vw \leq \frac{1}{k}v^{2} + kw^{2}$ is valid, with $k > 0$.
From this result, recalling Definition 1 and Definition 4 and considering $\boldsymbol{y} = \breve{\boldsymbol{\omega}}$, it is possible to say that the system is passive w.r.t. the pair $(\breve{\boldsymbol{\omega}}, \boldsymbol{m}_{ext}^{*})$ and admits a qISS-Lyapunov function.

Another candidate Lyapunov function can be defined slightly modifying V_{r1}:

$$V_{r2} = \frac{1}{2}\breve{\boldsymbol{\omega}}^T \boldsymbol{M}_{bq}\breve{\boldsymbol{\omega}} + \frac{1}{2}\tilde{\boldsymbol{\phi}}^T \boldsymbol{K}_{bq}\tilde{\boldsymbol{\phi}} + \epsilon\frac{\tilde{\boldsymbol{\phi}}^T \boldsymbol{M}_{bq}\breve{\boldsymbol{\omega}}}{\sqrt{1+\tilde{\boldsymbol{\phi}}^T\tilde{\boldsymbol{\phi}}}} \tag{6.27}$$

with $\epsilon = \text{const.} > 0$ sufficiently small.
The time derivative of V_{r2} is

$$\begin{aligned}
\dot{V}_{r2} =& \breve{\boldsymbol{\omega}}^T \boldsymbol{M}_{bq}\dot{\breve{\boldsymbol{\omega}}} + \breve{\boldsymbol{\omega}}^T \boldsymbol{J}_{\tilde{\phi}}^T \boldsymbol{K}_{bq}\tilde{\boldsymbol{\phi}} + \frac{1}{2}\breve{\boldsymbol{\omega}}^T \dot{\boldsymbol{M}}_{bq}\breve{\boldsymbol{\omega}} + \epsilon\frac{\breve{\boldsymbol{\omega}}^T \boldsymbol{J}_{\tilde{\phi}}^T \boldsymbol{M}_{bq}\breve{\boldsymbol{\omega}}}{\sqrt{1+\tilde{\boldsymbol{\phi}}^T\tilde{\boldsymbol{\phi}}}} + \\
&+ \epsilon\frac{\tilde{\boldsymbol{\phi}}^T \dot{\boldsymbol{M}}_{bq}\breve{\boldsymbol{\omega}}}{\sqrt{1+\tilde{\boldsymbol{\phi}}^T\tilde{\boldsymbol{\phi}}}} + \epsilon\frac{\tilde{\boldsymbol{\phi}}^T \boldsymbol{M}_{bq}\dot{\breve{\boldsymbol{\omega}}}}{\sqrt{1+\tilde{\boldsymbol{\phi}}^T\tilde{\boldsymbol{\phi}}}} - \epsilon\frac{(\tilde{\boldsymbol{\phi}}^T \boldsymbol{J}_{\tilde{\phi}}\breve{\boldsymbol{\omega}})(\tilde{\boldsymbol{\phi}}^T \boldsymbol{M}_{bq}\breve{\boldsymbol{\omega}})}{(1+\tilde{\boldsymbol{\phi}}^T\tilde{\boldsymbol{\phi}})^{\frac{3}{2}}} = \\
=& -\breve{\boldsymbol{\omega}}^T \boldsymbol{D}_{bq}\breve{\boldsymbol{\omega}} - \epsilon\frac{\tilde{\boldsymbol{\phi}}^T \boldsymbol{J}_{\tilde{\phi}}^T \boldsymbol{K}_{bq}\tilde{\boldsymbol{\phi}}}{\sqrt{1+\tilde{\boldsymbol{\phi}}^T\tilde{\boldsymbol{\phi}}}} + \epsilon\frac{\breve{\boldsymbol{\omega}}^T \boldsymbol{J}_{\tilde{\phi}}^T \boldsymbol{M}_{bq}\breve{\boldsymbol{\omega}}}{\sqrt{1+\tilde{\boldsymbol{\phi}}^T\tilde{\boldsymbol{\phi}}}} + \\
&+ \epsilon\frac{\tilde{\boldsymbol{\phi}}^T(\dot{\boldsymbol{M}}_{bq} - \boldsymbol{C}_{bq})\breve{\boldsymbol{\omega}}}{\sqrt{1+\tilde{\boldsymbol{\phi}}^T\tilde{\boldsymbol{\phi}}}} - \epsilon\frac{\tilde{\boldsymbol{\phi}}^T \boldsymbol{D}_{bq}\breve{\boldsymbol{\omega}}}{\sqrt{1+\tilde{\boldsymbol{\phi}}^T\tilde{\boldsymbol{\phi}}}} + \epsilon\frac{\tilde{\boldsymbol{\phi}}^T \boldsymbol{m}^*_{ext}}{\sqrt{1+\tilde{\boldsymbol{\phi}}^T\tilde{\boldsymbol{\phi}}}} + \\
&- \epsilon\frac{(\tilde{\boldsymbol{\phi}}^T \boldsymbol{J}_{\tilde{\phi}}\breve{\boldsymbol{\omega}})(\tilde{\boldsymbol{\phi}}^T \boldsymbol{M}_{bq}\breve{\boldsymbol{\omega}})}{(1+\tilde{\boldsymbol{\phi}}^T\tilde{\boldsymbol{\phi}})^{\frac{3}{2}}} + \breve{\boldsymbol{\omega}}^T \boldsymbol{m}^*_{ext}
\end{aligned} \tag{6.28}$$

As previously, the equations (6.12)-(6.24) and the property $\breve{\boldsymbol{\omega}}^T(\dot{\boldsymbol{M}}_{bq} - 2\boldsymbol{C}_{bq})\breve{\boldsymbol{\omega}} = 0$ have been used in the derivation of (6.28).
Considering one term of (6.28) at the time, the following relations can be written:

$$\begin{aligned}
\tilde{\boldsymbol{\phi}}^T \boldsymbol{J}_{\tilde{\phi}}^T \boldsymbol{K}_{bq}\tilde{\boldsymbol{\phi}} &= \begin{bmatrix} 2\tilde{\boldsymbol{\epsilon}} & \tilde{\boldsymbol{q}} \end{bmatrix} \begin{bmatrix} (\tilde{\eta}\boldsymbol{E} + [\tilde{\boldsymbol{\epsilon}}]^\times) & \boldsymbol{0} \\ \boldsymbol{0} & \boldsymbol{E} \end{bmatrix} \begin{bmatrix} \boldsymbol{K}_{\tilde{\epsilon}} & \boldsymbol{0} \\ \boldsymbol{0} & \boldsymbol{K}_{\tilde{q}} \end{bmatrix} \begin{bmatrix} 2\tilde{\boldsymbol{\epsilon}} \\ \tilde{\boldsymbol{q}} \end{bmatrix} = \\
&= \begin{bmatrix} 2\tilde{\boldsymbol{\epsilon}} & \tilde{\boldsymbol{q}} \end{bmatrix} \begin{bmatrix} \tilde{\eta}\boldsymbol{K}_{\tilde{\epsilon}} & \boldsymbol{0} \\ \boldsymbol{0} & \boldsymbol{K}_{\tilde{q}} \end{bmatrix} \begin{bmatrix} 2\tilde{\boldsymbol{\epsilon}} \\ \tilde{\boldsymbol{q}} \end{bmatrix} = \tilde{\boldsymbol{\phi}}^T \tilde{\boldsymbol{K}}_{bq}\tilde{\boldsymbol{\phi}},
\end{aligned} \tag{6.29}$$

$$\epsilon\frac{\breve{\boldsymbol{\omega}}^T \boldsymbol{J}_{\tilde{\phi}}^T \boldsymbol{M}_{bq}\breve{\boldsymbol{\omega}}}{\sqrt{1+\tilde{\boldsymbol{\phi}}^T\tilde{\boldsymbol{\phi}}}} \leq \epsilon\frac{|\boldsymbol{J}_{\tilde{\phi}}^T||\boldsymbol{M}_{bq}||\breve{\boldsymbol{\omega}}|^2}{\sqrt{1+|\tilde{\boldsymbol{\phi}}|^2}} \leq \epsilon|\boldsymbol{J}_{\tilde{\phi}}^T||\boldsymbol{M}_{bq}||\breve{\boldsymbol{\omega}}|^2 \leq a_{r1}|\breve{\boldsymbol{\omega}}|^2, \tag{6.30}$$

$$\epsilon\frac{\tilde{\boldsymbol{\phi}}^T(\dot{\boldsymbol{M}}_{bq}-\boldsymbol{C}_{bq})\breve{\boldsymbol{\omega}}}{\sqrt{1+\tilde{\boldsymbol{\phi}}^T\tilde{\boldsymbol{\phi}}}} \leq \epsilon\frac{|\tilde{\boldsymbol{\phi}}|}{\sqrt{1+|\tilde{\boldsymbol{\phi}}|^2}}(|\dot{\boldsymbol{M}}_{bq}|+|\boldsymbol{C}_{bq}|)|\breve{\boldsymbol{\omega}}| \leq \epsilon(|\dot{\boldsymbol{M}}_{bq}|+|\boldsymbol{C}_{bq}|)|\breve{\boldsymbol{\omega}}| \leq a_{r2}|\breve{\boldsymbol{\omega}}|^2, \tag{6.31}$$

$$-\epsilon\frac{\tilde{\boldsymbol{\phi}}^T\boldsymbol{D}_{bq}\breve{\boldsymbol{\omega}}}{\sqrt{1+\tilde{\boldsymbol{\phi}}^T\tilde{\boldsymbol{\phi}}}} \leq \epsilon\frac{\lambda_{max}(\boldsymbol{D}_{eq})|\tilde{\boldsymbol{\phi}}||\breve{\boldsymbol{\omega}}|}{\sqrt{1+|\tilde{\boldsymbol{\phi}}|^2}} \leq \epsilon\lambda_{max}(\boldsymbol{D}_{eq})|\breve{\boldsymbol{\omega}}| \leq a_{r3}|\breve{\boldsymbol{\omega}}|, \tag{6.32}$$

$$-\epsilon\frac{(\tilde{\boldsymbol{\phi}}^T\boldsymbol{J}_{\tilde{\phi}}\breve{\boldsymbol{\omega}})(\tilde{\boldsymbol{\phi}}^T\boldsymbol{M}_{bq}\breve{\boldsymbol{\omega}})}{(1+\tilde{\boldsymbol{\phi}}^T\tilde{\boldsymbol{\phi}})^{\frac{3}{2}}} \leq \epsilon\frac{|\boldsymbol{J}_{\tilde{\phi}}||\boldsymbol{M}_{bq}||\tilde{\boldsymbol{\phi}}|^2|\breve{\boldsymbol{\omega}}|^2}{(1+|\tilde{\boldsymbol{\phi}}|^2)^{\frac{3}{2}}} \leq \epsilon|\boldsymbol{J}_{\tilde{\phi}}^T||\boldsymbol{M}_{bq}||\breve{\boldsymbol{\omega}}|^2 \leq a_{r1}|\breve{\boldsymbol{\omega}}|^2 \tag{6.33}$$

$$\breve{\boldsymbol{\omega}}^T\boldsymbol{m}_{ext}^* \leq |\breve{\boldsymbol{\omega}}||\boldsymbol{m}_{ext}^*| \leq c_{r3}|\breve{\boldsymbol{\omega}}|^2 + c_{r2}|\boldsymbol{m}_{ext}^*|^2 \tag{6.34}$$

$$\epsilon\frac{\tilde{\boldsymbol{\phi}}^T\boldsymbol{m}_{ext}^*}{\sqrt{1+\tilde{\boldsymbol{\phi}}^T\tilde{\boldsymbol{\phi}}}} \leq \epsilon\frac{|\tilde{\boldsymbol{\phi}}|}{\sqrt{1+|\tilde{\boldsymbol{\phi}}|^2}}|\boldsymbol{m}_{ext}^*| \leq \epsilon|\boldsymbol{m}_{ext}^*| \tag{6.35}$$

where $a_{r1}, a_{r2}, a_{r3}, c_{r3} = \text{const.} > 0$.
The previous inequalities are derived considering that:

- for all $v, w \in \mathbb{R}$, $2vw \leq \frac{1}{k}v^2 + kw^2$, with $k > 0$;
- only revolute joints are considered, and thus $\boldsymbol{M}_{bq}$ is a periodic function of $\boldsymbol{q}$. Therefore, $|\boldsymbol{M}_{bq}| \leq d_1$, $|\dot{\boldsymbol{M}}_{bq}| \leq d_2|\breve{\boldsymbol{\omega}}|$, $|\boldsymbol{C}_{bq}| \leq d_2|\breve{\boldsymbol{\omega}}|$, with $d_1, d_2, d_3 = \text{const.} > 0$;
- it is assumed that $0 < \tilde{\eta} \leq 1$;
- all the functions $\frac{|\tilde{\boldsymbol{\phi}}|}{\sqrt{1+|\tilde{\boldsymbol{\phi}}|^2}}$, $\frac{1}{\sqrt{1+|\tilde{\boldsymbol{\phi}}|^2}}$, $\frac{|\tilde{\boldsymbol{\phi}}|}{(1+|\tilde{\boldsymbol{\phi}}|^2)^{\frac{3}{2}}}$ are positive and bounded by 1.

Using Eqs. (6.29)-(6.35), it is possible to find an upper bound for the time derivative of V_{r2} as follows:

$$\begin{aligned}\dot{V}_{r2} \leq & -\breve{\boldsymbol{\omega}}^T \boldsymbol{D}_{bq} \breve{\boldsymbol{\omega}} - \epsilon \frac{\tilde{\boldsymbol{\phi}}^T \tilde{\boldsymbol{K}}_{bq} \tilde{\boldsymbol{\phi}}}{\sqrt{1+\tilde{\boldsymbol{\phi}}^T \tilde{\boldsymbol{\phi}}}} + \\ & + (c_{r2}|\boldsymbol{m}^*_{ext}|^2 + \epsilon|\boldsymbol{m}^*_{ext}|) + (c_{r4}|\breve{\boldsymbol{\omega}}|^2 + a_{r3}|\breve{\boldsymbol{\omega}}|) \\ \leq & -\min(\lambda_{min}(\boldsymbol{D}_{bq}), \epsilon\lambda_{min}(\tilde{\boldsymbol{K}}_{bq})) \frac{|\breve{\boldsymbol{\omega}}|^2 + |\tilde{\boldsymbol{\phi}}|^2}{\sqrt{1+|\breve{\boldsymbol{\omega}}|^2+|\tilde{\boldsymbol{\phi}}|^2}} + \\ & + (c_{r2}|\boldsymbol{m}^*_{ext}|^2 + \epsilon|\boldsymbol{m}^*_{ext}|) + (c_{r4}|\breve{\boldsymbol{\omega}}|^2 + a_{r3}|\breve{\boldsymbol{\omega}}|) = \\ = & -\gamma_r(|[\tilde{\boldsymbol{\phi}}^T \ \breve{\boldsymbol{\omega}}^T]^T|) + \sigma_{r2}(|\boldsymbol{m}^*_{ext}|) + \lambda_r(|\breve{\boldsymbol{\omega}}|)\end{aligned} \tag{6.36}$$

Hence, recalling the Definition 3 and considering $\boldsymbol{y} = \breve{\boldsymbol{\omega}}$, V_{r2} is an IOSS-Lyapunov function for the system (6.24). Moreover, $\limsup_{r\to\infty} \lambda_r(r)/\bar{\gamma}_r(r)$ is a constant, and thus the controlled system (6.24) is ISS stable for the Theorem 1.

As regards the translational dynamics, combining Eq. (6.7a) and Eq. (6.10) the controlled system is

$$m\dot{\boldsymbol{v}}_{c,t} + \boldsymbol{D}_c \boldsymbol{v}_{c,t} + \boldsymbol{K}_c \tilde{\boldsymbol{x}}_{c,t} = \boldsymbol{f}_{ext,c,t}. \tag{6.37}$$

In order to prove the input-to-state stability, the same passages as before are followed: it is proved that the controlled system admits a qISS Lyapunov function and an IOSS Lyapunov function. In this case, the demonstration is more straightforward since there is not the Coriolis/centrifugal term and the mass matrix is constant. In the following only the main steps are reported since the demonstration is analogous to the previous one on the attitude-joints dynamics.
Consider the following candidate Lyapunov function:

$$V_{t1} = \frac{1}{2} m \boldsymbol{v}^T_{c,t} \boldsymbol{v}_{c,t} + \frac{1}{2} \tilde{\boldsymbol{x}}^T_{c,t} \boldsymbol{K}_c \tilde{\boldsymbol{x}}_{c,t}. \tag{6.38}$$

The time derivative of V_{t1} is

$$\begin{aligned}\dot{V}_{t1} = & \boldsymbol{v}^T_{c,t} m \dot{\boldsymbol{v}}_{c,t} + \boldsymbol{v}^T_{c,t} \boldsymbol{K}_c \boldsymbol{x}_{c,t} = -\boldsymbol{v}^T_{c,t} \boldsymbol{D}_c \boldsymbol{v}_{c,t} + \boldsymbol{v}^T_{c,t} \boldsymbol{f}_{ext,c,t} \\ & \leq -c_{t1}|\boldsymbol{v}_{c,t}|^2 + c_{t2}|\boldsymbol{f}_{ext,c,t}|^2 = -\bar{\gamma}_t(|\boldsymbol{v}_{c,t}|) + \sigma_{t1}(|\boldsymbol{f}_{ext,c,t}|),\end{aligned} \tag{6.39}$$

where $c_{t1}, c_{t2} = \text{const.} > 0$. Therefore, recalling Definition 1 and Definition 4, the controlled system (6.37) is said to be passive w.r.t. the pair

$(\boldsymbol{v}_{c,t}, \boldsymbol{f}_{ext,c,t})$ and admits a qISS Lyapunov function.
Define another candidate Lyapunov function as follows

$$V_{t2} = \frac{1}{2} m \boldsymbol{v}_{c,t}^T \boldsymbol{v}_{c,t} + \frac{1}{2} \tilde{\boldsymbol{x}}_{c,t}^T \boldsymbol{K}_c \tilde{\boldsymbol{x}}_{c,t} + \epsilon \frac{\tilde{\boldsymbol{x}}_{c,t}^T m \boldsymbol{v}_{c,t}}{\sqrt{1 + \tilde{\boldsymbol{x}}_{c,t}^T \tilde{\boldsymbol{x}}_{c,t}}}, \tag{6.40}$$

with $\epsilon = \text{const.} > 0$ sufficiently small. The time derivative of V_{t2} can be computed as follows

$$\begin{aligned}
\dot{V}_{t2} =& \boldsymbol{v}_{c,t}^T m \dot{\boldsymbol{v}}_{c,t} + \boldsymbol{v}_{c,t}^T \boldsymbol{K}_c \boldsymbol{x}_{c,t} + \epsilon \frac{\boldsymbol{v}_{c,t}^T m \boldsymbol{v}_{c,t}}{\sqrt{1 + \tilde{\boldsymbol{x}}_{c,t}^T \tilde{\boldsymbol{x}}_{c,t}}} + \\
&+ \epsilon \frac{\tilde{\boldsymbol{x}}_{c,t}^T m \dot{\boldsymbol{v}}_{c,t}}{\sqrt{1 + \tilde{\boldsymbol{x}}_{c,t}^T, \tilde{\boldsymbol{x}}_{c,t}}} + \epsilon \frac{(\boldsymbol{x}_{c,t}^T \boldsymbol{v}_{c,t})(\boldsymbol{x}_{c,t}^T m \boldsymbol{v}_{c,t})}{(1 + \tilde{\boldsymbol{x}}_{c,t}^T \tilde{\boldsymbol{x}}_{c,t})^{\frac{3}{2}}} = \\
=& - \boldsymbol{v}_{c,t}^T \boldsymbol{D}_c \boldsymbol{v}_{c,t} + \boldsymbol{v}_{c,t}^T \boldsymbol{f}_{ext,c,t} + \epsilon \frac{\boldsymbol{v}_{c,t}^T m \boldsymbol{v}_{c,t}}{\sqrt{1 + \tilde{\boldsymbol{x}}_{c,t}^T \tilde{\boldsymbol{x}}_{c,t}}} + \\
&- \epsilon \frac{\tilde{\boldsymbol{x}}_{c,t} \boldsymbol{D}_c \boldsymbol{v}_{c,t}}{\sqrt{1 + \tilde{\boldsymbol{x}}_{c,t}^T \tilde{\boldsymbol{x}}_{c,t}}} - \epsilon \frac{\tilde{\boldsymbol{x}}_{c,t}^T \boldsymbol{K}_c \tilde{\boldsymbol{x}}_{c,t}}{\sqrt{1 + \tilde{\boldsymbol{x}}_{c,t}^T \tilde{\boldsymbol{x}}_{c,t}}} + \\
&+ \epsilon \frac{\tilde{\boldsymbol{x}}_{c,t}^T \boldsymbol{f}_{ext,c,t}}{\sqrt{1 + \tilde{\boldsymbol{x}}_{c,t}^T \tilde{\boldsymbol{x}}_{c,t}}} + \epsilon \frac{(\boldsymbol{x}_{c,t}^T \boldsymbol{v}_{c,t})(\boldsymbol{x}_{c,t}^T m \boldsymbol{v}_{c,t})}{(1 + \tilde{\boldsymbol{x}}_{c,t}^T \tilde{\boldsymbol{x}}_{c,t})^{\frac{3}{2}}} \\
\leq& - \boldsymbol{v}_{c,t}^T \boldsymbol{D}_c \boldsymbol{v}_{c,t} - \epsilon \frac{\tilde{\boldsymbol{x}}_{c,t}^T \boldsymbol{K}_c \tilde{\boldsymbol{x}}_{c,t}}{\sqrt{1 + \tilde{\boldsymbol{x}}_{c,t}^T \tilde{\boldsymbol{x}}_{c,t}}} + \boldsymbol{v}_{c,t}^T \boldsymbol{f}_{ext,c,t} + \\
&+ (2 a_{t1} |\boldsymbol{v}_{c,t}|^2 + a_{t3} |\boldsymbol{v}_{c,t}|) + \epsilon |\boldsymbol{f}_{ext,c,t}| \\
\leq& - \min(\lambda_{min}(\boldsymbol{D}_c), \epsilon \lambda_{min}(\boldsymbol{K}_c)) \frac{|\boldsymbol{v}_{c,t}|^2 + |\tilde{\boldsymbol{x}}_{c,t}|^2}{\sqrt{1 + |\boldsymbol{v}_{c,t}|^2 + |\tilde{\boldsymbol{x}}_{c,t}|^2}} + \\
&+ (c_{t4} |\boldsymbol{v}_{c,t}|^2 + a_{t3} |\boldsymbol{v}_{c,t}|) + (c_{t2} |\boldsymbol{f}_{ext,c,t}|^2 + \epsilon |\boldsymbol{f}_{ext,c,t}|) = \\
=& - \gamma_t([\tilde{\boldsymbol{x}}_{c,t}^T \ \boldsymbol{v}_{c,t}^T]^T) + \sigma_{t2}(|\boldsymbol{f}_{ext,c,t}|) + \lambda_t(|\boldsymbol{v}_{c,t}|),
\end{aligned} \tag{6.41}$$

where $a_{t1}, a_{t3}, c_{t4} = \text{const.} > 0$.
Recalling Definition 3, the controlled system (6.37) is said to admit an IOSS Lyapunov function. Since $\limsup_{r \to \infty} \lambda_t(r)/\bar{\gamma}_t(r)$ is a constant, it is possible to conclude that also the system (6.37) is ISS stable for Theorem 1.

6.5 Simulation example

6.5.1 Simulation scenario and setup

A spacecraft mounting a 7DoF robotic arm is considered. The kinematics and dynamics parameters are reported in Tab. 6.1. The spacecraft is equipped with 4 variable speed control moment gyros in a pyramid configuration and 12 thrusters, commanded through a PWM approach. The position of the actuators on the spacecraft is reported in Fig. 6.1. The model of the thrusters includes a delay in the activation, due to the opening/closure of the valve, a dead-zone and a first-order dynamics with different time constant for the rising and falling phase. Therefore, the controller commands a certain action, but the system receives a slightly different one. The characteristics of both actuators are reported in Tab. 6.2, where the parameters f_{max} is the maximum force provided by a single thruster, T_{pwm} is the PWM period, t_{delay} is the delay of the opening/closure of the valve, T_{rising} and $T_{falling}$ are the time constants of the first-order dynamics. The spacecraft is endowed with an IMU, measuring accelerations and angular velocities, a star tracker for the attitude, a vision system for measuring the relative distance, while the manipulator's joints position is measured by encoders. The model for the measurements is the same presented in Sect. 5.6.2, with the same level of noise, but $\sigma_{p_{bt}} = 0.005$ m. Also in this case, a kinematics-based Kalman filter is implemented for the velocity estimation and to have the attitude at higher frequency (see Sect. 5.6.2). The cameras and the star tracker work at 3 Hz, while the other sensors and the controller at 200 Hz. The prediction step in the filters is run at 200 Hz, while the update step at 3 Hz. The position, attitude and velocity of the end-effector are computed using the knowledge of the spacecraft's states and the kinematics of the manipulator.

Table 6.1: *Kinematics and dynamics parameters.*

	l [m]	m [kg]	I_x [kgm^2]	I_y [kgm^2]	I_z [kgm^2]
Base	1.2	150	15	21.8	18.8
Link 1	0.2	2.71	0.023	0.023	0.005
Link 2	0.2	2.71	0.026	0.026	0.053
Link 3	0.2	2.54	0.014	0.014	0.005
Link 4	0.2	2.50	0.028	0.028	0.005
Link 5	0.19	1.30	0.026	0.026	0.026
Link 6	0.12	1.57	0.003	0.003	0.003
Link 7	0	0.2	0.003	0.003	0.003

Table 6.2: *Actuators parameters.*

	Parameters		
VSCMG	$I_{ws} = 0.042\text{kgm}^2$ $I_{gs} = 0.093\text{kgm}^2$	$I_{wt} = 0.024\text{kgm}^2$ $I_{gt} = 0.054\text{kgm}^2$	$I_{wg} = 0.024\text{kgm}^2$ $I_{gg} = 0.054\text{kgm}^2$
Thrusters	$f_{max} = 4$ N $T_{rising} = 1.5$ ms	$T_{pwm} = 50$ ms $T_{falling} = 3$ ms	$t_{delay} = 8$ ms

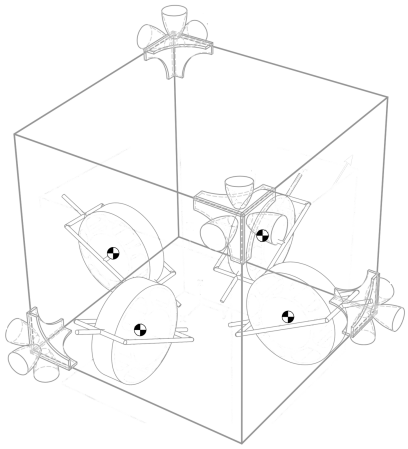

Figure 6.1: *Position of the thrusters and VSCMG on the spacecraft.*

Initially, the controller presented in [75] is active. The space robot is commanded to keep the initial attitude and position of the CM. The end-effector is controlled to follow a trapezoidal velocity profile along the y direction, while keeping the initial orientation and initial position along x and z.
At a certain time instant, the link 5 of the manipulator collides with another object. To simulate the contact, the *Dymola* library presented in [78] is used, in which the normal force is modeled as reported in Eq. (5.44). The residuals $\hat{\boldsymbol{m}}_{ext,c}$ and $\hat{\tilde{\boldsymbol{\tau}}}^*_{ext}$ are exploited to detect the collision and trigger the reaction control (6.10)-(6.11). The new setpoints for the joints position and the CM position are set through Eqs. (6.14)-(6.15), while the attitude is kept. For the translational and attitude control, the gains are the same for x, y and z directions: $k_c = 100$ Nm^{-1} and $d_c = 250$ Ns, $k_{\tilde{\epsilon}} = 1500$ Nmrad^{-1} and $d_{\omega_b} = 300$ Nmsrad^{-1}. For the first four joints, the gains $k_{\tilde{q}} = 70$ Nmrad^{-1} and $d_{\tilde{q}} = 10.5$ Nmsrad^{-1} are set, while for the other joints, $k_{\tilde{q}} = 1$ Nmrad^{-1} and $d_{\tilde{q}} = 0.2$ Nmsrad^{-1}. The parameters Δ_{x_c} and Δ_q are set equal to 0.60 m and 0.26 rad. Finally, the gains for the computation of the residuals $\hat{\boldsymbol{m}}_{ext,c}$ and $\hat{\tilde{\boldsymbol{\tau}}}^*_{ext}$ are set equal to 20 s^{-1}.

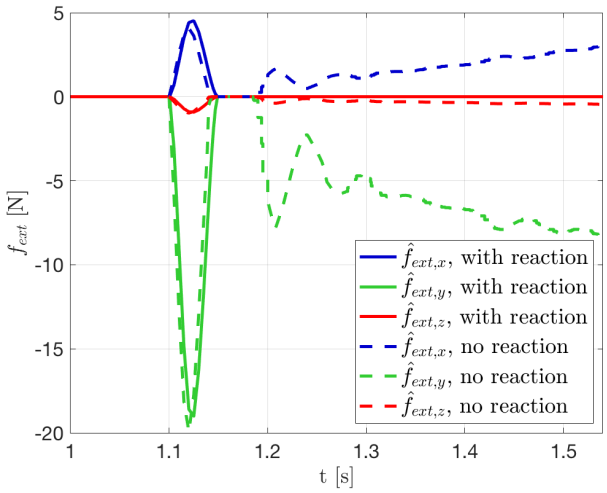

Figure 6.2: *Contact force generated by the collision in case the reaction control is active and in case it is not.*

6.5.2 Results

In Fig. 6.2, the force generated in the collision is reported in the case in which the reaction control is activated and in the case in which it is not. In the latter situation, the space robot does not recognize the contact and try to pursue the first goal, namely to move the end-effector along the direction y. Consequently, multiple contacts and the build-up of the force occur. This is a dangerous condition since instability can arise and robot can be affected by serious damages, jeopardizing the mission. On the other hand, if the proposed reaction control is activated, the contact is detected and the robot moves away avoiding other collisions and the increase of the force. In this way, the possible damages are mitigated and the space robot can reach a safe position, where then the subsequent actions can be planned. It is important to stress that this is a capability an autonomous space robot should have in order to carry out the mission safely. Indeed, in the future, it may be required to operate in an unstructured scenario, involving several proximity operations close to other objects.
Figs. 6.3-6.4 show the residuals $\hat{\boldsymbol{m}}_{ext,c}$ and $\hat{\tilde{\boldsymbol{\tau}}}^{*}_{ext}$, and the set thresholds for the detection. The contact is detected both at the angular momentum level and at the joint level. In particular, the contact is recognized on the components x and z of $\hat{\boldsymbol{m}}_{ext,c}$ and by the monitoring signals at the joints 1 and 3. In Fig. 6.5, the effects of the discrepancy between the commanded thrusters' force and the real one, which includes delay and first-order dy-

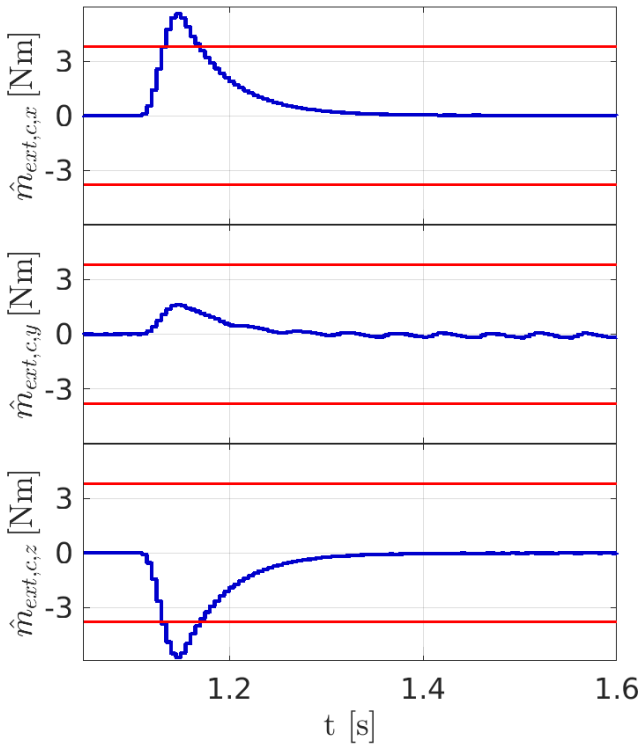

Figure 6.3: *Components of the residual $\hat{\boldsymbol{m}}_{ext,c}$ and the set thresholds (red line).*

namics, on the residual computation can be noted. Note that this discrepancy, along with other uncertainties and measurements noise, affects the selection of the threshold, and thus the sensitivity. The amplitude of these oscillations can be modified acting on the observer gains.
In Fig. 6.6, the position of the CM of the whole system is reported. Until the contact occurred, the position is constant, then the reaction control is activated and the entire spacecraft-manipulator system translates away from the obstacle reaching the new setpoint. Note that the setpoint is computed using Eq. (6.14), where the external force is estimated through Eq. (6.21), and the direction of the motion after the contact is along the line of action of the force (see also Fig. 6.2). For the reconstruction, the knowledge of the contact point is necessary and it is performed following the scheme presented in Sect. 5.5.2. Therefore, in the simulation, the complete loop detection, isolation, identification and reaction is implemented and works satisfactorily.

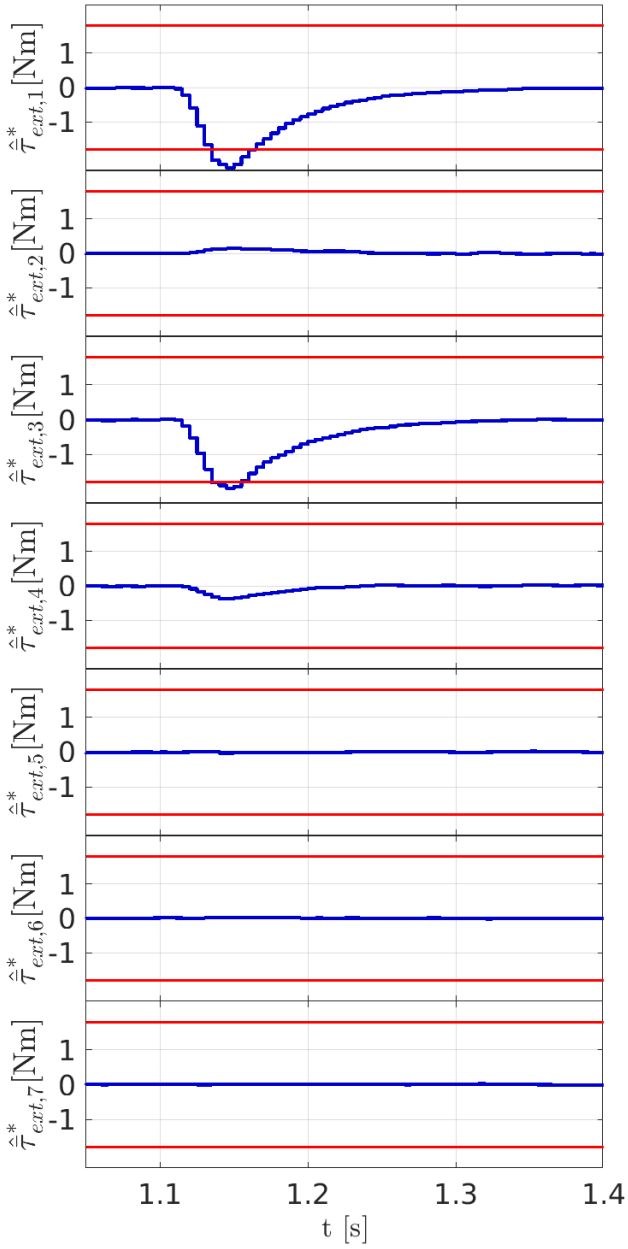

Figure 6.4: *Components of the residual $\hat{\hat{\tau}}^*_{ext}$ and the set thresholds (red line).*

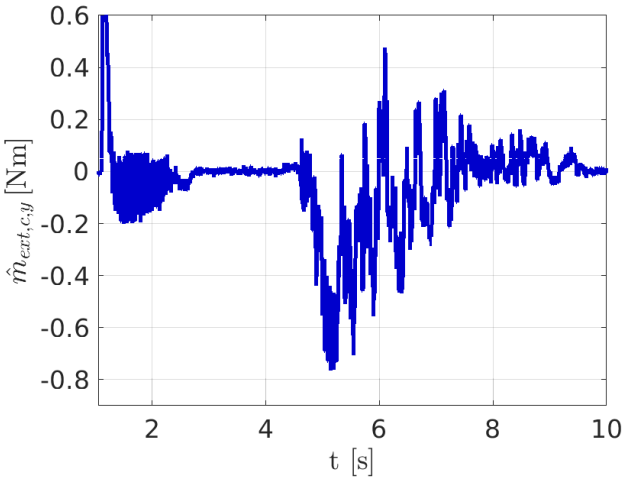

Figure 6.5: *Effects of the non-modelled dynamics of the thrusters on the residual* $\hat{\boldsymbol{m}}_{ext,c}$.

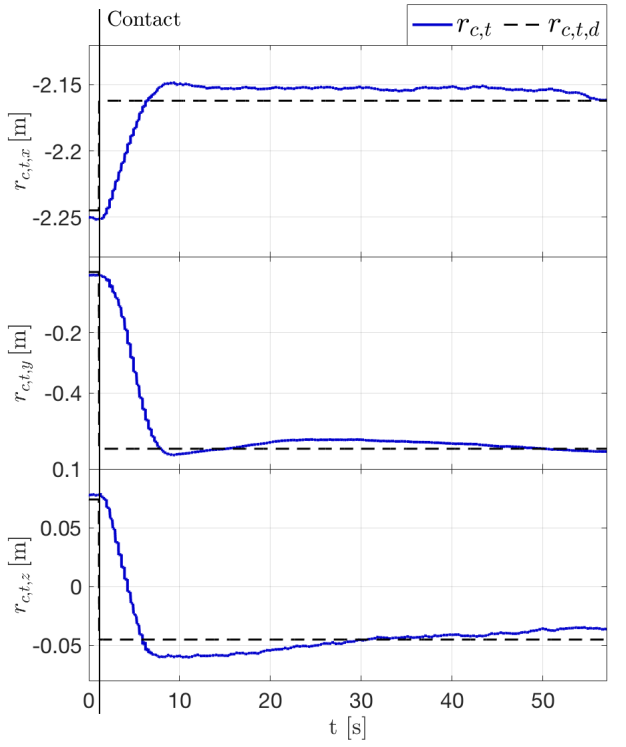

Figure 6.6: *Response of the CM position before and after the contact.*

The error on the absolute angles of the spacecraft is reported in Fig. 6.7. The error is always small, even during the contact phase, and it further decreases after the contact. Note that keeping a certain orientation of the spacecraft can be required either to communicate or to have the target in the field of view of some sensors, e.g. camera or lidar.
Finally, Fig. 6.8 reports the response of the joints position. Before the contact, the manipulator moves towards the obstacle, following the desired trajectory imposed in the end-effector space. Afterwards, the collision occurred and the new desired positions for the joints are computed by Eq. (6.15). Smooth trajectories are generated and the manipulator escapes from the obstacle successfully. Note that the directions followed by the joints in the post-impact phase is the one identified by the residual $\hat{\hat{\boldsymbol{\tau}}}^*_{ext}$ (see Fig. 6.4).

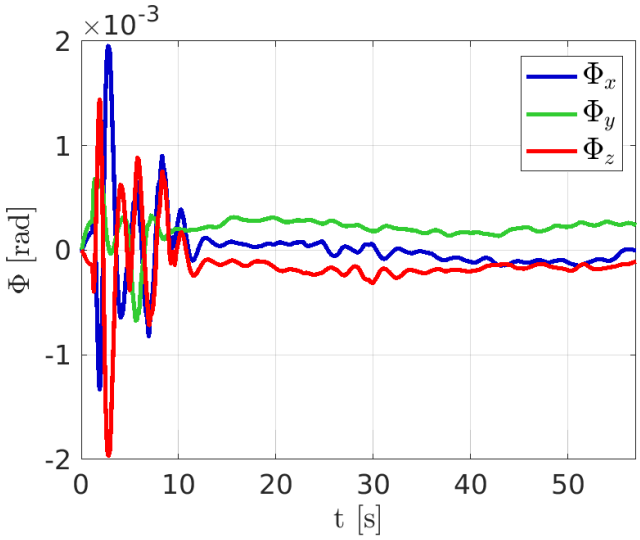

Figure 6.7: *Error on the Euler angles of the spacecraft.*

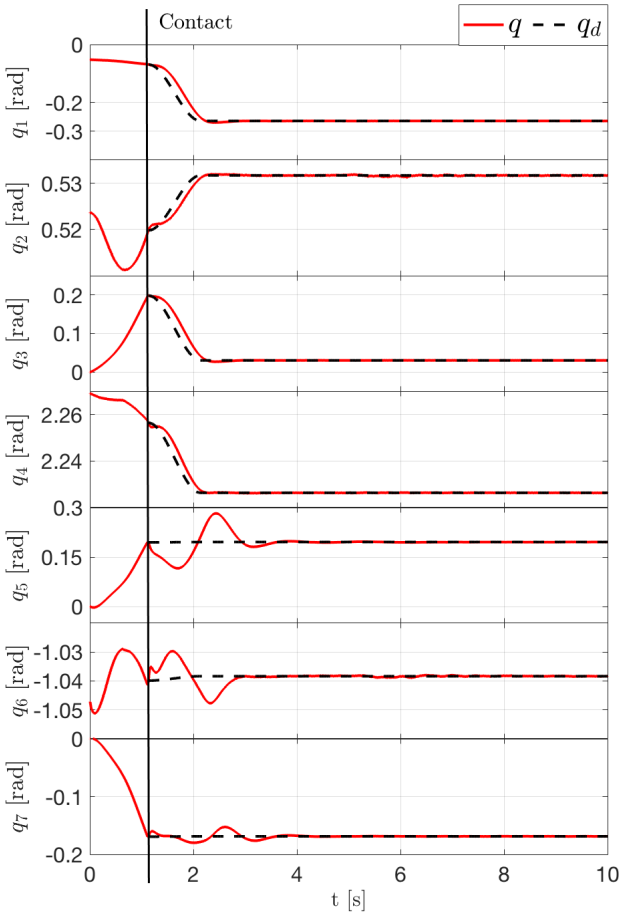

Figure 6.8: *Response of the position of the joints before and after the contact.*

CHAPTER 7

Conclusions

This study aimed at developing techniques to address some of the main challenges involved in an on-orbit autonomous robotic mission with manipulators. Especially, the relative pose estimation problem and the physical contact handling have been considered, with particular attention on unexpected collisions.
Before performing tasks with the robotic arm, the relative position and attitude of a target satellite with respect to the servicer is a key information for the navigation system. A proper characterization of the motion of the target is necessary to plan the approaching strategy during close-proximity operations. To this aim, two nonlinear filters have been proposed based on the differential algebra: an high-order numerical extended Kalman filter and an unscented Kalman filter. In the former one system nonlinearity are incorporated in terms of high-order Taylor expansions. In the original version, high-order partials have to be derived and integrated each time instant. On the other hand, this computational-demanding and cumbersome operation is completely avoided exploiting differential algebra. Indeed, the high-order partials are directly obtained through the integration of the dynamics in the DA framework, which provides the Taylor expansion of the flow up to an arbitrary order. Consequently, an easier and straightforward

implementation of the HNEKF is achieved. It has been shown that, actually, orders greater than two do not improve the accuracy of the filter. This is due to the fact that Kalman filter is based on the Gaussian hypothesis, namely only the first two moments, mean and covariance, are necessary to describe all random distributions. Indeed, in the considered cases, second order expansion already introduces sufficient information for an accurate estimation of these moments. Another important feature of a filter is the on-board applicability: the filter should work in real-time with low computational power available. Therefore, the DA-based HNEKF has been implemented on a BeagleBone Black platform, representative of the limited computational capability of space processors. Differently from the HNEKF, the unscented Kalman filter relies on the unscented transformation. The mean and covariance at a time instant $k+1$ are reconstructed by carefully chosen points, which are propagated through the dynamics. Thanks to the differential algebra, it is possible to substitute multiple integrations with an easier polynomial evaluation. As before, the integration of the dynamics in the DA framework provides the Taylor expansion of the flow, and thus to obtain the propagated sigma points it is sufficient to evaluate the polynomial in those points. The DA-based UKF turns out to be faster and computational lighter that the standard counterpart, especially when the dynamics integration is particularly demanding. The performance of both filters, in terms of accuracy and computational burden, have been assessed considering the e.Deorbit mission, considering camera measurements. This scenario is particularly challenging since it involves a noncooperative target characterized by tumbling motion. The results showed that the DA-based HNEKF is the most accurate, while the DA-based UKF is the fastest one.

Once the space robot carried out the rendezvous, the manipulator can be deployed and proximity operations, such as manipulation or inspection, can be performed. In this phase, physical contact situations may arise and must be handled properly. They can be planned, as in the case of a grasping task, or occur unexpectedly due to failures or errors. In both cases the knowledge of the contact force is a valuable information to trigger a reaction and to implement efficient control algorithms. Two observers have been introduced to estimate the contact force. One is based on a base-joints dynamics formulation, while the other one on a centroid-joints dynamics. In both schemes, three momentum-based residuals have been defined, which can be used to reconstruct the external wrench. It has been shown that the latter one provides better performance when realistic measurements are considered, thanks to the decoupling from the spacecraft's linear velocity of the angular and joints momentum residuals. The observers have been validated

on the On-Orbit Servicing Simulator facility of the DLR. Moreover, a strategy to isolate the point at which the contact occurred has been proposed. Along with the observers, another approach based on monitoring the total momentum of the space robot has been analyzed to address the contact detection and isolation problems. It turns out that, even if some interesting results have been obtained with the momentum monitoring technique, the observer based on a centroid-joints dynamics is a better solution from practical point of view. Indeed, it enables to deal with different kind of contacts, impulsive and continuous, and relies only on sensors featuring relatively low noise and high acquisition frequency, meaning that fast contacts can be promptly detected, accurately isolated and estimated.
Finally, a compliant reaction control strategy to unexpected collisions is also presented. The goal of the control is to move the space robot away from the hit obstacle, while keeping the attitude. In particular, the center of mass of the whole system and the joints position are controlled to follow the motion caused by the contact force. The direction of the force and its projection in the joints space are provided by the contact wrench reconstruction and the joints momentum residuals, respectively. In this way, the robot can escape from the obstacle reaching a safe configuration and position, while keeping the desired attitude, which is important for communication or to retain the target in the field of view of the sensors. The controlled system is demonstrated to be input-to-state stable, namely the error on the states is bounded even when the collision is taking place. The performance of the control is assessed through numerical simulations, considering a realistic measurement model and actuators. In particular, a general model for momentum exchange devices is implemented, including reaction wheels, control moment gyros and variable speed control moment gyros. Moreover, thrusters are modeled including valve delay, dead zone and a first order dynamics. Thanks to the reaction control, multiple hits and the build-up of the contact force are avoided, preventing instability and severe damages.

7.1 Future works

Different paths can be followed to further develop the work presented in this thesis. One of them is to integrate the proposed algorithms. After acquiring the motion information of the target satellite and performing the rendezvous maneuver, the space robot comes closer to the target and the robotic arm is deployed. At this point, the relative pose information are still required, but also the end-effector's states are necessary. Indeed, either an inspection task or a manipulation task are planned, the motion informa-

tion of the target are essential to generate an end-effector trajectory and the end-effector's states are requested by the controller. The end-effector's position and orientation, and velocity as well, can be reconstructed through the knowledge of the pose of the base and the kinematics. However, noise and uncertainties would deteriorate significantly the positioning accuracy. A better solution is to equip the manipulator with cameras measuring the relative distance and orientation of the end-effector with respect to the target. Cameras usually work at relatively low frequency, while the manipulator's controller requires higher frequency to provide good performance. Therefore, a filter estimating all the non-measured quantities can be designed, namely end-effector's and target's relative states. This filter can use the information from the DA-based filters for the initialization. The prediction step has to run at high frequency, and thus it could be convenient to implement a kinematics-based filter, similar to the one used in the simulations of this thesis, to estimate the base velocity and the attitude. Another solution could be to use two separate filters, one for the relative position of the target and one for the end-effector and attitude. Indeed, the first one can be used for the spacecraft position control at lower frequency, while the other one is used for the manipulator and attitude control at higher frequency. Note that the manipulator and rotational dynamics are expected to be faster than the translational one. To this aim, the decoupled dynamics (6.7) can be particularly useful. In this way, a smaller system has to be propagated inside the high-frequency filter, probably reducing the computational cost. For the control, a possible solution has been already presented, which integrates a compliant controller for the nominal operation (working in the operational space) with the proposed reaction controller (working in the joints space). The contact observer information is exploited to recognize the nature of the contact, desired or unintentional, and to switch between them. Moreover, in case of an unexpected collision, the proposed observer provides information about the direction to follow in order to move away from the obstacle and about the location of the contact, which can be used for health monitoring purpose. Finally, another problem that must be addressed is the generation of the end-effector trajectory, in which the knowledge of the servicer and target states is used.

Appendix

A Derivation of the relations (5.13)

Deriving the relations (5.13a) and (5.13b) is straightforward. Indeed, the differentiation of the momenta $\boldsymbol{h}_c^t$ and $\boldsymbol{h}_c^r$, which are expressed in a frame rotating with an angular velocity $\boldsymbol{\omega}_b$, results in

$$\dot{\boldsymbol{h}}_c^t + [\boldsymbol{\omega}_b]^\times \boldsymbol{h}_c^t = \boldsymbol{f}_{c,tot} \tag{A.1}$$

$$\dot{\boldsymbol{h}}_c^r + [\boldsymbol{\omega}_b]^\times \boldsymbol{h}_c^r = \boldsymbol{m}_{c,tot} \tag{A.2}$$

where $\boldsymbol{f}_{c,tot} \in \mathbb{R}^3$, $\boldsymbol{m}_{c,tot} \in \mathbb{R}^3$ are the total centroidal force and moment acting on the system. Recalling that $\boldsymbol{h}_c^t = m\boldsymbol{v}_c$ and comparing Eq. (A.1) with the first row of Eq. (5.11), the first relation (5.13a) is obtained. Similarly, comparing Eq. (A.2) with the second row of Eq. (5.11), the second relation (5.13b) is obtained.
For what concerns the third relation (5.13c), a quasi-Lagrangian approach [81] is used to rederive the joints equation in (5.11). Then, the relation (5.13c) is obtained by comparison of the quasi-Lagrangian joints formulation with the third row of Eq. (5.11). In the quasi-Lagrangian formulation, the generalized velocities $\boldsymbol{v}_c$ and $\boldsymbol{h}_c^r$ are called quasi-velocities since they are not integrable. In order to derive the dynamic equations, some integrable generalized coordinates $\boldsymbol{y} \in \mathbb{R}^{6+n}$ are defined, whose derivatives are related to the quasi-velocities as follows:

$$\begin{bmatrix} \boldsymbol{v}_c \\ \boldsymbol{h}_c^r \\ \dot{\boldsymbol{q}} \end{bmatrix} = \begin{bmatrix} \boldsymbol{E} & -[\boldsymbol{r}_c]^\times \boldsymbol{J}_\Phi^{-1} & \boldsymbol{0} \\ \boldsymbol{0} & \boldsymbol{I}_c \boldsymbol{J}_\Phi^{-1} & \boldsymbol{I}_c \bar{\boldsymbol{J}}_\omega \\ \boldsymbol{0} & \boldsymbol{0} & \boldsymbol{E} \end{bmatrix} \begin{bmatrix} \dot{\boldsymbol{r}}_c \\ \dot{\boldsymbol{\Phi}} \\ \dot{\boldsymbol{q}} \end{bmatrix} = \boldsymbol{\Xi}^T \dot{\boldsymbol{y}}, \tag{A.3}$$

where $\boldsymbol{r}_c \in \mathbb{R}^3$, $\dot{\boldsymbol{r}}_c \in \mathbb{R}^3$ are the position of the CM of the whole system expressed in $\mathcal{C}$ and its time derivative, respectively; $\boldsymbol{\Phi} \in \mathbb{R}^3$, $\dot{\boldsymbol{\Phi}} \in \mathbb{R}^3$ are the Euler angle vector and its time derivative, respectively; $\boldsymbol{J}_\Phi \in \mathbb{R}^{3\times 3}$ is the Jacobian mapping $\boldsymbol{\omega}_b$ in $\dot{\boldsymbol{\Phi}}$. The matrix $\boldsymbol{\Xi}$ is function of the generalized coordinates $\boldsymbol{y}$. Note that any rotation parameterization different from the Euler angles can be used without affecting the following joints dynamics derivation.
Introducing $\boldsymbol{x} = [\boldsymbol{v}_c^T \ \boldsymbol{h}_c^{rT} \ \dot{\boldsymbol{q}}^T]^T \in \mathbb{R}^{6+n}$ and assuming that $\boldsymbol{\Xi}^T$ is invertible, the following relation can be written:

$$\dot{\boldsymbol{y}} = \boldsymbol{\Omega} \boldsymbol{x} \tag{A.4}$$

where $\boldsymbol{\Omega} = \boldsymbol{\Xi}^{-T} \in \mathbb{R}^{(6+n)\times(6+n)}$.
Exploiting Eqs. (A.3)-(A.4), the quasi-Lagrangian formulation can be derived from the standard one [81], resulting in

$$\delta \boldsymbol{y}^T \left(\boldsymbol{\Xi} \frac{d}{dt} \left[\frac{\partial T}{\partial \boldsymbol{x}} \right] + \dot{\boldsymbol{\Xi}} \frac{\partial T}{\partial \boldsymbol{x}} - \frac{\partial T}{\partial \boldsymbol{y}} - \boldsymbol{H} \frac{\partial T}{\partial \boldsymbol{x}} - \boldsymbol{Q} \right) = 0, \tag{A.5}$$

where

$$\boldsymbol{H} = \begin{bmatrix} \boldsymbol{x}^T \boldsymbol{\Omega}^T \frac{\partial \boldsymbol{\Xi}}{\partial y_1} \\ \vdots \\ \boldsymbol{x}^T \boldsymbol{\Omega}^T \frac{\partial \boldsymbol{\Xi}}{\partial y_{6+n}} \end{bmatrix} \in \mathbb{R}^{(6+n)\times(6+n)}; \tag{A.6}$$

$\boldsymbol{Q} \in \mathbb{R}^{6+n}$ is the vector of the generalized forces; $T \in \mathbb{R}$ is the kinetic energy of the system expressed in terms of $\boldsymbol{x}$. The potential energy is assumed to be zero. T can be computed as follows

$$T = \frac{1}{2} \left(m \boldsymbol{v}_c^T \boldsymbol{v}_c + \dot{\boldsymbol{q}}^T \boldsymbol{M}_m^* \dot{\boldsymbol{q}} + \boldsymbol{h}_c^{rT} \boldsymbol{I}_c^{-T} \boldsymbol{h}_c^r \right). \tag{A.7}$$

The matrices $\dot{\boldsymbol{\Xi}}$ and $\boldsymbol{\Omega}^T \frac{\partial \boldsymbol{\Xi}}{\partial y_i}$, appearing in Eqs. (A.5)-(A.6), can be expanded as

$$\dot{\boldsymbol{\Xi}} = \begin{bmatrix} \boldsymbol{0} & \boldsymbol{0} & \boldsymbol{0} \\ \dot{\boldsymbol{J}}_\Phi^{-T} [\boldsymbol{r}_c]^\times + \boldsymbol{J}_\Phi^{-T} [\dot{\boldsymbol{r}}_c]^\times & \dot{\boldsymbol{J}}_\Phi^{-T} \boldsymbol{I}_c^T + \boldsymbol{J}_\Phi^{-T} \dot{\boldsymbol{I}}_c^T & \boldsymbol{0} \\ \boldsymbol{0} & \dot{\bar{\boldsymbol{J}}}_\omega^T \boldsymbol{I}_c^T + \bar{\boldsymbol{J}}_\omega^T \dot{\boldsymbol{I}}_c^T & \boldsymbol{0} \end{bmatrix} \tag{A.8}$$

$$\boldsymbol{\Omega}^T \frac{\partial \boldsymbol{\Xi}}{\partial y_i} = \begin{bmatrix} \mathbf{0} & \mathbf{0} & \mathbf{0} \\ \boldsymbol{I}_c^{-T} \boldsymbol{J}_\Phi^T \frac{\partial (\boldsymbol{J}_\Phi^{-T} [\boldsymbol{r}_c]^\times)}{\partial y_i} & \boldsymbol{I}_c^{-T} \boldsymbol{J}_\Phi^T \frac{\partial (\boldsymbol{J}_\Phi^{-T} \boldsymbol{I}_c^T)}{\partial y_i} & \mathbf{0} \\ -\bar{\boldsymbol{J}}_\omega^T \boldsymbol{J}_\Phi^T \frac{\partial (\boldsymbol{J}_\Phi^{-T} [\boldsymbol{r}_c]^\times)}{\partial y_i} & -\bar{\boldsymbol{J}}_\omega^T \boldsymbol{J}_\Phi^T \frac{\partial (\boldsymbol{J}_\Phi^{-T} \boldsymbol{I}_c^T)}{\partial y_i} + \frac{\partial (\bar{\boldsymbol{J}}_\omega^T \boldsymbol{I}_c^T)}{\partial y_i} & \mathbf{0} \end{bmatrix} \tag{A.9}$$

Therefore, the matrix $\boldsymbol{H}$ has this form:

$$\boldsymbol{H} = \begin{bmatrix} \boldsymbol{x}^T \boldsymbol{\Omega}^T \frac{\partial \boldsymbol{\Xi}}{\partial y_1} \\ \vdots \\ \boldsymbol{x}^T \boldsymbol{\Omega}^T \frac{\partial \boldsymbol{\Xi}}{\partial y_{6+n}} \end{bmatrix} = \begin{bmatrix} \boldsymbol{H}_t & \boldsymbol{H}_{tr} & \mathbf{0} \\ \boldsymbol{H}_{rt} & \boldsymbol{H}_r & \mathbf{0} \\ \boldsymbol{H}_{mt} & \boldsymbol{H}_{mr} & \mathbf{0} \end{bmatrix} \tag{A.10}$$

Since the joints dynamics is of interest, only the last n rows of the Lagrangian system can be considered. Hence, only the last n rows of $\boldsymbol{H}$ are expanded. It can be noted that $\boldsymbol{H}_{mt} = \mathbf{0}$ because neither $\boldsymbol{J}_\Phi$ nor $\boldsymbol{r}_c$ depend on $\boldsymbol{q}$, while $\boldsymbol{H}_{mr}$ can be expanded as follows

$$\begin{aligned} \boldsymbol{H}_{mr} &= \begin{bmatrix} \boldsymbol{h}_c^{rT} \boldsymbol{I}_c^{-T} \frac{\partial \boldsymbol{I}_c^T}{\partial q_1} + \dot{\boldsymbol{q}}^T \frac{\partial \bar{\boldsymbol{J}}_\omega^T}{\partial q_1} \boldsymbol{I}_c^T \\ \vdots \\ \boldsymbol{h}_c^{rT} \boldsymbol{I}_c^{-T} \frac{\partial \boldsymbol{I}_c^T}{\partial q_n} + \dot{\boldsymbol{q}}^T \frac{\partial \bar{\boldsymbol{J}}_\omega^T}{\partial q_n} \boldsymbol{I}_c^T \end{bmatrix} = \\ &= -\boldsymbol{I}_{c/q}^{-T} \boldsymbol{I}_c^T + \bar{\boldsymbol{J}}_{\omega/q}^T \boldsymbol{I}_c^T, \end{aligned} \tag{A.11}$$

where $\boldsymbol{I}_{c/q}^{-T}$, $\bar{\boldsymbol{J}}_{\omega/q}^T$ are reported in Eqs. (5.15) and (5.16), respectively. Considering that

$$\frac{\partial T}{\partial \boldsymbol{x}} = \begin{bmatrix} m \boldsymbol{v}_c \\ \boldsymbol{I}_c^{-T} \boldsymbol{h}_c^r \\ \boldsymbol{M}_m^* \dot{\boldsymbol{q}} \end{bmatrix}, \tag{A.12}$$

$$\frac{\partial T}{\partial \boldsymbol{y}} = \mathbf{0}, \tag{A.13}$$

after some simplification, the joints dynamic equation turns out to be

$$\begin{aligned} &\bar{\boldsymbol{J}}_\omega^T \boldsymbol{I}_c^T (\boldsymbol{I}_c^{-T} \dot{\boldsymbol{h}}_c^r + \dot{\boldsymbol{I}}_c^{-T} \boldsymbol{h}_c^r) + \boldsymbol{M}_m^* \ddot{\boldsymbol{q}} + \dot{\boldsymbol{M}}_m^* \dot{\boldsymbol{q}} + \dot{\bar{\boldsymbol{J}}}_\omega^T \boldsymbol{h}_c^r + \\ &-\frac{1}{2} (\boldsymbol{M}_{m/q}^* \dot{\boldsymbol{q}} - \boldsymbol{I}_{c/q}^{-T} \boldsymbol{h}_c^r) - \bar{\boldsymbol{J}}_{\omega/q}^T \boldsymbol{h}_c^r + \bar{\boldsymbol{J}}_\omega^T \dot{\boldsymbol{I}}_c^T \boldsymbol{I}_c^{-T} \boldsymbol{h}_c^r = \\ &= \boldsymbol{\tau}_{tot} - \bar{\boldsymbol{J}}_v^T \boldsymbol{f}_{b,tot} \end{aligned} \tag{A.14}$$

where $\boldsymbol{\tau}_{tot} \in \mathbb{R}^n$ are the total torques acting on the joints, i.e., including commanded torques and disturbance torques; $\boldsymbol{f}_{b,tot} \in \mathbb{R}^n$ are the total

forces acting on the base, i.e., including commanded forces and disturbance forces.
Substituting $\dot{\boldsymbol{h}}_c^r$ from Eq. (A.2) and $\dot{\boldsymbol{I}}_c^T = -\boldsymbol{I}_c^T \dot{\boldsymbol{I}}_c^{-T} \boldsymbol{I}_c^T$, and using relations (5.9) and (5.10), the dynamics (A.14) can be rewritten as

$$\begin{aligned} \boldsymbol{M}_m^* \ddot{\boldsymbol{q}} + (\dot{\boldsymbol{M}}_m^* - \frac{1}{2}\boldsymbol{M}_{m/q}^*)\dot{\boldsymbol{q}} + (\dot{\bar{\boldsymbol{J}}}_\omega^T - \bar{\boldsymbol{J}}_\omega^T [\boldsymbol{\omega}_b]^\times + \\ + \frac{1}{2}\boldsymbol{I}_{c/q}^{-T} - \bar{\boldsymbol{J}}_{\omega/q}^T)\boldsymbol{h}_c^r = \bar{\boldsymbol{\tau}}_{tot}, \end{aligned} \tag{A.15}$$

where $\bar{\boldsymbol{\tau}}_{tot} = \bar{\boldsymbol{\tau}} + \bar{\boldsymbol{\tau}}_{ext} \in \mathbb{R}^n$.
Finally, comparing Eq. (A.15) and the third row of Eq. (5.11), the relation (5.13c) can be obtained.

B Derivation of the relations (6.5)

This derivation is along the lines of the previous one in Sect. A. To derive the relation $\tilde{\boldsymbol{C}}_{cr}\boldsymbol{\omega}_b + \tilde{\boldsymbol{C}}_{cm}\dot{\boldsymbol{q}} = \boldsymbol{0}$, it is sufficient to write the time derivative of the translational momentum in the inertial frame and compare it to the first row of Eq. (6.4). Indeed,

$$\dot{\boldsymbol{h}}_{ct}^t = m\dot{\boldsymbol{v}}_{c,t} = \boldsymbol{f}_{c,t,tot}, \tag{B.16}$$

where $\boldsymbol{f}_{c,t,tot} \in \mathbb{R}^3$ is the total centrical force in the inertial frame, thus including $\boldsymbol{f}_{c,t}$ and $\boldsymbol{f}_{ext,c,t}$. Therefore, comparing Eq. (B.16) and the first row of Eq. (6.4), the relation $\tilde{\boldsymbol{C}}_{cr}\boldsymbol{\omega}_b + \tilde{\boldsymbol{C}}_{cm}\dot{\boldsymbol{q}} = \boldsymbol{0}$ can be obtained.
Deriving the relation (6.5a) is straightforward. Considering Eq. (A.2) and that $\boldsymbol{h}_c^r = \boldsymbol{I}_c\boldsymbol{\omega}_b + \boldsymbol{I}_c\bar{\boldsymbol{J}}_\omega\dot{\boldsymbol{q}}$, it is possible to write

$$\boldsymbol{I}_c\dot{\boldsymbol{\omega}}_b + \boldsymbol{I}_c\bar{\boldsymbol{J}}_\omega\ddot{\boldsymbol{q}} + \dot{\boldsymbol{I}}_c\boldsymbol{\omega}_b + \dot{\boldsymbol{I}}_c\bar{\boldsymbol{J}}_\omega\dot{\boldsymbol{q}} + \boldsymbol{I}_c\dot{\bar{\boldsymbol{J}}}_\omega\dot{\boldsymbol{q}} + [\boldsymbol{\omega}_b]^\times(\boldsymbol{I}_c\boldsymbol{\omega}_b + \boldsymbol{I}_c\bar{\boldsymbol{J}}_\omega\dot{\boldsymbol{q}}) = \boldsymbol{m}_{c,tot}. \tag{B.17}$$

Again, comparing Eq. (B.17) with the second row of Eq. (6.4), the relation (6.5a) is derived.
Finally, as regards the relation (6.5b), the idea is the same presented before in Sect. A, namely the joints equation is derived using the quasi-Lagrangian formulation and then compared to the third row of Eq. (6.4). In this case the derivative of the generalized coordinates $\boldsymbol{y}$ are related to the quasi-velocities in the following way:

$$\begin{bmatrix} \boldsymbol{v}_{c,t} \\ \boldsymbol{\omega}_b \\ \dot{\boldsymbol{q}} \end{bmatrix} = \begin{bmatrix} \boldsymbol{E} & \boldsymbol{0} & \boldsymbol{0} \\ \boldsymbol{0} & \boldsymbol{J}_\Phi^{-1} & \boldsymbol{0} \\ \boldsymbol{0} & \boldsymbol{0} & \boldsymbol{E} \end{bmatrix} \begin{bmatrix} \dot{\boldsymbol{p}}_{tc} \\ \dot{\boldsymbol{\Phi}} \\ \dot{\boldsymbol{q}} \end{bmatrix} = \boldsymbol{\Xi}^T\dot{\boldsymbol{y}}. \tag{B.18}$$

It can be noticed that the joints coordinates are not associated with nonholonomic relations. Consequently, for these degrees of freedom, the general equation (A.5) is simply the standard Lagrange equation [81]. The kinetic energy can be computed as follows

$$T = \frac{1}{2}(m\boldsymbol{v}_{c,t}^T\boldsymbol{v}_{c,t} + \breve{\boldsymbol{\omega}}^T\boldsymbol{M}_{bq}\breve{\boldsymbol{\omega}}). \tag{B.19}$$

Applying the Lagrange formalism to derive the joints dynamics, this equation is obtained:

$$\begin{aligned}\tilde{\boldsymbol{M}}_m\ddot{\boldsymbol{q}} + \bar{\boldsymbol{J}}_\omega^T\boldsymbol{I}_c^T\dot{\boldsymbol{\omega}}_b + (\dot{\tilde{\boldsymbol{M}}}_m - \frac{1}{2}\tilde{\boldsymbol{M}}_{rm/q} - \frac{1}{2}\tilde{\boldsymbol{M}}_{m/q})\dot{\boldsymbol{q}} + \\ +(\dot{\bar{\boldsymbol{J}}}_\omega^T\boldsymbol{I}_c^T + \bar{\boldsymbol{J}}_\omega^T\dot{\boldsymbol{I}}_c^T + \frac{1}{2}\boldsymbol{I}_{c/q}^{-T}\boldsymbol{I}_c - \frac{1}{2}\bar{\boldsymbol{J}}_{\omega/q}^T\boldsymbol{I}_c^T)\boldsymbol{\omega}_b = \bar{\boldsymbol{\tau}}_{tot}^*\end{aligned} \tag{B.20}$$

where $\tilde{\boldsymbol{M}}_{m/q}$ and $\tilde{\boldsymbol{M}}_{rm/q}$ are defined in Eq. (6.6). In (B.20), the following relations have been used

$$\begin{bmatrix} \boldsymbol{\omega}_b^T\frac{\partial \boldsymbol{I}_c^T}{\partial q_1} \\ \vdots \\ \boldsymbol{\omega}_b^T\frac{\partial \boldsymbol{I}_c^T}{\partial q_n} \end{bmatrix} + \begin{bmatrix} \dot{\boldsymbol{q}}^T\bar{\boldsymbol{J}}_\omega^T\frac{\partial \boldsymbol{I}_c^T}{\partial q_1} \\ \vdots \\ \dot{\boldsymbol{q}}^T\bar{\boldsymbol{J}}_\omega^T\frac{\partial \boldsymbol{I}_c^T}{\partial q_n} \end{bmatrix} + \begin{bmatrix} \dot{\boldsymbol{q}}^T\frac{\partial \bar{\boldsymbol{J}}_\omega^T}{\partial q_1}\boldsymbol{I}_c^T \\ \vdots \\ \dot{\boldsymbol{q}}^T\frac{\partial \bar{\boldsymbol{J}}_\omega^T}{\partial q_n}\boldsymbol{I}_c^T \end{bmatrix} = \bar{\boldsymbol{J}}_{\omega/q}^T\boldsymbol{I}_c^T - \boldsymbol{I}_{c/q}^{-T}\boldsymbol{I}_c^T, \tag{B.21}$$

with $\boldsymbol{I}_{c/q}^{-T}$ and $\bar{\boldsymbol{J}}_{\omega/q}^T$ defined in Eqs. (5.15) and (5.16), respectively.
From the comparison between Eq. (B.20) and the third row of Eq. (6.4), the relation (6.5b) can be derived.

C Proof of the property $\breve{\omega}^T(\dot{M}_{bq} - 2C_{bq})\breve{\omega} = 0$

It is well known that for the dynamics (2.24) the property $\boldsymbol{v}^T(\dot{\boldsymbol{M}} - 2\boldsymbol{C})\boldsymbol{v} = 0$ is valid, with $\boldsymbol{v} = [\boldsymbol{v}_b^T\ \boldsymbol{\omega}_b^T\ \dot{\boldsymbol{q}}^T]^T$, and it is transferred to the dynamics (6.4) thanks to the chosen transformation (6.1) [79], and thus

$$\begin{bmatrix} \boldsymbol{v}_{c,t}^T & \boldsymbol{\omega}_b^T & \dot{\boldsymbol{q}}^T \end{bmatrix}\left(\begin{bmatrix} \boldsymbol{0} & \boldsymbol{0} & \boldsymbol{0} \\ \boldsymbol{0} & \dot{\boldsymbol{I}}_c & \dot{\boldsymbol{I}}_c\bar{\boldsymbol{J}}_\omega + \boldsymbol{I}_c\dot{\bar{\boldsymbol{J}}}_\omega \\ \boldsymbol{0} & \dot{\bar{\boldsymbol{J}}}_\omega^T\boldsymbol{I}_c^T + \bar{\boldsymbol{J}}_\omega^T\dot{\boldsymbol{I}}_c^T & \dot{\tilde{\boldsymbol{M}}}_m \end{bmatrix} + \right. \\ \left. -2\begin{bmatrix} \boldsymbol{0} & \tilde{\boldsymbol{C}}_{cr} & \tilde{\boldsymbol{C}}_{cm} \\ -\tilde{\boldsymbol{C}}_{cr}^T & \tilde{\boldsymbol{C}}_r & \tilde{\boldsymbol{C}}_{rm} \\ -\tilde{\boldsymbol{C}}_{cm}^T & \tilde{\boldsymbol{C}}_{mr}^T & \tilde{\boldsymbol{C}}_m \end{bmatrix}\right)\begin{bmatrix} \boldsymbol{v}_{c,t} \\ \boldsymbol{\omega}_b \\ \dot{\boldsymbol{q}} \end{bmatrix} = 0. \tag{C.22}$$

Considering the relations (6.5) demonstrated in Sect. B, it is possible to write

$$\begin{aligned}
&\begin{bmatrix} \boldsymbol{v}_{c,t}^T & \boldsymbol{\omega}_b^T & \dot{\boldsymbol{q}}^T \end{bmatrix} \begin{bmatrix} \mathbf{0} & \tilde{\boldsymbol{C}}_{cr} & \tilde{\boldsymbol{C}}_{cm} \\ -\tilde{\boldsymbol{C}}_{cr}^T & \tilde{\boldsymbol{C}}_r & \tilde{\boldsymbol{C}}_{rm} \\ -\tilde{\boldsymbol{C}}_{cm}^T & \tilde{\boldsymbol{C}}_{mr}^T & \tilde{\boldsymbol{C}}_m \end{bmatrix} \begin{bmatrix} \boldsymbol{v}_{c,t} \\ \boldsymbol{\omega}_b \\ \dot{\boldsymbol{q}} \end{bmatrix} = \\
&= \begin{bmatrix} \boldsymbol{v}_{c,t}^T & \boldsymbol{\omega}_b^T & \dot{\boldsymbol{q}}^T \end{bmatrix} \begin{bmatrix} \mathbf{0} & \mathbf{0} & \mathbf{0} \\ \mathbf{0} & \boldsymbol{C}_{bq,r} & \boldsymbol{C}_{bq,rm} \\ \mathbf{0} & \boldsymbol{C}_{bq,mr} & \boldsymbol{C}_{bq,m} \end{bmatrix} \begin{bmatrix} \boldsymbol{v}_{c,t} \\ \boldsymbol{\omega}_b \\ \dot{\boldsymbol{q}} \end{bmatrix}.
\end{aligned} \tag{C.23}$$

Since the inertia matrix is the same for the dynamics (6.4) and (6.7), exploiting the relations (C.23) in (C.22), it is possible to conclude that the property $\breve{\boldsymbol{\omega}}^T(\dot{\boldsymbol{M}}_{bq} - 2\boldsymbol{C}_{bq})\breve{\boldsymbol{\omega}} = 0$ is valid for the dynamics (6.7b).

Bibliography

[1] B. Siciliano and O. Khatib, *Springer handbook of robotics*. Springer, 2016.

[2] A. Flores-Abad, O. Ma, K. Pham, and S. Ulrich, "A review of space robotics technologies for on-orbit servicing," *Progress in Aerospace Sciences*, vol. 68, pp. 1–26, 2014.

[3] D. M. Waltz, *On-orbit servicing of space systems*. Krieger Pub Co, 1993.

[4] N. Davinic, S. Chappie, A. Arkus, and J. Greenberg, "Spacecraft modular architecture design study- cost benefit analysis of on-orbit satellite servicing," in *IAF, International Astronautical Congress, 48 th, Turin, Italy*, 1997.

[5] G. Leisman, A. Wallen, S. Kramer, and W. Murdock, "Analysis and preliminary design of on-orbit servicing architectures for the GPS constellation," in *Space Technology Conference and Exposition*, p. 4425, 1999.

[6] R. Miller, M. L. Minsky, and D. B. Smith, "Space applications of automation, robotics and machine intelligence systems (ARAMIS). volume 1: Executive summary," 1982.

[7] R. Rembala and C. Ower, "Robotic assembly and maintenance of future space stations based on the ISS mission operations experience," *Acta Astronautica*, vol. 65, no. 7-8, pp. 912–920, 2009.

[8] C. Sallaberger, "Canadian space robotic activities," *Acta astronautica*, vol. 41, no. 4-10, pp. 239–246, 1997.

[9] N. Sato and S. Doi, "JEM remote manipulator system (JEMRMS) human-in-the-loop test," in *International Symposium on Space Technology and Science, 22 nd, Morioka, Japan*, pp. 1195–1199, 2000.

[10] F. Didot, M. Oort, J. Kouwen, and P. Verzijden, "The ERA system: Control architecture and performance results," in *Proc. 6th International Symposium on Artificial Intelligence, Robotics and Automation in Space (i-SAIRAS), Montral, Canada*, Citeseer, 2001.

[11] G. Hirzinger, B. Brunner, J. Dietrich, and J. Heindl, "ROTEX-the first remotely controlled robot in space," in *Proceedings of the 1994 IEEE international conference on robotics and automation*, pp. 2604–2611, IEEE, 1994.

[12] G. Hirzinger, K. Landzettel, D. Reintsema, C. Preusche, A. Albu-Schäffer, B. Rebele, and M. Turk, "Rokviss-robotics component verification on ISS," in *Proc. 8th Int. Symp. Artif. Intell. Robot. Autom. Space (iSAIRAS) (Munich 2005) p. Session2B*, 2005.

[13] M. Oda, K. Kibe, and F. Yamagata, "ETS-VII, space robot in-orbit experiment satellite," in *Proceedings of IEEE international conference on robotics and automation*, vol. 1, pp. 739–744, IEEE, 1996.

[14] R. B. Friend, "Orbital express program summary and mission overview," in *Sensors and systems for space applications II*, vol. 6958, p. 695803, International Society for Optics and Photonics, 2008.

[15] A. B. Bosse, W. J. Barnds, M. A. Brown, N. G. Creamer, A. Feerst, C. G. Henshaw, A. S. Hope, B. E. Kelm, P. A. Klein, F. Pipitone, *et al.*, "SUMO: spacecraft for the universal modification of orbits," in *Spacecraft Platforms and Infrastructure*, vol. 5419, pp. 36–46, International Society for Optics and Photonics, 2004.

[16] B. Kelm, J. Angielski, S. Butcher, N. Creamer, K. Harris, C. Henshaw, J. Lennon, W. Purdy, F. Tasker, W. Vincent, *et al.*, "FREND: pushing the envelope of space robotics," tech. rep., Naval Research Lab Washington DC, 2008.

[17] D. Barnhart, B. Sullivan, R. Hunter, J. Bruhn, E. Fowler, L. M. Hoag, S. Chappie, G. Henshaw, B. E. Kelm, T. Kennedy, *et al.*, "Phoenix program status-2013," in *AIAA SPACE 2013 conference and exposition*, p. 5341, 2013.

[18] B. Sommer, "Automation and robotics in the German space program-unmanned on-orbit servicing (OOS) & the TECSAS mission," in *55 th International Astronautical Congress*, 2004.

[19] D. Reintsema, J. Thaeter, A. Rathke, W. Naumann, P. Rank, and J. Sommer, "DEOS–the German robotics approach to secure and de-orbit malfunctioned satellites from low earth orbits," in *Proceedings of the i-SAIRAS*, pp. 244–251, Japan Aerospace Exploration Agency (JAXA) Japan, 2010.

[20] R. Biesbroek, T. Soares, J. Husing, and L. Innocenti, "The e.Deorbit CDF study: A design study for the safe removal of a large space debris," in *64th International Astronautical Congress (IAC), Beijing*, 2013.

[21] J. Kelsey, J. Byrne, M. Cosgrove, S. Seereeram, and R. Mehra, "Vision-based relative pose estimation for autonomous rendezvous and docking," in *Proceedings of IEEE Aerospace Conference*, pp. 1–20, 2006.

[22] C. Liu and H. Weiduo, "Relative pose estimation for cylinder-shaped spacecraft using single image," *IEEE Transactions on Aerospace and Electronic Systems*, vol. 50, pp. 3036–3056, 2014.

[23] O. Montenbruck and G. Eberhard, *Satellite orbits: models, methods, and applications*. Springer Verlag, 2000.

[24] S. Julier, J. Uhlmann, and H. Durrant-Whyte, "A new approach for filtering nonlinear systems," *Proceedings of the IEEE*, vol. 3, pp. 1628–1632, 1995.

[25] S. Julier and J. Uhlmann, "Unscented filtering and nonlinear estimation," *Proceedings of the IEEE*, vol. 92, no. 3, pp. 401–422, 2004.

[26] R. Park and D. Scheeres, "Nonlinear mapping of gaussian statistics: theory and applications to spacecraft trajectory design," *Journal of Guidance Control and Dynamics*, vol. 29, no. 6, pp. 1367–1375, 2006.

[27] R. Park and D. Scheeres, "Nonlinear semi-analytic methods for trajectory estimation," *Journal of Guidance Control and Dynamics*, vol. 30, no. 6, pp. 1668–1676, 2007.

[28] M. Berz, "The method of power series tracking for the mathematical description of beam dynamics," *Nuclear Instruments and Methods in Physics Research Section A: Accelerators, Spectrometers, Detectors and Associated Equipment*, vol. 258, no. 3, pp. 431–436, 1987.

[29] M. Berz, *Modern Map Methods in Particle Beam Physics*. Academic Press, 1999.

[30] M. Valli, R. Armellin, P. Di Lizia, and M. Lavagna, "Nonlinear filtering methods for spacecraft navigation based on differential algebra," *Acta Astronautica*, vol. 94, pp. 363–374, 2014.

[31] F. Cavenago, P. Di Lizia, M. Massari, and A. Wittig, "On-board DA-based state estimation algorithm for spacecraft relative navigation," in *7th European Conference for Aerospace Sciences (EUCASS 2017)*, pp. 1–14, 2017.

[32] F. Cavenago, P. Di Lizia, M. Massari, and A. Wittig, "On-board spacecraft relative pose estimation with high-order extended Kalman filter," *Acta Astronautica*, vol. 158, pp. 55–67, 2019.

[33] P. Di Lizia, M. Massari, and F. Cavenago, "Assessment of onboard DA state estimation for spacecraft relative navigation," Final Report IPL-PTE/LF/as/517.2016, European Space Agency, 2017.

[34] K. Yoshida, N. Sashida, R. Kurazume, and Y. Umetani, "Modeling of collision dynamics for space free-floating links with extended generalized inertia tensor," in *Robotics and Automation, 1992. Proceedings., 1992 IEEE International Conference on*, pp. 899–904, IEEE, 1992.

[35] X. Cyril, G. J. Jaar, and A. K. Misra, "The effect of payload impact on the dynamics of a space robot," in *Intelligent Robots and Systems' 93, IROS'93. Proceedings of the 1993 IEEE/RSJ International Conference on*, vol. 3, pp. 2070–2075, IEEE, 1993.

[36] L.-B. Wee and M. W. Walker, "On the dynamics of contact between space robots and configuration control for impact minimization," *IEEE Transactions on Robotics and Automation*, vol. 9, no. 5, pp. 581–591, 1993.

[37] D. N. Nenchev and K. Yoshida, "Impact analysis and post-impact motion control issues of a free-floating space robot subject to a force impulse," *IEEE Transactions on Robotics and Automation*, vol. 15, no. 3, pp. 548–557, 1999.

[38] S. A. A. Moosavian and E. Papadopoulos, "On the control of space free-flyers using multiple impedance control," in *Robotics and Automation, 1997. Proceedings., 1997 IEEE International Conference on*, vol. 1, pp. 853–858, IEEE, 1997.

[39] K. Yoshida, D. Dimitrov, and H. Nakanishi, "On the capture of tumbling satellite by a space robot," in *Intelligent robots and systems, 2006 IEEE/RSJ international conference on*, pp. 4127–4132, IEEE, 2006.

[40] K. Yoshida, H. Nakanishi, H. Ueno, N. Inaba, T. Nishimaki, and M. Oda, "Dynamics, control and impedance matching for robotic capture of a non-cooperative satellite," *Advanced Robotics*, vol. 18, no. 2, pp. 175–198, 2004.

[41] S. Abiko, R. Lampariello, and G. Hirzinger, "Impedance control for a free-floating robot in the grasping of a tumbling target with parameter uncertainty," in *Intelligent Robots and Systems, 2006 IEEE/RSJ International Conference on*, pp. 1020–1025, IEEE, 2006.

[42] A. M. Giordano, G. Garofalo, and A. Albu-Schaffer, "Momentum dumping for space robots," in *Decision and Control (CDC), 2017 IEEE 56th Annual Conference on*, pp. 5243–5248, IEEE, 2017.

[43] A. M. Giordano, D. Calzolari, and A. Albu-Schäffer, "Workspace fixation for free-floating space robot operations," in *Robotics and Automation (ICRA), 2018 IEEE International Conference on*, IEEE, 2018.

[44] A. Flores-Abad, M. Nandayapa, and M. A. Garcia-Teran, "Force sensorless impedance control for a space robot to capture a satellite for on-orbit servicing," in *2018 IEEE Aerospace Conference*, IEEE, 2018.

[45] S. Haddadin, A. De Luca, and A. Albu-Schäffer, "Robot collisions: A survey on detection, isolation, and identification," *IEEE Transactions on Robotics*, vol. 33, no. 6, pp. 1292–1312, 2017.

[46] T. Ren, Y. Dong, D. Wu, and K. Chen, "Collision detection and identification for robot manipulators based on extended state observer," *Control Engineering Practice*, vol. 79, pp. 144–153, 2018.

[47] F. Flacco, A. Paolillo, and A. Kheddar, "Residual-based contacts estimation for humanoid robots," in *Humanoid Robots (Humanoids), 2016 IEEE-RAS 16th International Conference on*, pp. 409–415, IEEE, 2016.

[48] J. Vorndamme, M. Schappler, and S. Haddadin, "Collision detection, isolation and identification for humanoids," in *2017 IEEE International Conference on Robotics and Automation (ICRA)*, pp. 4754–4761, IEEE, 2017.

[49] T. Tomić and S. Haddadin, "Simultaneous estimation of aerodynamic and contact forces in flying robots: Applications to metric wind estimation and collision detection," in *Robotics and Automation (ICRA), 2015 IEEE International Conference on*, pp. 5290–5296, IEEE, 2015.

[50] T. Tomić, C. Ott, and S. Haddadin, "External wrench estimation, collision detection, and reflex reaction for flying robots," *IEEE Transactions on Robotics*, vol. 33, no. 6, pp. 1467–1482, 2017.

[51] J. Artigas, M. De Stefano, W. Rackl, R. Lampariello, B. Brunner, W. Bertleff, R. Burger, O. Porges, A. Giordano, C. Borst, *et al.*, "The OOS-SIM: An on-ground simulation facility for on-orbit servicing robotic operations," in *2015 IEEE International Conference on Robotics and Automation (ICRA)*, pp. 2854–2860, IEEE, 2015.

[52] M. Massari, P. Di Lizia, F. Cavenago, and A. Wittig, "Differential algebra software library with automatic code generation for space embedded applications," AIAA SciTech Forum, American Institute of Aeronautics and Astronautics, Jan. 2018.

[53] R. Biesbroek, "The e.Deorbit ESA CDF study," *Proceedings of the SPIE*, vol. 5088, pp. 20–30, 2003.

[54] H. Schaub and J. L. Junkins, *Analytical mechanics of space systems*. Aiaa, 2003.

[55] M. Massari and M. Zamaro, "Application of SDRE technique to orbital and attitude control of spacecraft formation flying," *Acta Astronautica*, vol. 94, no. 1, pp. 409–420, 2014.

[56] S. Marandi and V. Modi, "A preferred coordinate system and the associated orientation representation in attitude dynamics," *Acta Astronautica*, vol. 15, no. 11, pp. 833–843, 1987.

[57] R. M. Murray, *A mathematical introduction to robotic manipulation*. CRC press, 2017.

[58] H. K. Khalil, "Nonlinear systems," *Upper Saddle River*, 2002.

[59] D. Angeli, "Input-to-state stability of PD-controlled robotic systems," *Automatica*, vol. 35, no. 7, pp. 1285–1290, 1999.

[60] L. Isserlis, "On a formula for the product-moment coefficient of any order of a normal frequency distribution in any number of variables," *Biometrika*, vol. 12, 1918.

[61] G. Casella and R. L. Berger, *Statistical inference*, vol. 2. Duxbury Pacific Grove, CA, 2002.

[62] M. Valli, R. Armellin, P. Di Lizia, and M. Lavagna, "Nonlinear mapping of uncertainties in celestial mechanics," *Journal of Guidance Control and Dynamics*, vol. 36, pp. 48–63, 2013.

[63] J. Gil-Fernández, T. Prieto-Llanos, and R. Panzeca, "Autonomous GNC algorithms for NEO impactor missions," in *Proceedings of the 20th International Symposium on Space Flight Dynamics*, pp. 1–14, 2007.

[64] S. J. Julier and J. K. Uhlmann, "A new extension of the Kalman filter to nonlinear systems," in *Int. symp. aerospace/defense sensing, simul. and controls*, vol. 3, pp. 182–193, Orlando, FL, 1997.

[65] S. J. Julier and J. K. Uhlmann, "A general method for approximating nonlinear transformations of probability distributions," tech. rep., Technical report, Robotics Research Group, Department of Engineering Science, University of Oxford, 1996.

[66] S. J. Julier and J. K. Uhlmann, "Unscented filtering and nonlinear estimation," *Proceedings of the IEEE*, vol. 92, no. 3, pp. 401–422, 2004.

[67] C. Stachniss, "Robot mapping - unscented Kalman filter," Uni Freiburg - ASI: Autonomous Intelligence Systems.

[68] H. Wang and M. Brady, "Real-time corner detection algorithm for motion estimation," *Image and vision computing*, vol. 13, no. 9, pp. 695–703, 1995.

[69] "European Space Agency, Annex C: Envisat specification," pp. 22–23, 17/05/2016.

[70] J. L. Crassidis and F. L. Markley, "Unscented filtering for spacecraft attitude estimation," *Journal of guidance, control, and dynamics*, vol. 26, no. 4, pp. 536–542, 2003.

[71] A. P. Gallardo, H. Mishra, A. M. Giordano, and R. Lampariello, "Robust estimation of motion states for free-floating tumbling target capture," in *2019 IEEE Aerospace Conference*, pp. 1–11, IEEE, 2019.

[72] J. L. Crassidis, "Sigma-point Kalman filtering for integrated gps and inertial navigation," *IEEE Transactions on Aerospace and Electronic Systems*, vol. 42, no. 2, pp. 750–756, 2006.

[73] F. Aghili and K. Parsa, "Adaptive motion estimation of a tumbling satellite using laser-vision data with unknown noise characteristics," in *2007 IEEE/RSJ International Conference on Intelligent Robots and Systems*, pp. 839–846, IEEE, 2007.

[74] F. Cavenago, A. M. Giordano, and M. Massari, "Force observer for space robots," in *2019 IEEE 58th Annual Conference on Decision and Control (CDC)*, IEEE, 2019.

[75] A. M. Giordano, C. Ott, and A. Albu-Schäffer, "Coordinated control of spacecraft's attitude and end-effector for space robots," *IEEE Robotics and Automation Letters*, vol. 4, no. 2, pp. 2108–2115, 2019.

[76] C. Alippi, G. Boracchi, and M. Roveri, "Change detection tests using the ICI rule," in *Neural Networks (IJCNN), The 2010 International Joint Conference on*, pp. 1–7, IEEE, 2010.

[77] A. Goldenshluger and A. Nemirovski, "On spatially adaptive estimation of nonparametric regression," *Mathematical methods of Statistics*, vol. 6, no. 2, pp. 135–170, 1997.

[78] F. Oestersötebier, P. Wang, and A. Trächtler, "A Modelica contact library for idealized simulation of independently defined contact surfaces," in *Proceedings of the 10 th International Modelica Conference; March 10-12; 2014; Lund; Sweden*, no. 096, pp. 929–937, Linköping University Electronic Press, 2014.

[79] G. Garofalo, C. Ott, and A. Albu-Schäffer, "On the closed form computation of the dynamic matrices and their differentiations," in *2013 IEEE/RSJ International Conference on Intelligent Robots and Systems*, pp. 2364–2359, IEEE, 2013.

[80] H. Yoon and P. Tsiotras, "Spacecraft adaptive attitude and power tracking with variable speed control moment gyroscopes," *Journal of Guidance, Control, and Dynamics*, vol. 25, no. 6, pp. 1081–1090, 2002.

[81] J. M. Cameron and W. J. Book, "Modeling mechanisms with nonholonomic joints using the Boltzmann-Hamel equations," *The International Journal of Robotics Research*, vol. 16, no. 1, pp. 47–59, 1997.